

**Multiphase flow in porous media
with phase transitions:
from CO₂ sequestration to gas hydrate systems**

by

Xiaojing Fu

Submitted to the Department of Civil and Environmental Engineering
in partial fulfillment of the requirements for the degree of

Doctor of Philosophy in Civil and Environmental Engineering

at the

MASSACHUSETTS INSTITUTE OF TECHNOLOGY

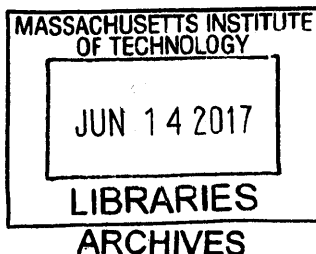
June 2017

© Massachusetts Institute of Technology 2017. All rights reserved.

Author **Signature redacted**
Department of Civil and Environmental Engineering
May 19, 2017

Certified by **Signature redacted**
/ Ruben Juanes
Associate Professor, Civil and Environmental Engineering
Thesis Supervisor

Accepted by **Signature redacted**
/ Jesse Kroll
Associate Professor, Civil and Environmental Engineering
Chairman, Graduate Program Committee



Multiphase flow in porous media
with phase transitions:
from CO₂ sequestration to gas hydrate systems

by

Xiaojing Fu

Submitted to the Department of Civil and Environmental Engineering
on May 19, 2017, in partial fulfillment of the
requirements for the degree of
Doctor of Philosophy in Civil and Environmental Engineering

Abstract

Ongoing efforts to mitigate climate change include the understanding of natural and engineered processes that can impact the global carbon budget and the fate of greenhouse gases (GHG). Among engineered systems, one promising tool to reduce atmospheric emissions of anthropogenic carbon dioxide (CO₂) is geologic sequestration of CO₂, which entails the injection of CO₂ into deep geologic formations, like saline aquifers, for long-term storage. Among natural contributors, methane hydrates, an ice-like substance commonly found in seafloor sediments and permafrost, hold large amounts of the world's mobile carbon and are subject to an increased risk of dissociation due to rising temperatures. The dissociation of methane hydrates releases methane gas—a more potent GHG than CO₂—and potentially contributes to a positive feedback in terms of climatic change.

In this Thesis, we explore fundamental mechanisms controlling the physics of geologic CO₂ sequestration and natural gas hydrate systems, with an emphasis on the interplay between multiphase flow—the simultaneous motion of several fluid phases—and phase transitions—the creation or destruction of fluid or solid phases due to thermodynamically driven reactions.

We first study the fate of CO₂ in saline aquifers in the presence of CO₂–brine–carbonate geochemical reactions. We use high-resolution simulations to examine the interplay between the density-driven convective mixing and the rock dissolution reactions. We find that dissolution of carbonate rock initiates in regions of locally high mixing, but that the geochemical reaction shuts down significantly earlier than shutdown of convective mixing. This early shutdown reflects the important role that chemical speciation plays in this hydrodynamics–reaction coupled process.

We then study hydrodynamic and thermodynamic processes pertaining to a gas hydrate system under changing temperature and pressure conditions. The framework for our analysis is that of phase-field modeling of binary mixtures far from equilibrium, and show that: (1) the interplay between phase separation and hydrodynamic insta-

bility can arrest the Ostwald ripening process characteristic of nonflowing mixtures; (2) partial miscibility exerts a powerful control on the degree of viscous fingering in a gas-liquid system, whereby fluid dissolution hinders fingering while fluid exsolution enhances fingering. We employ this theoretical phase-field modeling approach to explain observations of bubble expansion coupled with gas dissolution and hydrate formation in controlled laboratory experiments. Unraveling this coupling informs our understanding of the fate of hydrate-crusting methane bubbles in the ocean water column and the migration of gas pockets in hydrate-bearing sediments.

Thesis Supervisor: Ruben Juanes

Title: Associate Professor, Civil and Environmental Engineering

Acknowledgments

I would like to express my deepest gratitude to my research advisor, Ruben Juanes, for your insightful teaching, patience, kindness, friendship and for always giving me the courage and resources to explore new ideas;

To my dearest collaborator, mentor and friend, Luis Cueto-Felgueroso, I am deeply grateful for your generosity, kindness, insights, patience and friendship;

To my committee member Carolyn Ruppel, I am truly grateful for your time, advice and encouragement, and for showing me the fascinating world of gas hydrates;

To my committee chair Charlie Harvey, for always being a great source of intellectual discussion and inspiration;

To former and current members of the Juanes research group, thank you for creating so many great memories and for your friendship. I will miss the Thai/Indian take out and pizza lunches at the group meetings, the ping pong tournaments and dinner preparation at group retreats, and the Friday beers;

I am very lucky to have really wonderful friends from the Parsons laboratory, the Pierce laboratory and the rock climbing community; thank you for keeping my head above the water all these years;

To my parents Ming Fu and Li Wan, I want to thank you for all that you have provided for me. To my dad, who teaches me to be brave and curious, and to my mom, who teaches me to love and appreciate mathematics and life, thank you for giving me the freedom to explore the world far away from you and home;

Last but not least, to my partner Ryan Lewis, thank you for your love, encouragement, patience and companion, and for damping all the turbulence and creating rays of sunshine in my life. I am so blessed to have you by my side.

献给铭和在水一方。

“蒹葭苍苍，白露为霜。所谓伊人，在水一方。
溯洄从之，道阻且长。溯游从之，宛在水中央。
蒹葭萋萋，白露未晞。所谓伊人，在水之湄。
溯洄从之，道阻且跻。溯游从之，宛在水中坻。
蒹葭采采，白露未已。所谓伊人，在水之涘。
溯洄从之，道阻且右。溯游从之，宛在水中沚。”

---- 《诗经·蒹葭》

Contents

1	Introduction	21
1.1	Rock dissolution patterns and geochemical shutdown of CO ₂ -brine-carbonate reactions during convective mixing in porous media	23
1.2	Phase-field modeling of partially miscible fluids	25
1.2.1	Thermodynamic coarsening arrested by viscous fingering in partially-miscible binary mixtures	25
1.2.2	Viscous fingering with partially miscible fluids	26
1.3	Phase-field modeling of gas-liquid-hydrate systems	26
2	Rock dissolution patterns and geochemical shutdown of CO₂-brine-carbonate reactions during convective mixing in porous media	29
2.1	Introduction	30
2.1.1	Decoupled formulation for multispecies reactive transport	32
2.2	Mathematical formulation	34
2.3	Dissolution regimes	39
2.3.1	Mixing-controlled dissolution patterns	39
2.3.2	Speciation-controlled reaction shutdown	41
2.4	Impact on the macroscopic mass exchange rate	43
2.5	Dissolution patterns in three dimensions	45
2.5.1	Coarsening of dissolution patterns	48
2.6	Summary	50
2.A	Comparison between time to reach chemical equilibrium and characteristic time of transport	51

2.B	Geochemical speciation curve	53
3	Thermodynamic coarsening arrested by viscous fingering in partially-miscible binary mixtures	55
3.1	Introduction	55
3.2	Mathematical model	58
3.2.1	Phase-field modeling of two-phase Darcy flow with compositional effects	58
3.2.2	Design of free energy	60
3.2.3	Scaling analysis	62
3.3	Problem statement	63
3.4	Coarsening in gas-liquid mixtures by Ostwald ripening	64
3.5	Coarsening arrest by viscous fingering	66
3.6	Permanent supersaturation in liquid phase by hydrodynamic stirring .	67
4	Viscous fingering with partially miscible fluids	71
4.1	Introduction	71
4.2	Problem setup and numerical methods	75
4.3	Results	77
4.3.1	Fingering pattern under the influence of gas dissolution and exolution	77
4.3.2	The coupling between ϕ and c	80
4.3.3	Thermodynamic control on the degree of fingering	81
4.3.4	Impact of viscous fingering on the rate of gas dissolution/exolution	82
4.3.5	Heterogeneity in phase compositions	83
4.4	Conclusions	84
5	Phase-field modeling of gas-liquid-hydrate systems	87
5.1	Introduction	87
5.1.1	Predicting gas hydrate stability using thermodynamic phase diagrams	91

5.1.2	Laboratory experiments	94
5.2	Hydrate phase diagram through a simplified free energy description	100
5.2.1	Motivation for a simplified free energy description	100
5.2.2	Primary variables	102
5.2.3	Basic elements in a free energy functional	104
5.2.4	Single phase Gibbs free energy $f_\alpha(\chi)$	104
5.2.5	The common tangent construction technique for three-phase system	106
5.2.6	Single phase Gibbs free energy $f_\alpha(\chi, T)$	107
5.2.7	An isobaric phase diagram based on simplified Gibbs free energy	110
5.2.8	Isobaric phase diagram at different pressures	110
5.3	Phase-field modeling of phase separation dynamics	118
5.3.1	The bulk free energy density of a three-phase system	118
5.3.2	Total free energy of a three-phase system	119
5.3.3	Conservation of methane mass	120
5.3.4	Evolution equation for ϕ_α	121
5.3.5	Summary of model equations and parameters	122
5.4	Phase separation simulations above and below the triple point	126
5.4.1	Phase separation in vapor-liquid region	126
5.4.2	Phase separation in hydrate-forming region	127
5.4.3	Phase separation dynamics in a ternary diagram	129
5.5	Growth kinetics of hydrate on a gas-liquid interface	131
5.5.1	Slow diffusion within hydrate layer leads to prolonged three- phase coexistence	131
5.5.2	Implications for the fate of hydrate-crusted bubbles	133
5.5.3	The rate of hydrate film growth: diffusion-limited and kinetically- controlled regimes	135
5.5.4	Implications for predicting occurrence of hydrate-crusted bub- bles in natural water columns	137
5.6	Compressibility of mixtures	140

5.6.1	Three-phase mixture velocity under Darcy's law	141
5.6.2	Evolution equations with advection	142
5.6.3	Discretization of pressure equation	143
5.6.4	Example in 1D: hydrate growth on an expanding gas bubble .	143
5.6.5	Results and discussion	146
5.7	Modeling rupturing behavior of a hydrate shell	150
5.7.1	General viscosity law for non-Newtonian fluid in bulk flow . .	150
5.7.2	A generalized Darcy's law for viscoelastic fluid in a Hele-Shaw cell	151
5.7.3	2D simulation of hydrate shell rupturing	153
6	Implication, discussion and conclusions	155

List of Figures

2-1	The problem is set up in a two-dimensional square homogeneous porous medium composed mainly of carbonate rocks. The domain is impermeable at the top and bottom. <i>Solution 1</i> , the equilibrated CO ₂ -rich brine, enters via diffusion at the top of the formation, which is initially saturated with <i>Solution 2</i> , the equilibrated aquifer-brine.	36
2-2	Snapshots of mixing ratio (left column) and porosity percentage increase (right column) for a simulation with H=6000, Da=20 and $R_\phi = 2$ at time $t = 0.6H$ (top), 4H (middle) and 15H (bottom).	40
2-3	Volume-averaged measures of (a) percentage increase in ϕ (b) chemical speciation and (c) scalar dissipation rate over time for a simulation with H=6000. The transition in curve color from light orange to dark indicates increase in Da. The dark circles in (a) and (b) indicate the shutdown time $t_{sd}^{\Delta\phi}$ and $t_{sd}^{F(\alpha)}$, respectively, as defined in Sec. 2.3.2. (d) Cumulative (volume-averaged) porosity increase plotted against Da for different values of H (red, blue and black). (e) and (f) $t_{sd}^{\Delta\phi}$ and $t_{sd}^{F(\alpha)}$ plotted against Da for different values of H.	44
2-4	Volume-averaged measure of mass exchange rate of solution 1 for increasing Damköhler numbers with H=6000 (top) and for three values of H with Da=20 (bottom). The blue curves in both figures correspond to the case with H=6000 and without reaction (Da=0).	46
2-5	Dissolution patterns in 3D: for a simulation of H=2500, Da=5 and $R_\phi=2$, at $t/H = 14.0$, this figure shows surface contours for (a) $\Delta\phi = 4\%$ and (b) $\Delta\phi = 8\%$	47

2-6	Dissolution rate (laterally averaged) at various depths over time. Cyan-colored dots correspond to the “freezing” events, which is around the time that the tessellation pattern at that depth adopts its final configuration.	48
2-7	Horizontal slices of the reaction rate $r = \phi F(\alpha) \nabla \alpha \cdot \nabla \alpha$ (color frames) and the relative porosity increase $\Delta\phi/\phi_0$ (black and white frames) at different depths: (a) $z/H = 0.01$, (b) $z/H = 0.14$, (c) $z/H = 0.27$, (d) $z/H = 0.54$, (e) $z/H = 0.82$ and (f) $z/H = 1.0$. The color frames for r are at different times: (a) $t/H = 6.0$, (b) $t/H = 1.2$, (c) $t/H = 2.7$, (d) $t/H = 5.0$, (e) $t/H = 7.8$ and (f) $t/H = 10.1$ (subtracted from a background image corresponding to $t/H = 8.9$ for clarity). Red color indicates high value (colormap not shown). The black and white frames for $\Delta\phi/\phi_0$ are all at time $t/H = 14.0$. The colormap range varies with depth to best reflect the dissolution structure.	49
2-8	Number of dissolved polygonal rings as a function of depth at $t = 14$.	50
2-9	When solution 1 and 2 mix at $\alpha = 0.01$, concentration of Ca^{2+} in the mixed solution increases over time as the mixture equilibrates over course of tens of hours.	52
2-10	(a) Vertical concentration profiles at $t = 5$ for different Rayleigh numbers. We only show one sample of each Rayleigh number here while the analysis is done using ensemble of 5 samples for each Rayleigh number. Here $z^* = z/L$, where L is the natural length scale. (b) Average thickness of boundary layer, $L_{\text{diff}}^* = L_{\text{diff}}/L$, as a function of Rayleigh numbers.	53
2-11	Speciation curve $F(\alpha)$ obtained from PHREEQC. The dashed line (inset) is the calcium molality ($[\text{Ca}^{2+}]$) versus α . The solid line (main plot) is the second derivative, computed numerically, of the dashed line.	54

3-1	<p>(Top) The common tangent construction (blue line) on the bulk free energy of pure phases yields the equilibrium concentrations (green circles) within gas and liquid. For parameters $\alpha_l=1$, $\beta_l=500$, $\alpha_g=200$, $\beta_g=2\times 10^{-4}$, the equilibrium compositions are $c_l^{\text{eq}}\approx 0.304$ and $c_g^{\text{eq}}\approx 0.828$. (Bottom) Zoomed-in snapshots of c illustrate the process of spinodal decomposition of a domain that is initially filled with supersaturated liquid ($t=0$). The progression shows vapor bubbles (high c, red-colored) that nucleate and coarsen out of the liquid phase (low c, pink-colored).</p>	61
3-2	<p>Snapshots of c (top) and ϕ (bottom) illustrating the Ostwald ripening process in a system with a small and a large vapor bubble, in an liquid bath that is initially at local equilibrium.</p>	64
3-3	<p>Snapshots of c at $t=40, 200, 300$ and 400, under no flow (top) and with periodic left-to-right flow imposed at $t>40$ (bottom).</p>	65
3-4	<p>(a) $\langle r \rangle^3$ vs. t for simulations without flow (dashed red line) and with background flow after $t = 40$ (solid black line), emphasizing arrest of thermodynamic coarsening in the presence of flow. Inset: $\langle r \rangle$ vs. t in log-log scale, emphasizing algebraic growth of spinodal decomposition ($\langle r \rangle \sim t^{1/3}$) in the absence of flow. (b–c) Normalized distribution of $r/\langle r \rangle$ at sampling times for simulations without flow (b) and with flow introduced at $t = 40$ (c). (d) $\overline{\langle r \rangle}$ vs. Ca for different Pe. (e) $\overline{\langle r \rangle}$ rescaled with $\text{Pe}^{-0.078}$ vs. Ca. Inset: $\overline{\langle r \rangle}$ vs. Pe for different Ca.</p>	68
3-5	<p>Evolution of the averaged liquid-phase concentration $\langle c_l \rangle$ for systems without background flow (red solid line) and with background flow after $t=40$ (black solid line). The gray dashed line indicates equilibrium liquid-phase concentration from the common tangent construction [Fig. 3-1(top)]. Insets: zoomed-in snapshots of c. The circle highlights pinch-off of a small bubble that quickly dissolves into the liquid—the colormap range is $(0.3, 0.35)$ to emphasize concentration variations around the c_l^{eq}.</p>	69

4-1	Displacement of a gas band through liquid phase in a Hele-Shaw cell: (a) initial set up (b) the displacement leads to viscous fingering due to viscosity contrast. Meanwhile, compositional exchange occurs along the fingering interface if the two fluids are out of thermodynamic equilibrium. For example, in this sample image, the liquid phase is initially supersaturated with respect to gas and will swell the gas fingers as they evolve (see Sec. 5.1.1). The blue dashed box indicates the area of study in our discussions.	75
4-2	The coupling between different viscosity contrast and compositional effects lead to a rich set of viscous fingering patterns. Here we show snapshots of c at $t = 50$ for six different R values (across each row). Each of the three rows correspond to different c_l^0 values: defending liquid is (a) undersaturated; (b) near-saturated and (c) oversaturated. Note that the colormap differs between each row to reveal the detailed structures in the concentration field.	78
4-3	Defending fluid is (a) undersaturated or (b) supersaturated. Top: snapshots of ϕ at $t = 46$. Middle: snapshots of c at $t = 46$. Bottom: horizontal transects of ϕ (dashed) and c (solid) at $t = 46$ along the dashed lines indicated in the 2D plots in the top and middle rows. Note that regions where $c \approx 0.33$ indicate area in which local thermodynamic equilibrium is in place.	80
4-4	Normalized interfacial length, \mathcal{L}/L_y , as a function of time for three compositional scenarios with (a) $R = 5$ and (b) $R = 1$. In both plots, colored insets show the traced outline of the fingering front at $t = 50$ for oversaturated, near-saturated and unsaturated defending liquid (left to right).	81
4-5	$\Delta\overline{\phi}_g(t)$ for $R = 0, 1, 2, 3, 4, 5$ (arrows indicating increasing order) when the defending phase is undersaturated (left) and supersaturated (right). The insets in both plots show snapshots of ϕ at $t = 50$ for the different values of R	82

4-6	(Left) $\bar{c}_y(x)$ at $t = 0, 10, 20, 30, 40$ and 50 . Blue arrow indicates direction of time. Red dashed line indicates thermodynamic equilibrium: $c_i^{\text{eq}} \approx 0.33$. Red shaded area indicates metastability. (Right) snapshots of c for the corresponding times. The defending liquid is initially undersaturated in (a) and supersaturated in (b), and all simulations correspond to $R = 5$	85
5-1	Predicted and measured hydrate compositions at 30MPa illustrated in a T- χ phase diagram. Figure is from (Huo et al., 2003). Waiting for permission from John Wiley and Sons.	94
5-2	The temperature-composition phase diagram for methane-water system from (Huo et al., 2003; Sloan and Koh, 2008; Sloan et al., 2010). Here concentration is given in methane mole fraction. The diagram is not plot to scale in order to emphasize certain features. Figure is taken from (Huo et al., 2003). Waiting for permission from John Wiley and Sons.	95
5-3	Illustration of the Hele-Shaw cell showing the inlet/outlet for water and inlet for Xe.	96
5-4	Phase diagram for xenon-water system at various pressure and temperature. The orange line marks the gas-liquid phase boundary for xenon. The dashed black box marks the supercritical region of xenon. The blue curve marks the phase boundary for xenon-hydrate stability region (shaded grey). The phase boundaries for xenon-water system (blue and orange) are plotted based on measurements from (Ohgaki et al., 2000) and CSMGem calculations (Sloan and Koh, 2008). . . .	97
5-5	Time-lapse of Xe bubble (black) depressurization from the surrounding water (grey) in a Hele-Shaw cell. Gas expands during depressurization, causing a hydrate-encrusted finger to form and migrate.	97

5-6	The controlled expansion of the hydrate-crust bubble can be decomposed into three mechanisms: gas expansion, crust rupturing and crust healing/growth	98
5-7	Comparison between χ and C as a function of C for methane-water (left) and xenon-water system (right)	103
5-8	The bulk free energy of each phases, $f_\alpha(\chi)$, as introduced in Eq. (5.2)-(5.4): gas (red), liquid (blue) and solid(black). The grey dashed lines are the common tangents for liquid-solid and gas-solid curves. The green dots mark the tangent points obtained from the constructions. The common tangent for liquid-gas pair is not shown here.	105
5-9	Gibbs free energy of all phases (f_α) at various temperatures. The feasible common tangent constructions are plotted in dashed grey line.	109
5-10	The $T - \chi$ phase diagram obtained analytical from our <i>model</i> three-phase system based on Eqs. (5.7)-(5.9) and Eq. (5.10). The parameter values come from Table 5.2.	111
5-11	The $T - \chi$ phase diagram obtained analytical from our <i>model</i> three-phase system.	112
5-12	The $T - \chi$ phase diagram obtained analytical from our <i>model</i> three-phase system at $P= 5\text{MPa}$. The blue line represents compositions calculated for L_w -V equilibrium. Similarly, the red dashed lines are for H-V equilibrium and the black line is for L_w -H equilibrium. Sub figure (b) is the enlarged version of the shaded grey area in (a). Sub figure (c) is the blowup of the green box in (b). The dashed line marks the triple point temperature in all sub figures.	116
5-13	The $T - \chi$ phase diagram obtained analytical from our <i>model</i> three-phase system at $P= 30\text{MPa}$. The blue dashed line represents compositions calculated for L_w -V equilibrium. Similarly, the red dashed lines are for H-V equilibrium and the black line is for L_w -H equilibrium. Sub figure (b) is the blowup of the green box in (a). The dashed line marks the triple point temperature.	117

5-14 At $T = 20$, an initially perturbed mixture with an average molar fraction of $\bar{\chi} = 0.4$ phase separates into gas and liquid. At equilibrium, $\bar{\chi}_g \approx 0.875$ and $\bar{\chi}_l \approx 0.08$. The snapshots are shown at $t = 0, 0.6, 2$ and 40. These equilibrium values match that predicted by the phase diagram calculated in Fig. 5-10. 127

5-15 At $T = 5$, a temperature when hydrate can form, the domain is initially occupied by three gas bubbles with $\chi_g = 0.9$ surrounded by liquid with $\chi_l = 0.01$; no hydrate is present initially. The average molar fraction in the entire domain is $\bar{\chi} = 0.238$. As the mixture evolves, hydrate first forms at the gas-liquid interface, then hydrate preferentially grow into the liquid phase, which has an elevated χ due to some initial gas dissolution. At equilibrium, there are only gas and hydrate present and $\bar{\chi}_g \approx 0.968$ and $\bar{\chi}_s \approx 0.149$. These equilibrium values match that predicted by the phase diagram calculated in Fig. 5-2. 128

5-16 At $T = 5$, a temperature when hydrate can form, the domain is initially occupied by a single gas bubbles with $\chi_g = 0.9$ surrounded by liquid with $\chi_l = 0.01$; no hydrate is present initially. The average molar fraction in the entire domain is $\bar{\chi} = 0.066$. As the mixture evolves, hydrate first forms at the gas-liquid interface, then hydrate preferentially grow into the gas phase and eventually replaces the gas bubble completely. At equilibrium, there are only liquid and hydrate present with $\bar{\chi}_l \approx 0.0088$ and $\bar{\chi}_s \approx 0.079$. These equilibrium values match that predicted by the phase diagram calculated in Fig. 5-2. 129

5-17	Phase separation dynamics drawn in a ternary diagram. The colormap references time. Trajectory 1 corresponds to simulation shown in Fig. 5-15 or the green star in Fig. 5-10. Trajectory 2 corresponds to simulation shown in Fig. 5-16 or the green square in Fig. 5-10. Trajectory 3 corresponds to simulation shown in Fig. 5-18, where diffusion inside hydrate is much slower compared to that in Fig. 5-16. Note trajectory 2 and 3 start at the same location but terminate at different points.	130
5-18	This simulation uses the same parameters as in Fig. 5-16, but diffusion coefficients are assigned differently. In Fig. 5-16, $D_l = D_s = D_g = 1$. In this simulation, $D_l = 0.1$, $D_s = 10^{-5}$, $D_g = 1$	132
5-19	Sample profiles of ϕ_g (red), ϕ_l (blue), ϕ_s (black) and χ (green) of a series of simulations performed in Sec. 5.5.3. (Top): initial condition; (bottom): end of simulation at $t = 1.5$	136
5-20	(a) Zoomed-in view of the free energy curves shown in Fig. 5-8. Here we focus on the L_w -H region. The colored dots mark the liquid phase compositions for each simulation. Note that $\chi_l^{\text{eq}} \approx 0.03$ is the 3rd dot from left. (b) The corresponding hydrate film thickness (here calculated as the domain averaged hydrate volume fraction $\overline{\phi_s}$) as a function of time for all simulations.	138
5-21	(a): $\overline{\phi_s}$ vs. t in log-log scale. (b) enlarged view of the dashed box in (a).	139
5-22	Density of methane gas, liquid water and hydrate as a function of pressure.	141
5-23	Snapshots of χ , ϕ_s and ρ describing the details of an expanding hydrate-crusted bubble.	147
5-24	Snapshots of p during the expansion of a hydrate-crusted bubble. . .	148
5-25	Snapshots of u_x during the expansion of a hydrate-crusted bubble. . .	149
5-26	Shear thinning viscosities as a function of $ \nabla p ^2$ for weakly shear thinning (blue, Eq. (5.74)) and strongly shear-thinning (red, Eq. (5.75)) fluids.	153

5-27 Evolution of the hydrate-crusted gas-liquid interface under a constant gas injection from left. The colors here correspond to volume fraction of hydrate (ϕ_s), where white indicates 1 and black indicates 0. 154

Chapter 1

Introduction

The ongoing efforts to mitigate climate change focus on two fronts. First, we are in search of effective strategies to reduce emissions of anthropogenic carbon dioxide (CO_2) into the atmosphere. Second, we need to better understand how naturally occurring greenhouse gases (GHG) contribute to the global budget and impact the environment. One key challenge in moving forward on both fronts is the detailed understanding of processes that control the transport of GHG within its ambient environment.

For example, one promising climate-change mitigation tool is the large-scale injection of CO_2 into deep saline aquifers. Upon injection, buoyant CO_2 enters the geologic formation and mixes with the underlying brine, which leads to a local density increase that triggers density-driven flow. This phenomena is termed *convective mixing* and is an essential trapping mechanism during CO_2 sequestration in deep saline aquifers. Meanwhile, the presence of CO_2 disturbs the geochemical equilibrium of brine with respect to the formation, which can lead to dissolution or precipitation of carbonate minerals. Dissolution/precipitation reactions result in changes in porosity, which in turn induce changes in permeability that impact the flow dynamics. Understanding the impact of rock dissolution and CO_2 -brine-carbonate geochemical reactions on the fate of CO_2 plumes is crucial to addressing the feasibility of geologic sequestration of CO_2 .

Our current estimation of global GHG budget is highly uncertain because of the

difficulty in predicting naturally occurring contributions. This includes contribution of atmospheric methane (CH_4)—a greenhouse gas 100 times more potent than CO_2 —from wetlands, ruminants, termites and gas hydrates. Among these natural contributors, gas hydrates, an ice-like solid commonly found in seafloor sediments and permafrost, contain somewhere between 15% up to more than 50% of the world’s mobile carbon and are subject to an increased risk of dissociation due to rising temperatures. The breakdown of gas hydrate in the marine environment releases methane from the seafloor in the form of methane bubble plumes. Understanding the fate of a single methane bubble or a methane-bubble plume after the release is important in assessing the impact of methane seepage from seafloor on the ocean biogeochemistry and possibly on the atmospheric methane budget. It has been observed in field studies and controlled laboratory experiments that rising methane bubbles may form a hydrate shell as they traverse the hydrate stability zone. Quantifying the effect of a hydrate shell on the transport of methane in the water column remains a challenging question.

In both examples described above, the key processes, being the dissolution of carbonate rock by migrating CO_2 -rich brine and the solidification of hydrate on moving gas-water interfaces, entail multiphase hydrodynamics coupled with thermodynamically driven phase transitions. Multiphase hydrodynamics is defined here as the simultaneous motion of several fluids with distinctive physical or chemical properties. Phase transition in this work refers to the creation or destruction of fluid or solid phases due to thermodynamically driven reactions.

In this Thesis, we use tools of modeling and simulation to explore multiphase problems involving phase transitions in the context of CO_2 sequestration and natural gas hydrate systems. The challenge in continuum modeling and simulation of this type of problem is the robust coupling of the complex thermodynamics into multiphase hydrodynamics within a reasonable computational budget. This Thesis addresses this challenge by adopting and constructing novel modeling frameworks that are computationally tractable. Through high-resolution numerical simulations of these models, we gain insights into the overarching scientific questions and also uncover new physics

in the field of pattern formation and phase separation.

1.1 Rock dissolution patterns and geochemical shutdown of CO₂–brine–carbonate reactions during convective mixing in porous media

Sequestering anthropogenic CO₂ by injecting and storing it in geologic formations has been proposed as a promising tool to mitigate climate change. The sequestration process involves the capture of CO₂ from anthropogenic sources such as coal-fired and gas-fired power plants, the transportation after compression through a pipeline system and, finally, the injection of supercritical CO₂ into underground geologic formations such as deep saline aquifers. Upon injection, CO₂ dissolves into the ambient brine, creating a solution that is denser than both initial fluids. The density increase triggers a Rayleigh–Bénard-type gravitational instability that enables mass transport through advection and diffusion—known here as convective mixing. Meanwhile, under reservoir conditions, the dissolution of CO₂ into brine also creates a solution that is acidic and can induce dissolution of minerals such as calcite (CaCO₃) through a series of geochemical reactions.

In the first part of this Thesis (Chapter 2), we study the morphology of rock dissolution patterns that develop from the interplay between reaction and density-dependent flow and ask the following questions: how do flow patterns translate into spatial organization of the permeability field through mineral dissolution? What is the evolution that leads to this pattern morphology? As rock dissolution alters local porosity and permeability, how does their change, in turn, affect flow and transport? We seek answers to these questions through high-resolution three-dimensional simulation of convective mixing in porous media coupled with carbonate geochemistry.

The problem requires modeling the flow and transport in porous media coupled to geochemical reactions; traditionally, this is described by a set of mass balance equations for the relevant chemical species, namely the ions and molecules participat-

ing in the chemical processes. Two independent time scales become relevant during a reactive-transport problem: the characteristic time of transport and the time to reach chemical equilibrium. When chemical reactions are slow compared to transport, a *kinetic* formulation of the reactions is often adopted to describe the rate of depletion/creation of chemical species along with the flow and transport problem. This requires solving a set of partial differential equations (PDEs) in a fully-coupled fashion. However, when reactions are much faster than transport, a kinetic formulation renders the problem computationally expensive as one needs to resolve the very fine time scale enforced by the fast chemical kinetics.

A workaround to this issue is possible if we consider that the chemical reactions are extremely fast: an instantaneous chemical equilibrium compared to the much slower flow and transport. Under the assumption of instantaneous chemical equilibrium, we adopt a formulation of the local reaction rate as a function of scalar dissipation rate—a measure that depends solely on flow and transport—and chemical speciation, which is a measure that depends only on the equilibrium thermodynamics of the chemical system. We use high-resolution simulations to examine the interplay between the density-driven hydrodynamic instability and the rock dissolution reactions, and analyze the impact of geochemical reactions on the macroscopic mass exchange rate. We find that dissolution of carbonate rock initiates in regions of locally high mixing, but that the geochemical reaction shuts down significantly earlier than shutdown of convective mixing. This early shutdown feature reflects the important role that chemical speciation plays in this hydrodynamics–reaction coupled process. Finally, we extend our analysis to three dimensions and explore the morphology of dissolution patterns in 3D.

1.2 Phase-field modeling of partially miscible fluids

Chemical reactions, such as the ones studied in Chapter 2, lead to the rearrangement of the molecular or ionic structure of a substance and a consequent destruction or creation of some phases (mineral dissolution/precipitation). Chemical reactions can be considered as a specific case under a broader definition of thermodynamic-driven reactions. A simpler example of a thermodynamic-driven process is the dissolution or exsolution of CO_2 gas bubbles in water. Depending on the concentration of dissolved CO_2 in water, a gas bubble can either dissolve to replenish or exsolve to extract the surrounding dissolved CO_2 . The CO_2 -water is an example of a fluid pair that is considered *partially miscible*: two fluids have limited (but nonzero) solubility into each other. Experimental and numerical studies of two-phase flow have focused on fluids that are either fully miscible (e.g. water and glycerol) or perfectly immiscible (e.g. water and oil). In practice, however, the miscibility of two fluids can change appreciably with temperature and pressure and often falls into the case of partial miscibility.

In Chapters 3 and 4, we develop a phase-field model for fluid-fluid displacements in a porous medium for two fluids that are partially miscible. In our model, partial miscibility is characterized through the design of the thermodynamic free energy of the two-fluid system. We express the model in dimensionless form and elucidate the key dimensionless groups that control the behavior of the system.

1.2.1 Thermodynamic coarsening arrested by viscous fingering in partially-miscible binary mixtures

In Chapter 3, we present high-resolution numerical simulations of the model to study the dynamics of vapor bubble interactions within an initially supersaturated liquid in a Hele-Shaw cell. Without background flow, we confirm that the vapor bubbles coarsen in size due to Ostwald ripening. Under periodic background flow, viscous in-

stability leads to continued break-up and coalescence of the less viscous vapor phase. As a result, we observe a shutdown in Ostwald coarsening and a time-invariant bubble-size distribution. Further, we explain that the interplay between thermodynamic effects and hydrodynamic instability leads to a system that is permanently driven away from thermodynamic equilibrium, in which the liquid phase is always supersaturated.

1.2.2 Viscous fingering with partially miscible fluids

In Chapter 4, we perform high-resolution numerical simulations to study the viscous fingering problem—the fluid-mechanical instability that takes place when a low-viscosity fluid displaces a high-viscosity fluid. This problem has traditionally been studied with either fully miscible or fully immiscible fluid systems. Here we study the impact of partial miscibility (a common occurrence in nature) on the fingering dynamics. By means of high-resolution numerical simulations, we show that partial miscibility exerts a powerful control on the degree of fingering: fluid dissolution hinders fingering while fluid exsolution enhances fingering. We also show that, as a result of the interplay between compositional exchange and the hydrodynamic pattern-forming process, stronger fingering promotes faster thermodynamic equilibrium.

1.3 Phase-field modeling of gas–liquid–hydrate systems

In the last part of this Thesis (Chapter 5), we discuss phase-field modeling of a gas–liquid–hydrate system under changing temperature or pressure conditions. We describe in detail how to extend the two-phase model developed in Chapter 3 and 4 to include a third solid phase (hydrate). Motivated by the temperature–composition phase diagram proposed for the real methane–water system, we present a *simulated* temperature–composition phase diagram based on our phase-field model that can capture the key phase behaviors in the natural system (Sec. 5.2). Using high-resolution simulations in 2D, we demonstrate the details of phase-separation dynamics in a

three-phase system that are often difficult to capture in experiments (Sec. 5.3–5.5). In the last three sections (5.6–5.7), we employ this theoretical phase-field modeling approach to explain observations of bubble expansion coupled with gas dissolution and hydrate formation in controlled laboratory experiments. Unraveling this coupling informs our understanding of the fate of hydrate-crusted methane bubbles ascending from seafloor seeps and the migration of gas pockets in hydrate-bearing sediments.

Chapter 2

Rock dissolution patterns and geochemical shutdown of CO₂-brine-carbonate reactions during convective mixing in porous media

Motivated by the process of CO₂ convective mixing in porous media, here we study the formation of rock-dissolution patterns that arise from geochemical reactions during Rayleigh–Bénard–Darcy convection. Under the assumption of instantaneous chemical equilibrium, we adopt a formulation of the local reaction rate as a function of scalar dissipation rate—a measure that depends solely on flow and transport—and chemical speciation, which is a measure that depends only on the equilibrium thermodynamics of the chemical system. We use high-resolution simulations to examine the interplay between the density-driven hydrodynamic instability and the rock dissolution reactions, and analyze the impact of geochemical reactions on the macroscopic mass exchange rate. We find that dissolution of carbonate rock initiates in regions of locally high mixing, but that the geochemical reaction shuts down significantly

earlier than shutdown of convective mixing. This early shutdown feature reflects the important role that chemical speciation plays in this hydrodynamics–reaction coupled process. Finally, we extend our analysis to three dimensions and explore the morphology of dissolution patterns in 3D. The results are published in the *Journal of Fluid Mechanics* (Fu et al., 2015).

2.1 Introduction

Convective mixing in porous media is an important process that has been studied extensively (Nield and Bejan, 2006). Recently, it has received renewed attention in the context of geologic sequestration of carbon dioxide (CO_2), a promising technology to mitigate climate change by reducing atmospheric greenhouse gas emissions (Lackner, 2003; Orr, 2009; Szulczewski et al., 2012). The sequestration process involves the capture of CO_2 from anthropogenic sources such as coal-fired and gas-fired power plants, the transportation after compression through a pipeline system and, finally, the injection of supercritical CO_2 into underground geologic formations such as deep saline aquifers (IPCC, 2005). Once it reaches a brine-saturated porous formation, CO_2 dissolves into the ambient brine, creating a solution that is denser than both initial fluids. The density increase triggers a Rayleigh–Bénard-type gravitational instability that enables mass transport through advection and diffusion—known here as convective mixing—rather than diffusion alone (Weir et al., 1996; Lindeberg and Wessel-Berg, 1997; Ennis-King and Paterson, 2005; Riaz et al., 2006). Convective mixing allows for faster solubility trapping of CO_2 into the brine, thus increasing storage security against leakage risks (MacMinn et al., 2011; Szulczewski et al., 2012).

Solubility trapping of CO_2 into groundwater at reservoir conditions (e.g. $p\text{CO}_2 \sim 10$ MPa, $T \sim 60^\circ\text{C}$) creates an acidic solution with $\text{pH} \sim 4$ (Xu et al., 2010). As suggested by recent core flood experiments on carbonate rock samples (Carroll et al., 2013; Elkhoury et al., 2013), interaction between the acidic CO_2 –brine solution and carbonate rocks leads to dissolution of minerals such as calcite (CaCO_3) through a series of geochemical reactions. Under constant flow conditions, rock dissolution may

lead to the formation of high-porosity channels in the core sample (Carroll et al., 2013). To put this in the context of CO₂ sequestration, as mineral dissolution occurs in response to the lowered pH in brine, this could result in a positive feedback that further drives the solubility trapping of CO₂ and mineral dissolutions (Xu et al., 2003). A recent study addressed this issue by performing a series of two-dimensional aquifer simulations that incorporate geochemistry into existing flow simulation software (Saaltink et al., 2013). They concluded that porosity changes due to calcite dissolution were relatively small in the scenario they studied.

Here, we revisit this problem using high-resolution simulation. The phenomenon of convective mixing has been studied through nonlinear simulations in two dimensions (e.g., Riaz et al., 2006; Hassanzadeh et al., 2007; Hidalgo and Carrera, 2009; Neufeld et al., 2010; Hidalgo et al., 2012; Szulczewski et al., 2013; Bolster, 2014; Slim, 2014), three dimensions (Pau et al., 2010; Fu et al., 2013), and experimental systems reproducing the conditions for a stationary horizontal layer (Neufeld et al., 2010; Kneafsey and Pruess, 2010; Backhaus et al., 2011; Slim et al., 2013) or a migrating buoyant current (MacMinn et al., 2012; MacMinn and Juanes, 2013). In the case of three-dimensional simulations, a striking self-organized network pattern is observed near the top boundary layer (Fu et al., 2013). Here, we study the morphology of rock dissolution patterns that develop from the interplay between reaction and density-dependent flow and ask the following questions: how do flow patterns translate into spatial organization of the permeability field through mineral dissolution? What is the evolution that leads to this pattern morphology? As rock dissolution alters local porosity and permeability, how does their change, in turn, affect flow and transport? We seek answers to these questions through high-resolution three-dimensional simulation of convective mixing in porous media coupled with carbonate geochemistry.

2.1.1 Decoupled formulation for multispecies reactive transport

The classic formulation of flow and transport in porous media coupled to geochemical reactions is a set of mass balance equations for the relevant chemical species, namely the ions and molecules participating in the chemical processes (Steefel and Lasaga, 1994):

$$\phi \frac{\partial c_i}{\partial t} + \nabla \cdot (\mathbf{u}c_i) - \nabla \cdot (\phi D \nabla c_i) = r_i \quad (i = 1, 2, \dots, N_{\text{tot}}), \quad (2.1)$$

where c_i is the mass concentration of species i , r_i is the source/sink term of species i due to chemical reactions (defined as the mass of species i produced/consumed in all participating reactions per unit volume and unit time), N_{tot} is the number of aqueous species, ϕ is porosity, \mathbf{u} is the Darcy velocity and D is the diffusion/dispersion coefficient. Equation (2.1) is then coupled with chemical reactions through appropriate relations for the source/sink term.

When chemical reactions are slow compared to transport—a *reaction-controlled* system—one can use a kinetic formulation for r_i to characterize the reactions. For example, a simplified kinetic formulation to describe precipitation/dissolution of a mineral takes the form (Steefel and Lasaga, 1994):

$$r_i = \xi K f(c_m), \quad (2.2)$$

where ξ is the reactive mineral surface area, K is the kinetic rate constant associated with dissolution/precipitation and $f(c_m)$ is some function of concentrations of the participating species (c_m). Kinetic formulations similar to Eq. (2.2) have been adopted to study dissolution patterns in fractured media (Detwiler and Rajaram, 2007) and formation of wormholes (Szymczak and Ladd, 2011a), both of which can exhibit slow chemical kinetics.

When reactions are fast, the problem becomes *transport-limited* because the reaction time scale is much smaller than the transport time scale. In the limit of instantaneous chemical equilibrium, the kinetic reaction rates become by definition

infinitely large, but the rates of production/consumption r_i remain bounded by the rate at which chemicals are brought in contact to sustain the reactions.

A challenging aspect of reactive transport simulation is the high computational cost as a result of the highly nonlinear nature of the coupled equations. To alleviate this computational burden, one can rewrite the mass balance equations through linear combinations to eliminate the source/sink terms in all but a small subset of the transport equations (Yeh and Tripathi, 1991; Steefel and MacQuarrie, 1996; Lichtner, 1996; Saaltink et al., 1998). Most reactive transport codes today employ variants of this split into primary and secondary chemical species (Yeh and Tripathi, 1991; Olivella et al., 1996; Saaltink et al., 2004; Xu et al., 2006; Hammond et al., 2012)

For the special case of geochemical systems described by instantaneous equilibrium reactions, one can reformulate the problem as a transport equation for a *conservative* species τ , defined as any quantity in the system that is unaffected by reactions.

$$\phi \frac{\partial \tau}{\partial t} + \nabla \cdot (\mathbf{u}\tau) - \nabla \cdot (\phi D \nabla \tau) = 0, \quad (2.3)$$

from which the rate of production/consumption r_i is determined by an analytical expression (De Simoni et al., 2005, 2007):

$$r_i = 2\phi F_i(\tau) (\nabla \tau \cdot D \nabla \tau). \quad (2.4)$$

Typical examples of the conservative variable τ include ionic charge (Andre and Rajaram, 2005), or a given element such as carbon (De Simoni et al., 2005).

Equation (2.4) consists of two τ -dependent factors, both of which control where and how much reaction occurs in a reactive transport system:

1. The chemical speciation function of species i . Chemical speciation refers to the distribution of a given element or ion amongst chemical species in the system. The speciation function of element/ion i , defined here as $F_i(\tau) = d^2 c_i / d\tau^2$ (De Simoni et al., 2007), describes the vigor of the chemical reactions at a given system state (i.e, for a given value of τ) and depends solely on the specifics

of the reactions. It can be calculated *offline*, therefore greatly reducing the computational cost of the simulation.

2. The scalar dissipation rate, $\varepsilon = \nabla\tau \cdot D\nabla\tau$, measures the local rate of fluid mixing as a result of fluid flow and transport.

Loosely speaking, r_i is controlled locally by both the chemistry and the fluid mechanics. This decoupled formulation (Eqs. (2.3)–(2.4)) has been shown to be a good approximation in systems with fast (but not instantaneous) reactions (Sanchez-Vila et al., 2007). It has been adopted by various authors to study reactions driven by fluid mixing, including calcite dissolution in coastal carbonate aquifers (Rezaei et al., 2005; Romanov and Dreybrodt, 2006; De Simoni et al., 2007) and numerical modeling of laboratory experiments of saltwater–freshwater mixing (Guadagnini et al., 2009). In our system, the time to reach geochemical equilibrium is estimated to be on the order of tens of hours, which is indeed small compared to the time for flow and transport over the natural length scale in a typical aquifer (see Appendix 2.A). In situations where local transport time is comparable to that of reaction, non-equilibrium effects can occur, although the finite-rate kinetics would have minimal effect for the parameter ranges we investigate in this study (Sanchez-Vila et al., 2007). The above assumptions allow us to adopt the decoupled approach, which also simplifies computation and offers insight into the interplay between geochemical and hydrodynamic processes.

2.2 Mathematical formulation

We consider a two-dimensional porous medium with square geometry composed mainly of carbonate rocks, or CaCO_3 (figure 2-1). The porous domain has impermeable boundaries at the top and bottom, and we assume periodicity in the lateral direction. The height of the square domain is denoted H . There are two participating solutions in the system; *solution 1* consists of brine saturated with CO_2 , and it enters the domain through the top boundary; *solution 2* is the ambient brine that initially fully saturates the porous medium. An important assumption we make in this formula-

tion is that both solutions are initially at chemical equilibrium with the carbonate formation. This assumption is justified because 1) the pH for *solution 1* is around 4, which indicates fast reaction with the carbonate; 2) *solution 2* is the ambient brine, which has already reached chemical equilibrium with the carbonate during its geologic residence time. This assumption distinguishes our formulation from the classical kinetic reaction behavior. Under this setup, neither solution 1 nor solution 2 alone will induce reactions; rather it is the mixing of the two solutions, which disturbs local chemical equilibrium, that triggers geochemical reactions and rock dissolution. We assume Boussinesq, incompressible Darcy flow through porous media (Nield and Bejan, 2006):

$$\nabla \cdot \mathbf{u} = 0, \quad \mathbf{u} = -\frac{k(\phi)}{\mu}(\nabla P - \rho g \mathbf{z}), \quad (2.5)$$

where \mathbf{u} is the Darcy velocity, k is permeability, μ is dynamic viscosity, P is pressure, ρ is fluid density, g is gravitational acceleration and ϕ is porosity. We adopt a simple cubic law for the permeability–porosity relationship, $k = k_0(\phi/\phi_0)^3$, where k_0 and ϕ_0 are the initial permeability and porosity, respectively. This relationship captures the evolution in permeability induced by porosity increase observed in laboratory experiments (Carroll et al., 2013).

We denote the density of solution 1 as ρ_1 and that of solution 2 as ρ_2 , where $\rho_1 > \rho_2$, and the density difference as $\Delta\rho = \rho_1 - \rho_2 > 0$. We define the mixing ratio α as the volumetric ratio of solution 1 in the mixture:

$$\alpha(x, z, t) = \frac{V_{\text{solution 1}}}{V_{\text{total}}}. \quad (2.6)$$

The density of the fluid mixture, ρ , increases linearly with the mixing ratio:

$$\rho = \rho_2 + \Delta\rho \alpha. \quad (2.7)$$

When the two solutions mix at α , chemical equilibrium is temporarily disturbed locally and the mixture undergoes a series of geochemical reactions to reach a new

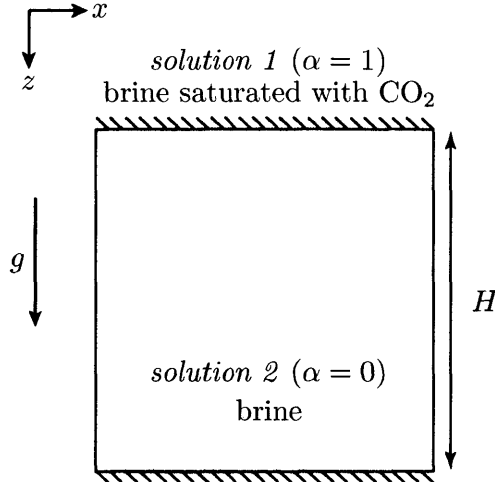
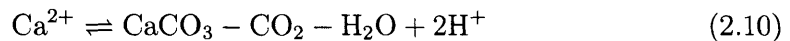


Figure 2-1: The problem is set up in a two-dimensional square homogeneous porous medium composed mainly of carbonate rocks. The domain is impermeable at the top and bottom. *Solution 1*, the equilibrated CO_2 -rich brine, enters via diffusion at the top of the formation, which is initially saturated with *Solution 2*, the equilibrated aquifer-brine.

equilibrium with calcite. While this process can be complicated by the participation of other co-existing minerals such as magnesite (MgCO_3) or gypsum ($\text{CaSO}_4 \cdot \text{H}_2\text{O}$), the dominant effect can be captured with the following four reactions (Sanford and Konikow, 1989; De Simoni et al., 2007):



Eight chemical species participate in these reactions, namely calcium carbonate (CaCO_3), water (H_2O), carbon dioxide (CO_2), hydrogen ion (H^+), bicarbonate (HCO_3^-), carbonate (CO_3^{2-}), calcium ion (Ca^{2+}) and hydroxide (OH^-). Adopting the approach in De Simoni et al. (2007) discussed in Sec. 2.1.1, we track the mixing ratio α , which is a conserved quantity in the system equivalent to τ in Eq. (2.3), using the

advection–diffusion equation:

$$\phi \frac{\partial \alpha}{\partial t} + \nabla \cdot (\mathbf{u}\alpha) - \nabla \cdot (\phi D \nabla \alpha) = 0, \quad (2.12)$$

where D is the diffusion/dispersion coefficient, taken here as constant. We assume here that D is the same for all chemical species in the system and is also the same as that of the fluid mixture. Using Eq. (2.4), we can then explicitly calculate the rate of calcite dissolution, which according to Eq. (2.10) is also the production rate for Ca^{2+} :

$$r = 2\phi F(\alpha) (\nabla \alpha \cdot D \nabla \alpha), \quad F(\alpha) = \frac{\partial^2 [\text{Ca}^{2+}]}{\partial \alpha^2}, \quad (2.13)$$

where $F(\alpha)$ is the speciation term associated with Ca^{2+} that we obtain *a priori* with a geochemical code such as PHREEQC (see Appendix 2.B). Equation (2.13) states that the local rate of porosity change is controlled by two mechanisms: (1) chemical speciation of calcium ion, $F(\alpha)$, which measures the vigor of the rock dissolution reaction in equation (2.10), and (2) strength of fluid mixing, which is measured in terms of scalar dissipation rate of α . Finally, we update porosity locally using the calcite dissolution rate r :

$$c_s \frac{\partial \phi}{\partial t} = r \Theta(\phi_1 - \phi), \quad (2.14)$$

where c_s is the molar density of calcite, and Θ is the Heaviside step function that limits the increase in porosity to a maximum value ϕ_1 , which accounts for the presence of residual minerals that are nonreactive in the system. Once ϕ reaches ϕ_1 locally, the assumption of chemical equilibrium fails since there is no more calcite to react with the un-equilibrated mixtures; nevertheless, we assume equilibrium for solutions that pass through the inert area. We keep this special case in mind and address its limitations when we interpret the results in section 2.3.2.

We choose as characteristic velocity the speed at which a fluid parcel sinks in the porous medium: $U_c = k_0 \Delta \rho g / \mu$. The natural length scale is the length over which diffusion and advection are balanced: $L = \phi D / U_c$. We choose to rescale the problem with this intrinsic length scale L as it is more relevant than domain height (H) for

characterizing local quantity changes. We set the other characteristic quantities as:

$$\rho_c = \Delta\rho, \quad P_c = \Delta\rho gL, \quad T_c = \frac{\phi_0 L}{U_c}, \quad \phi_c = \phi_0, \quad F_c = \max(|F(\alpha)|), \quad r_c = \frac{2\phi_0 F_c D}{L^2}.$$

Applying these scales, we obtain three dimensionless parameters: the dimensionless domain height $H = H/L$, the maximum relative porosity increase $R_\phi = \phi_1/\phi_0$, and the dissolution Damkhöler number:

$$\text{Da} = \frac{r_c T_c}{c_s \phi_0} = \frac{2F_c}{c_s}. \quad (2.15)$$

Since we use the intrinsic length scale here, the Rayleigh number ($\text{Ra} = U_c L/D$) is identically equal to one, and H plays the role of the traditional Ra (Hidalgo and Carrera, 2009). The dissolution Damkhöler number measures the competition between rock dissolution rate and solute transport velocity. In dimensionless form, the governing equations read:

$$\nabla \cdot \mathbf{u} = 0, \quad \mathbf{u} = -\phi^3(\nabla P' - \alpha \mathbf{z}), \quad (2.16)$$

$$\phi \frac{\partial \alpha}{\partial t} + \nabla \cdot (\mathbf{u} \alpha) - \nabla \cdot (\phi \nabla \alpha) = 0, \quad (2.17)$$

$$\frac{\partial \phi}{\partial t} = \text{Da} r \Theta(R_\phi - \phi/\phi_0), \quad r = \phi F(\alpha)(\nabla \alpha \cdot \nabla \alpha). \quad (2.18)$$

Here, P' is the dimensionless pressure with respect to a hydrostatic datum posed by ρ_2 . The boundary and initial conditions are:

$$\alpha(x, z = 0) = 1, \quad \left. \frac{\partial \alpha}{\partial z} \right|_{x, z=H} = 0,$$

$$\mathbf{u} \cdot \mathbf{n}(x, z = 0) = 0, \quad \mathbf{u} \cdot \mathbf{n}(x, z = H) = 0,$$

$$\phi(t = 0) = 1, \quad \alpha(t = 0) = 0.$$

We adopt a stream function–vorticity formulation for Eq. (2.16) (Tan and Homsy, 1988b; Riaz and Meiburg, 2003a; Fu et al., 2013) and solve for the stream functions with an eighth-order finite difference scheme, implemented with a fast Poisson solver

(Swarztrauber, 1977). To evaluate the derivatives used in the transport equation (Eq. (2.17)) and consumption rate (Eq. (2.18)(b)), we use sixth-order compact finite differences in the vertical direction (Lele, 1992) and a Fourier discretization along the horizontal direction, which we assume to be periodic. We integrate Eq. (2.17) and Eq. (2.18)(a) sequentially in time using a third-order Runge-Kutta scheme with dynamic time stepping (Ruith and Meiburg, 2000). We accelerate the onset of the gravitational instability by perturbing the initial mixing ratios at the top boundary with small white noise (an uncorrelated Gaussian random function).

2.3 Dissolution regimes

In this section, we describe dissolution patterns as a result of the reaction with calcite, and we illustrate the various dissolution regimes. Specifically, we focus on $\langle \Delta \phi \rangle$, the domain-averaged porosity increase, and $d\langle \alpha \rangle / dt$, the time derivative of the domain-averaged pore-volume ratio of solution 1 (the equilibrated CO₂-rich brine), or cumulative mass of solution 1 in the domain. We solve the governing equations for Damkhöler numbers up to 20 and values of H up to 6000 on a grid of 2500² cells. Convergence tests show that the required grid resolution increases super-linearly with the product of H and Da since both parameters have a combined effect on generating small-scale details.

2.3.1 Mixing-controlled dissolution patterns

The diffusive layer of solution-1-rich mixture near the top boundary becomes gravitationally unstable after some initial onset time, resulting in finger-like structures (figure 2-2, top left) that migrate downwards, stripping away the dense fluid (figure 2-2, middle left). Fingering dynamics and scaling relations have been studied extensively (Riaz et al., 2006; Hassanzadeh et al., 2007; Hidalgo and Carrera, 2009; Hidalgo et al., 2012; Hewitt et al., 2013; Slim et al., 2013; Slim, 2014) and will not be the focus of this work. The density-driven flow leads to mixing of fluids and triggers rock dissolution reactions which alter the permeability field. Initially, these reactions chisel

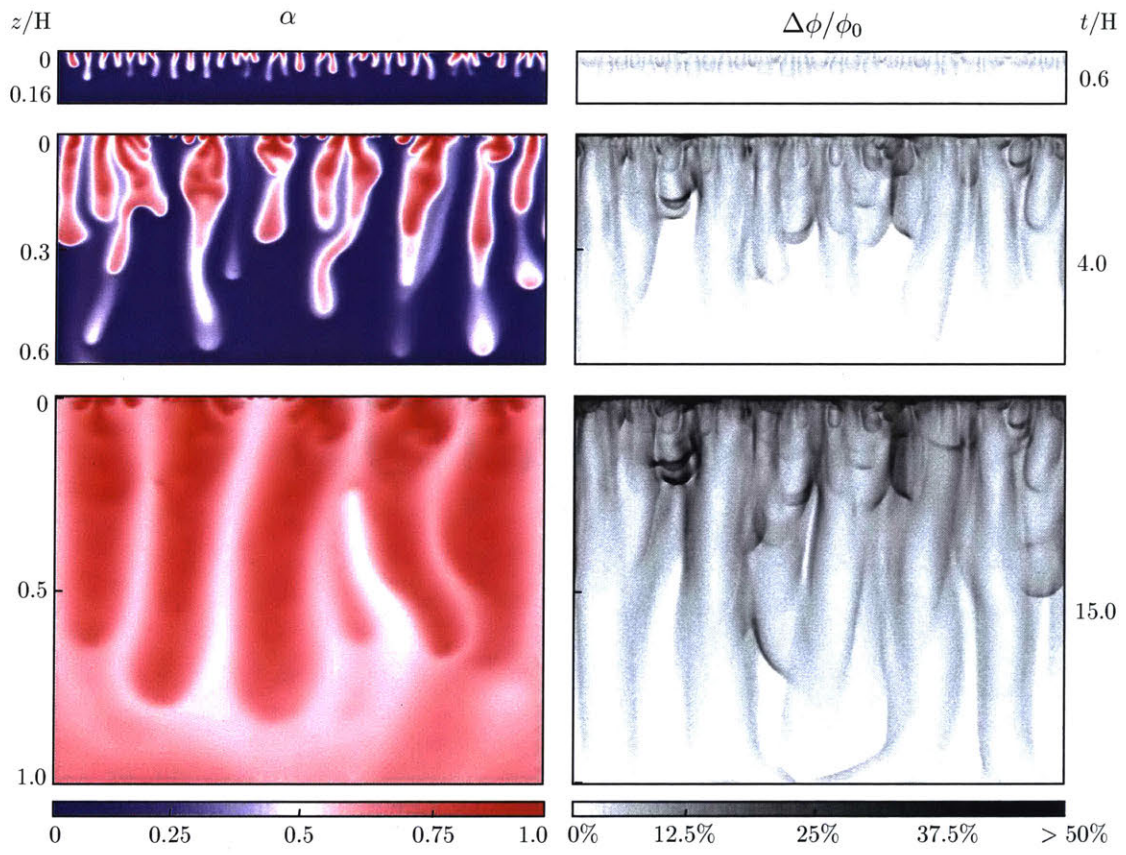


Figure 2-2: Snapshots of mixing ratio (left column) and porosity percentage increase (right column) for a simulation with $H=6000$, $Da=20$ and $R_\phi = 2$ at time $t = 0.6H$ (top), $4H$ (middle) and $15H$ (bottom).

out patterns that follow closely the interface of the fluid fingers, leaving the interior of these fingering channels almost unaffected (figure 2-2, top and middle right). The “hollowness” of the dissolution patterns can be understood as the direct consequence of a mixing-controlled dissolution rate (Eq. (2.4)). The rate of fluid mixing, as measured by the scalar dissipation rate, is strongest along finger interfaces where the concentration gradient is large (Hidalgo et al., 2012) and is weak within the core of the fingers, where concentration gradients are small. Over time, the rock dissolution patterns evolve in two ways:

- (a) *Elongation towards the bottom:* new fingers are continuously born at the top boundary; the cascade of fingers of different ages interact through a merging process where young fingers merge into old ones, small ones into bigger ones, allowing the surviving fingers to sink and coarsen laterally in size (Riaz et al., 2006; Hassanzadeh et al., 2007; Pau et al., 2010; Slim, 2014). As a result, finger-like dissolution channels continue to extend downwards and expand laterally (figure 2-2, bottom), following the locations of finger interfaces where mixing is strong.
- (b) *Focusing near the top:* while dissolution channels elongate towards the bottom due to downward migration of fingers, regions of high rock dissolution, or “dissolution hubs” start to appear near the top boundary (figure 2-2, bottom). These hubs develop as a result of repeated events of newly born fingers carrying $\alpha \approx 1$ meeting the upwelling plume of $\alpha \approx 0$, creating high concentration gradients that result in strong mixing and reaction.

2.3.2 Speciation-controlled reaction shutdown

The overall dissolution pattern is controlled by fluid mixing, as evidenced by the spatial correlation between the permeability and mixing fields. However, the magnitude of permeability increase, or how much reaction occurs when the two fluids mix, is set by the shape of the speciation term $F(\alpha)$. As shown in figure 2-11 in appendix B, $F(\alpha)$ for our geochemical system is a highly nonlinear function, showing that reaction is favored in the lower range of mixing ratios ($\alpha < 0.1$); when $\alpha > 0.2$, $F(\alpha)$ becomes

so small that regardless of the strength of local mixing, almost no reaction will take place. The behavior of this speciation curve is crucial for explaining the system's evolution.

For a simulation with $H=6000$, $Da=20$, we track the domain-averaged porosity increase $\langle \Delta\phi \rangle$ with time, and find that after a period of monotonic growth, $\langle \Delta\phi \rangle$ reaches a plateau, indicating a *shutdown* of dissolution reactions globally (figure 2-3(a)). We compute the time for dissolution shutdown, $t_{sd}^{\Delta\phi}$, as the time when $\langle \Delta\phi \rangle$ reaches 95% of the plateau value, denoted $\langle \Delta\phi \rangle_{sd}$; the shutdown times are shown as dark circles in figure 2-3(a). We next track the domain-averaged speciation term over time and find that it also flattens out towards zero after some period of time. We compute the corresponding time for speciation shutdown, $t_{sd}^{F(\alpha)}$, shown as dark circles in figure 2-3(b), as the time when $\langle F(\alpha) \rangle$ falls below 0.02. Shutdown time for dissolution corresponds closely to that of speciation (figure 2-3(a) and (b), dark circles) and this shutdown happens much earlier than the decaying of global degree of mixing (figure 2-3(c)). In other words, while reaction-inducing fluid mixing is still active in the system, the fast decay of chemical speciation has caused the dissolution reactions to stop at a much earlier time. We refer to this as a *speciation-controlled* reaction shutdown. The concept of convective shutdown was coined in the context of the one-sided convection system to describe the effect of domain saturation on the mass flux (Hewitt et al., 2013). Here, we find a shutdown in reaction caused by the decay of chemical speciation, not the loss in strength of the convective instability.

We extend the above analysis to a range of values of H and Da , and find that the plateau value $\langle \Delta\phi \rangle_{sd}$ scales linearly with Da (figure 2-3(d)):

$$\langle \Delta\phi \rangle_{sd} \sim Da, \quad (2.19)$$

which is a consequence of the role that Da plays in the porosity-update equation (Eq. (2.18)(a)). The shutdown time for dissolution and speciation both decrease with increasing Da (figure 2-3 (e) and (f)). This is because as Da increases, the permeability near the top boundary increases faster, allowing fluid to enter and saturate the domain

faster, and leading to an earlier speciation shutdown (see further discussion in Sec. 2.4). We find that H , on the other hand, has little impact on $\langle \Delta\phi \rangle_{sd}$ and $t_{sd}^{\Delta\phi}$, an observation that is consistent with the fact that the rate of fluid mixing is independent of H (Hidalgo et al., 2012).

We analyze the time series of the porosity field and find that the maximum porosity ϕ_1 is reached locally for simulations with large Da and H after some initial period of dissolution and this critical time arrives later for smaller Da and H . This indicates that the special case of non-equilibrium state as discussed in section 2 is indeed present in some of our simulations. For small enough Da and H (e.g. $H=2000$ with any Da ; $H=4000$ with $Da=1$; $H=6000$ with $Da=1$), however, ϕ_1 is not reached anywhere. When ϕ_1 is reached, we find that the spatial spread of the non-equilibrium state is focused near the top boundary and accounts for a small portion of the domain, between 0.17% and 0.69%. This suggests that non-equilibrium effects are not critical in our examples. However, such non-equilibrium effect could be more important for simulations with large Damkhöler numbers as the maximum ϕ could be reached early on in the simulation and impact larger areas.

2.4 Impact on the macroscopic mass exchange rate

The macroscopic mass exchange rate measures how fast solution 1, the equilibrated CO_2 -rich brine at the top, enters the formation and mixes with the resident brine. It is a quantity of special interest in the context of geologic carbon sequestration as it determines the effectiveness of solubility trapping. Previous studies that do not account for geochemical reactions (Hassanzadeh et al., 2007; Pau et al., 2010; Hidalgo et al., 2012; Hewitt et al., 2013; Slim et al., 2013; Slim, 2014) have shown that the exchange rate, often referred to as the CO_2 flux, reaches a plateau after the onset of instability and remains constant until domain saturation starts to impact the top boundary, at which point the flux decays (figure 2-4, $Da=0$). Further, it has been shown that this constant flux is independent of the domain size H (Hidalgo et al., 2012; Slim, 2014). We address here how these observations change in the presence of

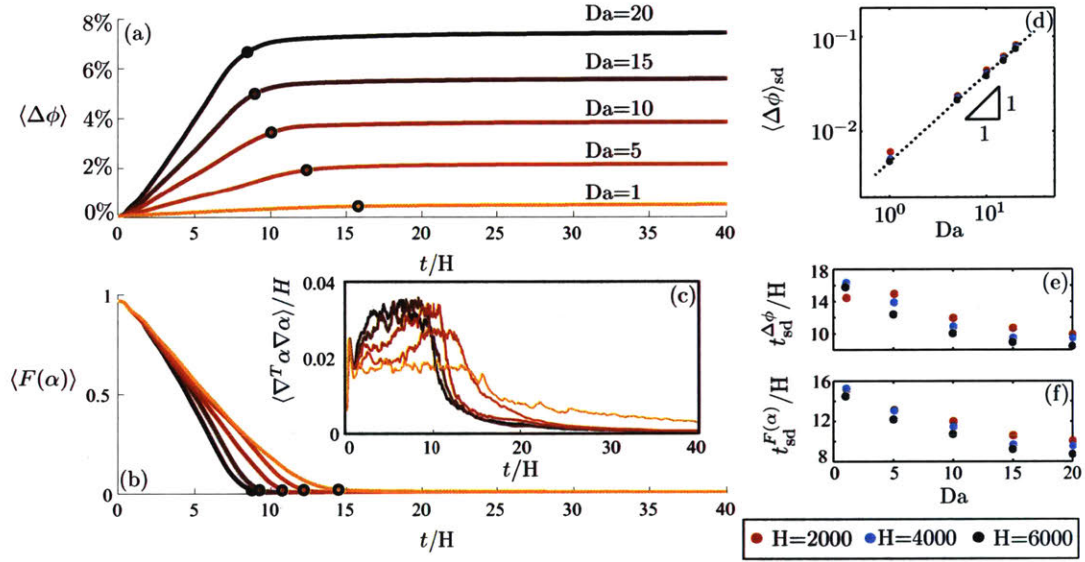


Figure 2-3: Volume-averaged measures of (a) percentage increase in ϕ (b) chemical speciation and (c) scalar dissipation rate over time for a simulation with $H=6000$. The transition in curve color from light orange to dark indicates increase in Da . The dark circles in (a) and (b) indicate the shutdown time $t_{sd}^{\Delta \phi}$ and $t_{sd}^{F(\alpha)}$, respectively, as defined in Sec. 2.3.2. (d) Cumulative (volume-averaged) porosity increase plotted against Da for different values of H (red, blue and black). (e) and (f) $t_{sd}^{\Delta \phi}$ and $t_{sd}^{F(\alpha)}$ plotted against Da for different values of H .

rock dissolution reactions.

We define the mass exchange rate as the volumetric flux of solution 1, $d\langle\alpha\rangle/dt$, which we calculate by taking numerical derivative of $\langle\alpha\rangle$ with respect to t . For simulations with fixed H (e.g. $H=6000$) and $Da>1$, we observe significant differences with respect to the nonreactive case. Instead of reaching a plateau after the onset of convection, the flux continues to grow with time as a result of increasing permeability from rock dissolution near the top (figure 2-4, top); the rate of flux increase grows with Da . When Da is sufficiently large (e.g. $Da=20$), the increase in $d\langle\alpha\rangle/dt$ hits a ceiling early on (figure 2-4, top, $Da=20$); this is because the relative porosity increase $\langle\Delta\phi\rangle$ at the top has reached R_ϕ and cannot increase further. In all cases, with or without reaction, the flux ultimately decays due to the effect of domain saturation and, as shown in figure 2-4, the flux decays at earlier times as Da increases. This is, again, because an increase in permeability leads to a more convective system that can reach saturation faster. These observations are largely independent of the values of H (figure 2-4, bottom), similar to what we observe in Sec. 2.3.2.

2.5 Dissolution patterns in three dimensions

We simulate equations (2.16)–(2.18) with the same boundary and initial conditions in three dimensions, for a case with $H=2500$, $Da=5$ and $R_\phi=2$ with a grid resolution of 368^3 cells. The numerical scheme is the same as that for 2D, where we use Fourier discretization in the x and y directions and compact finite differences in the z -direction. Similar to the 2D results, the reaction shuts down at around $t/H=8$. We present the final morphology (at $t/H=14$) of dissolved rock in figure 2-5. As the 3D columnar fingers move downwards—see more details in Fu et al. (2013)—they chisel out columnar-shaped regions along the finger-brine interfaces (figure 2-5(a)) as a result of the high local concentration gradients. Underneath the top boundary layer, the interiors of fingers are barely affected by reaction (figure 2-7, (b)–(f), black-white frames). These empty columns are analogous to the hollow channels observed in 2D (see Sec. 2.3.1). At the top boundary we observe the same dissolution hubs as seen

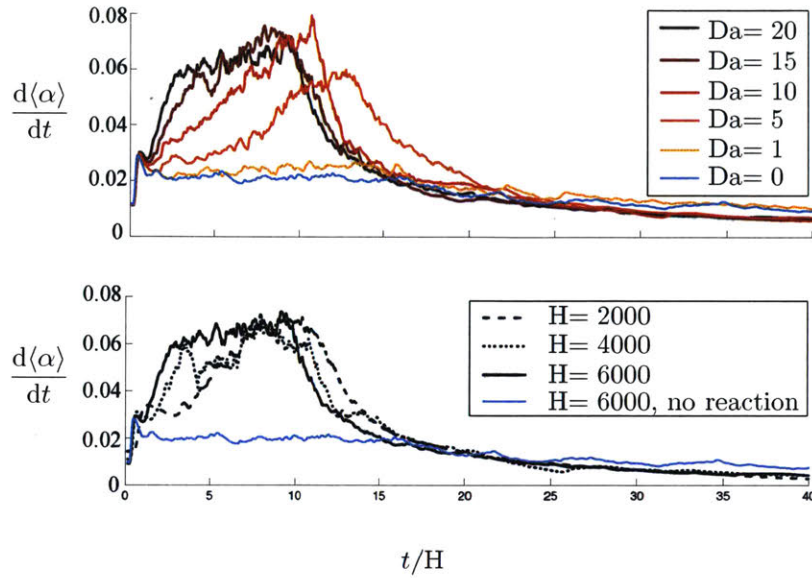


Figure 2-4: Volume-averaged measure of mass exchange rate of solution 1 for increasing Damköhler numbers with $H=6000$ (top) and for three values of H with $Da=20$ (bottom). The blue curves in both figures correspond to the case with $H=6000$ and without reaction ($Da=0$).

in 2D (Sec. 2.3.1); here, they take the shape of upside-down dunes, scattered and hanging from the top surface (figure 2-5(b)).

While 3D visualization gives insight into the morphology of the rock dissolution patterns, it provides limited quantitative details. To obtain more information about the interior structure of the dissolution morphology, we plot horizontal slices of $\Delta\phi/\phi_0$ at six depths: $z/H = 0.01$ (top boundary layer), $z/H = 0.14, 0.27, 0.54$ and 0.82 (the bulk) and $z/H = 1.0$ (bottom). As fingers start to arrive at a given depth, circular rings of dissolved rock emerge within the horizontal plane, reflecting the shape of fingering plumes at those depths. With the exception of the top boundary layer ($z/H = 0.01$), the dissolved rings continue to expand laterally to form a tessellation of polygons. The polygons are “hollow” inside and separated from each other by a clearly-defined polygonal network of undissolved edges (figure 2-7(b)-(f), black and white frames). Once the tessellation has evolved into its full form, usually within $\Delta t = 2500$ after the fingers invade that depth, the pattern “freezes” in time due to a drastic reduction in dissolution activity.

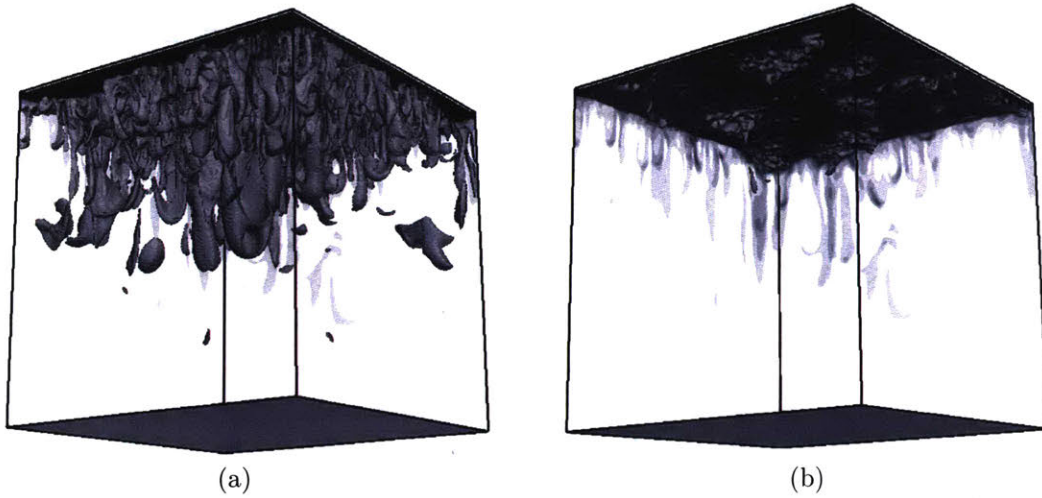


Figure 2-5: Dissolution patterns in 3D: for a simulation of $H=2500$, $Da=5$ and $R_\phi=2$, at $t/H = 14.0$, this figure shows surface contours for (a) $\Delta\phi = 4\%$ and (b) $\Delta\phi = 8\%$.

We track the dissolution rate at each depth as a function of time—denoted here as $d\langle\phi\rangle_z/dt$, where $\langle\cdot\rangle_z$ is the average across the x - y plane—and observe that the dissolution rates peak at around the time that dissolution structures “freeze” at that depth (figure 2-6). Similar to earlier observations in 2D (Sec. 2.3.2), the “freezing” of rock dissolution structures is a consequence of a speciation-controlled reaction shutdown: once fingers arrive at a given layer, dissolution reactions take place for a short period of time; once the layer becomes weakly saturated with α (e.g. $\langle\alpha\rangle_z > 0.1$), the reactions stop. Figure 2-6 also clearly demonstrates the temporal dynamics of the shutdown process: instead of occurring all at once, the shutdown takes place at later times for deeper layers. Overall, this provides us with a more mechanistic description on how these tessellation patterns evolve: as fingers arrive at each layer, they imprint their “images” through mineral dissolution onto the porosity field; once the reaction shuts down, the dissolution pattern becomes immune to further alterations by fingering dynamics.

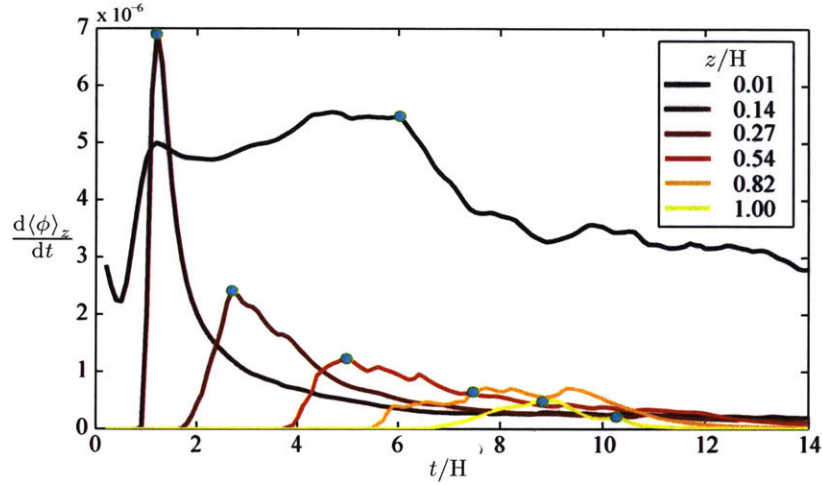


Figure 2-6: Dissolution rate (laterally averaged) at various depths over time. Cyan-colored dots correspond to the “freezing” events, which is around the time that the tessellation pattern at that depth adopts its final configuration.

2.5.1 Coarsening of dissolution patterns

Finger coarsening in nonreactive convective mixing has been observed and quantified in both experimental studies (Backhaus et al., 2011; MacMinn and Juanes, 2013) and simulations (Fu et al., 2013; Hewitt et al., 2013; Slim et al., 2013). The dynamics of coarsening are different in the boundary layer and within the bulk. Near the top boundary, finger roots initially coarsen through a series of merging events but then reaches a statistical steady state, where the finger root spacing stands at a quasi-steady value (Fu et al., 2013; MacMinn and Juanes, 2013). On the other hand, finger coarsening in the bulk persists throughout the entire lifetime of the falling fingers (MacMinn and Juanes, 2013). In this work, because dissolution structures are directly linked to the spatial arrangement of fingers, it is not surprising to find that the dissolution patterns also coarsen with depth (figure 2-7), much in the same way that fingers coarsen in the bulk. Here, we quantify this coarsening by counting the number dissolved polygonal rings (N_{polygon}) as a function of depth (z), as seen in figure 2-7 (black and white frames) at $t = 14$ (figure 2-8). The analysis shows that

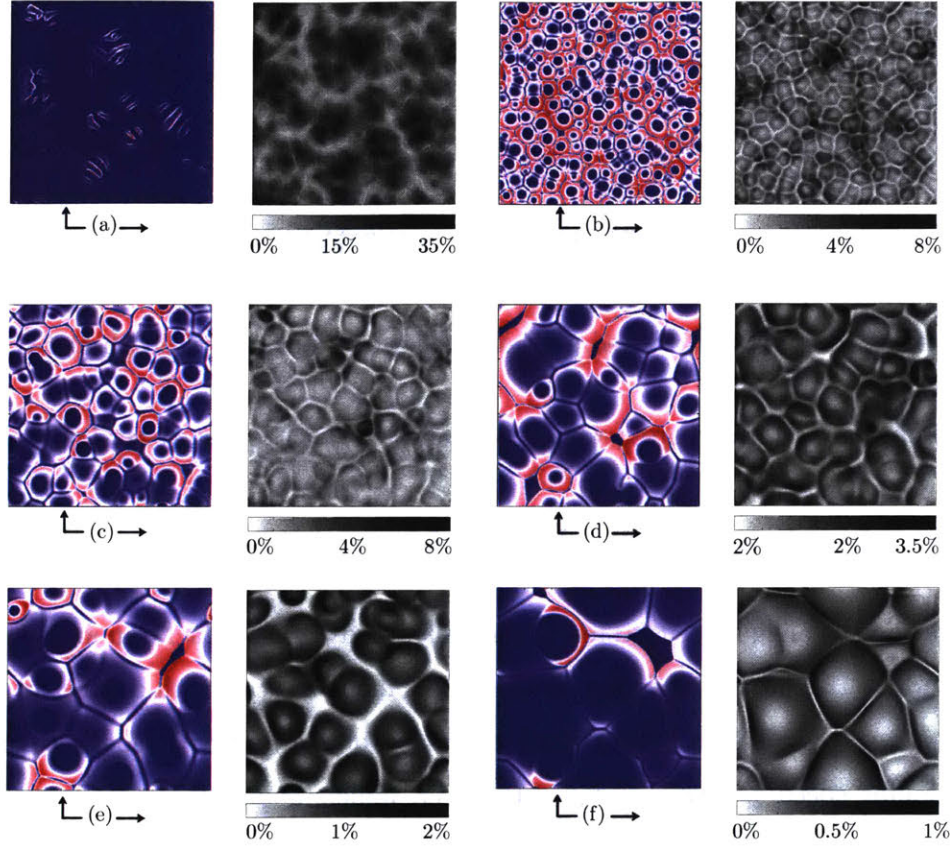


Figure 2-7: Horizontal slices of the reaction rate $r = \phi F(\alpha) \nabla \alpha \cdot \nabla \alpha$ (color frames) and the relative porosity increase $\Delta\phi/\phi_0$ (black and white frames) at different depths: (a) $z/H = 0.01$, (b) $z/H = 0.14$, (c) $z/H = 0.27$, (d) $z/H = 0.54$, (e) $z/H = 0.82$ and (f) $z/H = 1.0$. The color frames for r are at different times: (a) $t/H = 6.0$, (b) $t/H = 1.2$, (c) $t/H = 2.7$, (d) $t/H = 5.0$, (e) $t/H = 7.8$ and (f) $t/H = 10.1$ (subtracted from a background image corresponding to $t/H = 8.9$ for clarity). Red color indicates high value (colormap not shown). The black and white frames for $\Delta\phi/\phi_0$ are all at time $t/H = 14.0$. The colormap range varies with depth to best reflect the dissolution structure.

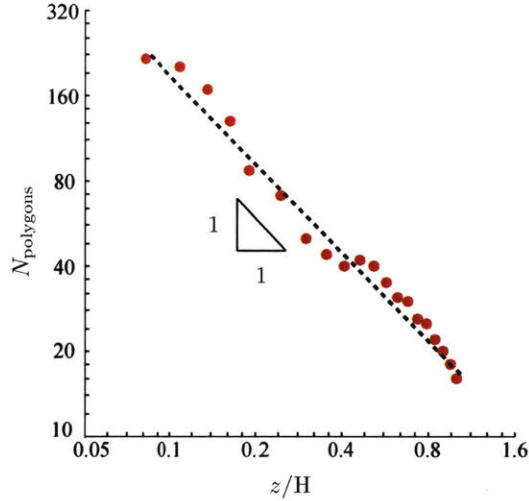


Figure 2-8: Number of dissolved polygonal rings as a function of depth at $t = 14$.

the dissolution patterns coarsen with depth, and exhibit a robust power-law scaling:

$$N_{\text{polygon}} \sim z^{-1}. \quad (2.20)$$

The above scaling was suggested by an earlier study in 2D (MacMinn and Juanes, 2013), where the number of fingers in the bulk is found to scale with convective time as: $N_{\text{fingers}} \sim t_{\text{conv}}^{-1}$. This is indeed consistent with Eq.(2.20) if we consider a constant finger falling speed so that $z \sim t_{\text{conv}}$. However, understanding the mechanism that leads to such scaling remains a future task in this study.

2.6 Summary

In this paper, we study rock dissolution as a result of geochemical reactions during convective mixing in porous media, in the context of CO_2 sequestration. To couple geochemistry with flow and transport, we assume a mixing-limited reactive transport system where reactions reach chemical equilibrium instantaneously compared to the transport time scale. This allows us to adopt a formulation that completely decouples transport from reaction, and describes the local reaction rate as a function of scalar dissipation and chemical speciation (De Simoni et al., 2005). Using high-resolution

simulations, we investigate the interplay between flow and reaction as a result of local permeability changes from rock dissolution. Because the reactive system we study here is mixing-limited, we find that the rate of rock dissolution is initially high in regions of high fluid mixing, which leads to dissolution patterns that closely follow the structure of the mixing field. However, geochemical reactions shut down much earlier than convective mixing shuts down; a result of the highly nonlinear behavior of chemical speciation. This feature of a *speciation-controlled* shutdown highlight the important role that the details of the geochemical equilibrium play in this hydrodynamics–reaction coupled process.

In both 2D and 3D simulations, we find that rock dissolution focuses on the top boundary, leaving the rock in the rest of the domain almost undissolved. As a result of the porosity increase at the top, we observe a significant increase in the rate at which the denser fluid enters the domain. This increase in solubility rate could enhance the effectiveness of CO₂ trapping in the context of a migrating plume (MacMinn et al., 2011). In the bulk, we see weak coupling from the rock dissolution patterns to the fingering dynamics, since the permeability increase is small below the boundary layer. We investigate the dissolution morphology in 3D and observe that the pattern at each depth exhibits a polygonal tessellation structure. This structure corresponds closely to the spatial arrangement of columnar fingers, and it also coarsens with depth in a similar way that convective fingers coarsen with time in the bulk of the domain.

2.A Comparison between time to reach chemical equilibrium and characteristic time of transport

The following analysis is specific to the chemical system in Eqs. (2.8)–(2.11) but can be extended to other systems as well. We first estimate the time to reach chemical equilibrium when solution 1 and 2 are mixed at a given α . We use the KINETICS data block in PHREEQC (Parkhurst (1995)) and the Plummer-Wigley-Parkhurst

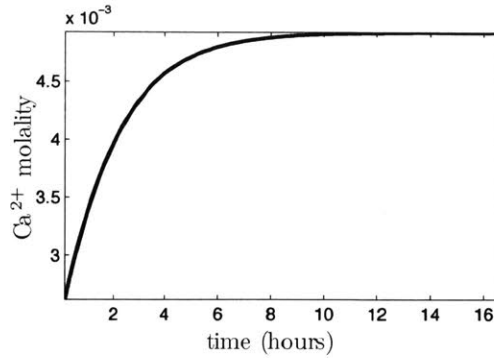


Figure 2-9: When solution 1 and 2 mix at $\alpha = 0.01$, concentration of Ca^{2+} in the mixed solution increases over time as the mixture equilibrates over course of tens of hours.

rate model for calcite dissolution (Plummer et al. (1978)). Figure 2-9 plots calcium ion concentration over time for a mixture of $\alpha = 0.01$, showing that equilibrium is reached at around $t = 10$ hours. We confirm with additional kinetic simulations that equilibrium is reached within tens of hours for all values of α (not shown here).

We estimate the characteristic transport time across the natural length scale of the diffusive boundary layer $L_{\text{diff}} \approx 120\phi D/U$ to be on the order of thousands of hours or more for a typical aquifer ($U = \Delta\rho g k/\mu$ is the characteristic velocity, where $k = 10^{-13}\text{m}^2$, $D = 10^{-9}\text{m}^2/\text{s}$, $\Delta\rho = 10\text{kg}/\text{m}^3$, $\mu = 0.8 \times 10^{-3}\text{kg}/\text{m} \cdot \text{s}$). We obtain the coefficient of 120 in L_{diff} by directly measuring the boundary layer thickness from 3D simulations. To quantify the boundary layer thickness, we sample the vertical concentration profile, at $t = 5$, and at five different horizontal locations; we repeat the sampling for different Rayleigh numbers (figure 2-10a). We then define the boundary layer thickness as the depth below which the concentration is smaller than $c = 0.3$. With this, we calculate the boundary layer thickness for each sample and obtain the average thickness for each Rayleigh number (figure 2-10b). The fitted straight line in figure 2-10(b) suggests that

$$\log_{10} \left(\frac{L_{\text{diff}}^*}{\text{Ra}} \right) = -\log_{10}(\text{Ra}) + 2.08,$$

which yields $L_{\text{diff}}^* \approx 120$, or $L_{\text{diff}} \approx 120\phi D/U$.

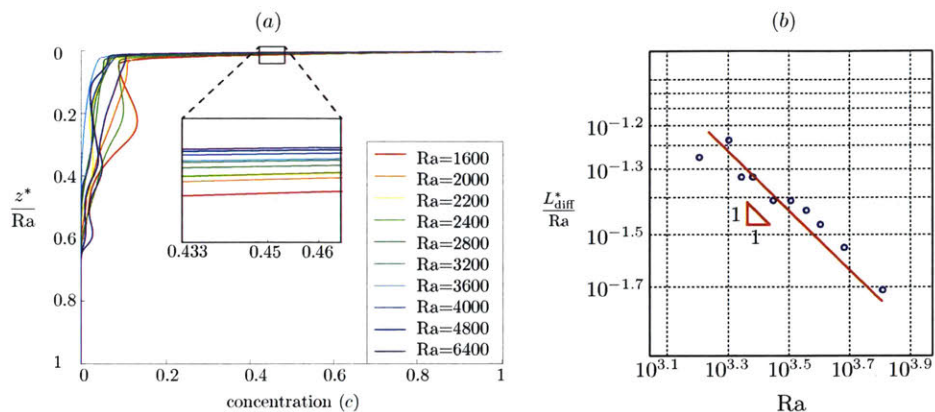


Figure 2-10: (a) Vertical concentration profiles at $t = 5$ for different Rayleigh numbers. We only show one sample of each Rayleigh number here while the analysis is done using ensemble of 5 samples for each Rayleigh number. Here $z^* = z/L$, where L is the natural length scale. (b) Average thickness of boundary layer, $L_{\text{diff}}^* = L_{\text{diff}}/L$, as a function of Rayleigh numbers.

2.B Geochemical speciation curve

We use PHREEQC (Parkhurst, 1995) to obtain the speciation curve corresponding to the chemical system in equations (2.8)–(2.11). To do so, we first define the composition of solution 1 and solution 2, which are the two fluids that participate in the mixing. To obtain solution 1, the equilibrated CO_2 -rich brine, we subject pure water at $\text{pH} = 7$ and $T = 60^\circ\text{C}$ to equilibrium with gaseous CO_2 at $\text{pCO}_2 = 10^2$ atm and with calcite. To obtain solution 2, the equilibrated aquifer-brine, we subject also pure water at $\text{pH} = 7$ and $T = 60^\circ\text{C}$ to equilibrium with gaseous CO_2 at $\text{pCO}_2 = 10^{-1}$ atm and with calcite. Then, for one thousand, preselected and equally-spaced values of α , PHREEQC performs the speciation calculation by first mixing solutions 1 and 2 at volume fraction α and then re-equilibrating the mixed solution with respect to CaCO_3 . At the end of each calculation, we obtain the value of calcium molality ($[\text{Ca}^{2+}]$) in the final mixed-and-equilibrated solution corresponding to that given mixing ratio (figure 2-11, inset). Finally, we calculate the speciation curve by taking the second derivative of the molality curve numerically (figure 2-11, solid curve).

The equilibrium constants of reactions in Eq. (2.8)–(2.11) are: $K_1 = 10^{6.3447}$,

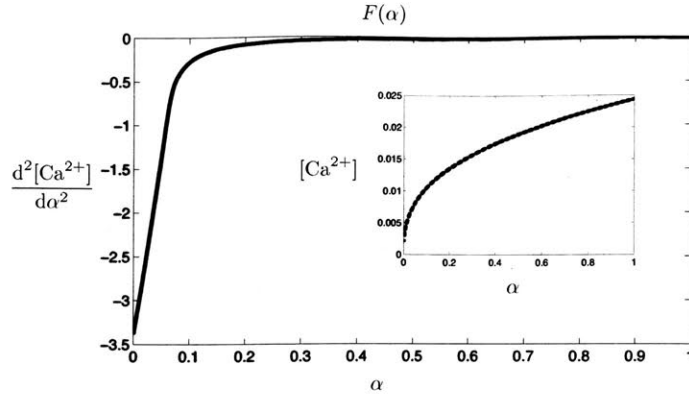


Figure 2-11: Speciation curve $F(\alpha)$ obtained from PHREEQC. The dashed line (inset) is the calcium molality ($[\text{Ca}^{2+}]$) versus α . The solid line (main plot) is the second derivative, computed numerically, of the dashed line.

$K_2 = 10^{16.6735}$, $K_3 = 10^{-8.1934}$ and $K_4 = 10^{13.9951}$ respectively (Parkhurst, 1995). These equilibrium constants are corrected by the species activities γ_i , modeled using the extended Debye–Hückel equation (Helgeson and Kirkham, 1974):

$$\log \gamma_i = \frac{Az_i^2 \sqrt{I_s}}{1 + \overset{\circ}{a}_i B \sqrt{I_s}} + \overset{\circ}{b} I_s, \quad (2.21)$$

where I_s is the ionic strength of the mixture characterized by α , z_i and $\overset{\circ}{a}_i$ are the valence and the ionic radius of species i , respectively, and $\overset{\circ}{b}$, A and B are constants set by PHREEQC.

Chapter 3

Thermodynamic coarsening arrested by viscous fingering in partially-miscible binary mixtures

In this Chapter, we study the evolution of binary mixtures far from equilibrium, and show that the interplay between phase separation and hydrodynamic instability can arrest the Ostwald ripening process characteristic of non-flowing mixtures. We describe a model binary system in a Hele-Shaw cell using a phase-field approach with explicit dependence of both phase fraction and mass concentration. When the viscosity contrast between phases is large (as is the case for gas and liquid phases), an imposed background flow leads to viscous fingering, phase branching and pinch-off. This dynamic flow disorder limits phase growth and arrests thermodynamic coarsening. As a result, the system reaches a regime of statistical steady state in which the binary mixture is permanently driven away from equilibrium. The results are published in *Physical Review E* (Fu et al., 2016).

3.1 Introduction

Spinodal decomposition is the process by which a thermodynamically unstable mixture separates into two phases. The signature feature of this process is coarsening:

the characteristic length scale of phase separation grows algebraically with time (Furukawa, 1985; Voorhees, 1992; Bray, 1995). Thermodynamic coarsening—first studied in the context of solid alloys (Ostwald, 1900; Voorhees, 1992)—can be fundamentally altered in fluid mixtures by means of hydrodynamic effects that lead to more complex dynamics. For instance, hydrodynamic coalescence due to curvature-induced pressure differences can enhance the coarsening rate (Siggia, 1979; Wagner and Yeomans, 1998). Under uniform shear flow, a highly anisotropic layered phase ordering appears in the mixture (Min and Goldberg, 1993; Hashimoto et al., 1995; Shou and Chakrabarti, 2000). Under turbulent flow, experiments (Pine et al., 1984; Tong et al., 1989) and numerical simulations (Berti et al., 2005; Perlekar et al., 2014) have shown that coarsening is suppressed due to vigorous stirring, a result that is also observed when a chaotic flow is imposed (Berthier et al., 2001).

These observations arise from the coupling of a phase-ordering process (promoting coarsening) to a velocity field with *externally imposed* strong disorder (suppressing coarsening) (Berthier et al., 2001). The paradigmatic model used to investigate this process is the advective Cahn–Hilliard equation coupled to the incompressible Navier–Stokes equations (Ruiz and Nelson, 1981; Berthier et al., 2001; Berti et al., 2005; Perlekar et al., 2014). In this case, the Navier–Stokes equations contain a capillary term that embodies gradients in chemical potential, and thereby a feedback from the phase-evolution equation. This term alone, however, is insufficient to suppress coarsening—on the contrary, the main observation is that, in an unstirred fluid, domain growth of the phase-separating field is enhanced (Berti et al., 2005).

In this Chapter, we set to elucidate whether thermodynamic coarsening can be arrested by the coupling between phase-ordering and hydrodynamics in the absence of external mechanical forcing. We study spinodal decomposition of a binary fluid mixture driven by Darcy flow, such as flow in a Hele-Shaw cell (a thin gap between two parallel plates) or porous media. Our interest is in systems that naturally phase-separate into phases of very different viscosity (as is typical of liquids and gases). Under these conditions, two relevant effects set in. On one hand, there is strong feedback between phase ordering and fluid velocity via a phase-dependent mixture viscosity.

On the other, the well-known viscous fingering hydrodynamic instability (Saffman and Taylor, 1958a; Paterson, 1981; Maher, 1985; Homsy, 1987) induces phase branching, splitting and pinch-off (Arnéodo et al., 1989; Lajeunesse and Couder, 2000; Cueto-Felgueroso and Juanes, 2014). While many aspects of viscous fingering have been studied—including its role on fluid mixing (Jha et al., 2011, 2013; Chen et al., 2015) and ensuing chemical reactions (De Wit, 2001; Nagatsu et al., 2014; Haudin et al., 2014)—its impact on phase separation of a fluid mixture remains unexplored.

A complicating factor in fluid binary mixtures is that miscibility can change appreciably with the ambient conditions, which often introduces compositional effects to two-phase problems. In previous studies of spinodal decomposition coupled to flow, fluid phase is inferred from composition, and not independently described (Ruiz and Nelson, 1981; Wagner and Yeomans, 1998; Shou and Chakrabarti, 2000; Berthier et al., 2001; Berti et al., 2005; Perlekar et al., 2014). The free energy of such mixtures is formulated as a functional of molar fractions and their gradients and, in its simplest setting, the coarsening dynamics is described by a Cahn–Hilliard equation (Cahn and Hilliard, 1958). Here, in contrast, we consider *partially miscible* systems—components can exchange between the two phases and, therefore, fluid concentrations evolve independently from the phase variable. During spinodal decomposition, our mixture phase-separates into domains with different compositions, accompanied by redistribution of composition between phases. Describing such mixture requires having separate evolution equations for phase and concentration, and defining a free energy that is a function of both variables. Analogous two-field approaches have been extensively adopted in the simulation of solidification of binary alloys Wheeler et al. (1993); Karma (2001); Boettinger et al. (2002); Folch and Plapp (2005); Plapp (2011). By adopting this more general framework, we investigate the two-way coupling between thermodynamics (compositional phase behavior and phase ordering) and hydrodynamics (viscously unstable Darcy flow), and find that the system reaches a statistical steady state in which viscous fingering not only arrests phase growth, but also drives the mixture away from compositional equilibrium permanently.

3.2 Mathematical model

We develop a phase-field model of two-phase flow with two-component transport. Without loss of generality, we focus on a binary mixture that is an analogy for a $\text{CO}_2(g)$ -water(l) system. The two fluids, denoted *gas* (g) and *liquid* (l), have different viscosities with $\mu_l > \mu_g$. Upon contact, they seek to reach compositional equilibrium through mutual component exchange. The result should be a gas phase that is rich in the primary component (e.g. CO_2) and a liquid that is rich in the secondary component (e.g. H_2O). We introduce two variables, defined pointwise, to describe the state of the binary mixture: the gas volume fraction, ϕ , is a nonconserved quantity due to dissolution/expansion of the gas phase; the molar fraction of CO_2 , c , is conservative in the entire domain. The model describes the evolution of ϕ and c when the binary mixture is subjected to hydrodynamic instabilities.

3.2.1 Phase-field modeling of two-phase Darcy flow with compositional effects

We introduce the following dimensional governing equations to describe incompressible, isothermal, two-phase flow with two-component transport in a Hele-Shaw cell, with a uniform gap thickness b :

$$\nabla \cdot \mathbf{u} = 0, \quad \mathbf{u} = -\frac{k}{\mu(\phi)} \nabla P, \quad (3.1)$$

$$\frac{\partial \phi}{\partial t} + \nabla \cdot (\mathbf{u}\phi) + \lambda^\phi \Psi_\phi = 0; \quad (3.2)$$

$$\frac{\partial c}{\partial t} + \nabla \cdot (\mathbf{u}c) - \nabla \cdot (\lambda^c \nabla \Psi_c) = 0. \quad (3.3)$$

Equations (3.1) are the continuity equation for an incompressible mixture and Darcy's law, where \mathbf{u} is the mixture velocity, P is a kinematic pressure, k is a constant permeability and μ is the mixture viscosity, assumed to follow an exponential dependence on phase fraction, $\mu(\phi) = \mu_g \exp(R(1 - \phi))$, where $R = \log(\mu_l/\mu_g)$ is the viscosity

contrast.

In the context of phase-field modeling, we understand ϕ also as a phase variable, which takes a value of 1 in the gas and 0 in the liquid, and interpolates smoothly between the two bulk phases over a well-resolved, diffuse numerical interface. Time evolution of ϕ simulates gas dissolution/exsolution [Eq. (3.2)], and can be considered a relaxation process towards a minimum of the free energy function of the system F (Hohenberg and Halperin, 1977). The gradient towards minimization, obtained by taking the variational derivative of F with respect to ϕ , can be understood as a phase potential that drives phase-transformations:

$$\Psi_\phi \equiv \delta F / \delta \phi = \partial F / \partial \phi - \nabla \cdot [\partial F / \partial (\nabla \phi)]. \quad (3.4)$$

The dynamics of phase transformation [Eq. (3.2)] are formulated using Allen–Cahn dynamics (Allen and Cahn, 1979). The evolution of c is described by a nonlinear advection–diffusion equation [Eq. (3.14)], where the component diffusion is driven by gradients in chemical potentials, defined similarly to Eq. 3.4:

$$\Psi_c \equiv \delta F / \delta c = \partial F / \partial c - \nabla \cdot [\partial F / \partial (\nabla c)]. \quad (3.5)$$

In Eqs. (3.2) and (3.3), λ^ϕ and λ^c are mobilities for ϕ and c respectively. Here we assume that both mobilities are only a function of c :

$$\lambda^{\phi b^2} = \lambda^c = \frac{D\nu}{R_{\text{ideal}}T}(c(1-c) + 0.01), \quad (3.6)$$

where D is the diffusion coefficient, ν is the kinematic viscosity, R_{ideal} is the ideal gas constant and T is temperature (assumed constant here). We define the characteristic composition mobility as:

$$\lambda_c = \frac{D\nu}{R_{\text{ideal}}T}, \quad (3.7)$$

and the characteristic phase mobility as:

$$\lambda_c^\phi = \frac{D\nu}{b^2 R_{\text{ideal}} T}. \quad (3.8)$$

3.2.2 Design of free energy

The free energy functional $F(\phi, c)$ plays a central role in the thermodynamic behavior of our binary mixture. Following the classical Cahn–Hilliard formulation for a binary system (Cahn and Hilliard, 1958), our F subsumes interfacial and bulk energy contributions:

$$F(\phi, c) = \int_V \left\{ \frac{1}{2} \epsilon_\phi^2 T (\nabla \phi)^2 + \frac{1}{2} \epsilon_c^2 T (\nabla c)^2 + \omega T W(\phi) + \omega_{\text{mix}} T [f_l(c)(1 - g(\phi)) + f_g(c)g(\phi)] \right\} dV. \quad (3.9)$$

The first two terms in Eq. (3.9) capture the interfacial energy associated with phase and compositional boundaries. The characteristic interfacial energy per unit volume associated with ϕ and c are $\epsilon_\phi^2 T$ and $\epsilon_c^2 T$ respectively. The third term is the part of the bulk free energy responsible for phase separation, where $W(\phi) = \frac{1}{4} \phi^2 (1 - \phi)^2$ adopts the shape of a double-well, determining the two stable states of F : $\phi = 0$ or $\phi = 1$. Here, ω is the energy (per unit volume) associated with the double-well energy. The last term, known as the bulk mixing energy, is the part of the bulk free energy responsible for partially miscible behavior. We adopt a form for mixing energy that is commonly used in the field of binary alloy solidification (Wheeler et al., 1993), where the energy is an interpolation in ϕ between liquid and gas excess energies (f_l and f_g), which are functions of c only. Here, $\omega_{\text{mix}} T$ is the energy (per unit volume) associated with mixing. The interpolation function $g(\phi) = -\phi^2(2\phi - 3)$ satisfies that the system approaches the stable states $\phi = 0, 1$ with zero slope, which ensures positivity of the phase variable (Wheeler et al., 1993). The excess free energy of each phase are due to compositional effects; here we adopt the Wilson model (Wilson, 1964):

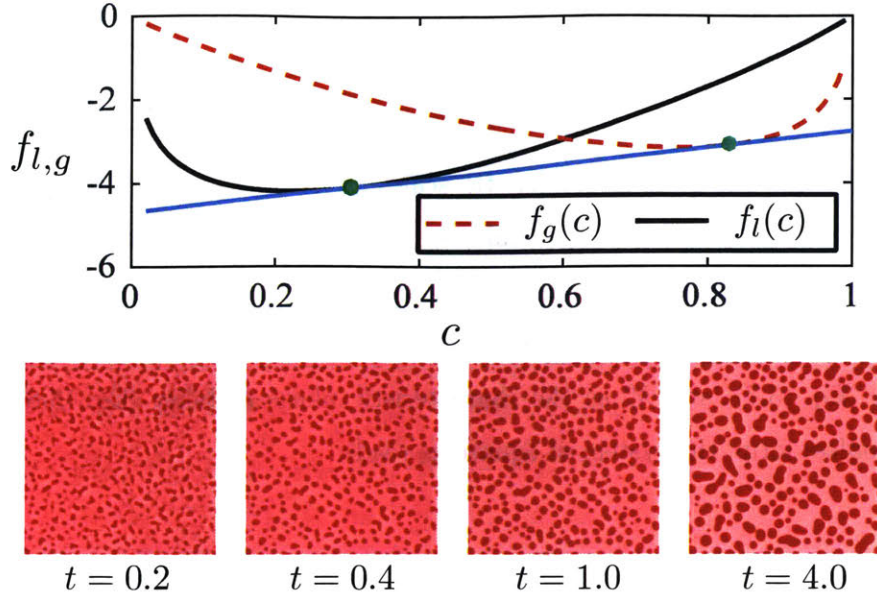


Figure 3-1: (Top) The common tangent construction (blue line) on the bulk free energy of pure phases yields the equilibrium concentrations (green circles) within gas and liquid. For parameters $\alpha_l=1$, $\beta_l=500$, $\alpha_g=200$, $\beta_g=2\times 10^{-4}$, the equilibrium compositions are $c_l^{\text{eq}}\approx 0.304$ and $c_g^{\text{eq}}\approx 0.828$. (Bottom) Zoomed-in snapshots of c illustrate the process of spinodal decomposition of a domain that is initially filled with supersaturated liquid ($t=0$). The progression shows vapor bubbles (high c , red-colored) that nucleate and coarsen out of the liquid phase (low c , pink-colored).

$$f_l(c) = c \log c + (1 - c) \log(1 - c) \quad (3.10)$$

$$- c \log(c + \alpha_l(1 - c)) - (1 - c) \log(1 - c + \beta_l c),$$

$$f_g(c) = c \log c + (1 - c) \log(1 - c) \quad (3.11)$$

$$- c \log(c + \alpha_g(1 - c)) - (1 - c) \log(1 - c + \beta_g c).$$

The equilibrium concentrations within each phase are then obtained by the common tangent construction of f_l and f_g (Bray, 1995; Witelski, 1996) (Fig. 3-1 top). Note here that both $f_l(c)$ and $f_g(c)$ are dimensionless.

3.2.3 Scaling analysis

We identify the following characteristic scales in our system: $\epsilon_\phi^2 T/b^2$ is the characteristic energy, b is the length scale, $t_c = b/u_c$ is the characteristic time with $u_c = (k_c \Delta p_c)/(\mu_g b)$, where k_c , Δp_c are the characteristic permeability and pressure drop respectively. Additionally, we introduce λ_c as the characteristic composition mobility [Eq. (3.7)] and λ_c^ϕ as the characteristic phase mobility [Eq. (3.8)]. In its dimensionless form, the system of equations reads:

$$\nabla \cdot \mathbf{u} = 0, \quad \mathbf{u} = -\frac{1}{\mu(\phi)} \nabla P, \quad (3.12)$$

$$\frac{\partial \phi}{\partial t} + \nabla \cdot (\mathbf{u}\phi) + \frac{1}{\text{Ca}} \lambda \Psi_\phi = 0, \quad (3.13)$$

$$\frac{\partial c}{\partial t} + \nabla \cdot (\mathbf{u}c) - \frac{1}{\text{Pe}} \nabla \cdot (\lambda \nabla \Psi_c) = 0. \quad (3.14)$$

where $\mu(\phi) = e^{R(1-\phi)}$ and $\lambda = 0.01 + c(1 - c)$. The first dimensionless group, the capillary number Ca , sets the ratio between time scales associated with phase change and advection:

$$\text{Ca} = (u_c b)/(\lambda_c^\phi \epsilon_\phi^2 T), \quad (3.15)$$

where $\epsilon_\phi^2 T/b$ is the interfacial tension. We expect that Ca controls the characteristic length scale of the instability pattern, such that the characteristic length decreases with increasing Ca (Fu et al., 2016). The second dimensionless group, the Péclet number, sets the ratio between rate of advection and diffusion:

$$\text{Pe} = (u_c b)/(\lambda_c \epsilon_\phi^2 T). \quad (3.16)$$

Pe controls the rate of diffusion within a single phase, and therefore directly affects the rate of gas dissolution/exsolution. We expect that for large values of Pe , the finger morphology will approach that of an immiscible system. In dimensionless form, the

free energy is described with three additional dimensionless groups:

$$F(\phi, c) = \int_V \left\{ \frac{1}{2}(\nabla\phi)^2 + \epsilon \frac{1}{2}(\nabla c)^2 + \frac{1}{\text{Ch}}W(\phi) + \frac{1}{\text{Ma}} [f_i(c)(1 - g(\phi)) + f_g(c)g(\phi)] \right\} dV. \quad (3.17)$$

We introduce the third dimensionless group as the ratio between the two energy scales associated with compositional and phase boundaries:

$$\epsilon = \epsilon_c^2 / \epsilon_\phi^2. \quad (3.18)$$

An increase in ϵ would mean that the numerical profile of concentration (c) becomes sharper and the numerical profile of phases (ϕ) becomes smoother. The fourth group is the Cahn number, which controls the thickness of the numerical interface:

$$\text{Ch} = (\epsilon_\phi^2 / b^2) / \omega. \quad (3.19)$$

A larger Ch would require more grid points to resolve the fluid-fluid interface. Phenomenologically, a larger Ch also corresponds to a system with larger surface tension. Finally, we define a solutal Marangoni number, which sets the ratio between interfacial energy and mixing energy:

$$\text{Ma} = (\epsilon_\phi^2 / b^2) / \omega_{\text{mix}}. \quad (3.20)$$

As Ma increases, the system becomes dominated by interfacial effects and we expect non-equilibrium thermodynamics to play a weaker role in the pattern forming process.

3.3 Problem statement

We conduct high-resolution numerical simulations of this compositional phase-field model. We solve Eqs. (3.12)–(3.14) sequentially: first obtaining the velocity using the streamfunction-vorticity formulation (Tan and Homsy, 1988b; Riaz and Meiburg, 2003a); then updating c and ϕ using a Fourier pseudo-spectral discretization and

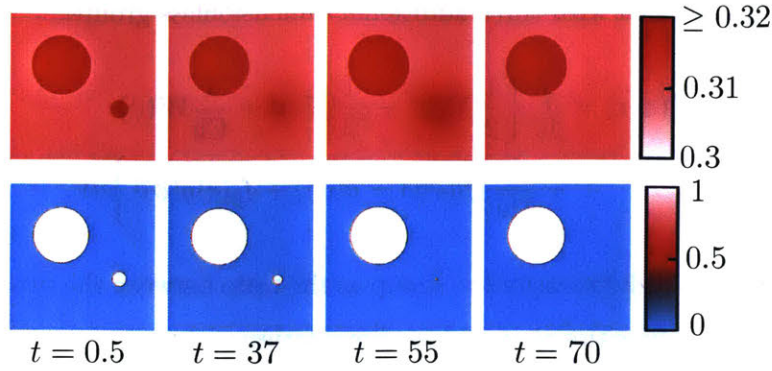


Figure 3-2: Snapshots of c (top) and ϕ (bottom) illustrating the Ostwald ripening process in a system with a small and a large vapor bubble, in a liquid bath that is initially at local equilibrium.

using a biharmonic-modified time stepping (Bertozzi et al., 2011). Our simulations are on a bi-periodic square domain of size 160×160 and parameter values $Ca=2$, $Pe=32$, $Ch=1/400$, $Ma=1/40$ and $\epsilon=8$ (and parameters of the Wilson model given in Fig. 3-1, top). The domain is initially filled with liquid phase that is supersaturated: $\phi(x, y, t=0)=0$, $c(x, y, t=0)=0.36 \pm 0.1$. We perturb the initial concentration field with random uncorrelated noise to promote nucleation of gas bubbles. The supersaturated liquid is thermodynamically unstable and undergoes spinodal decomposition almost immediately, where the domain phase-separates into vapor bubbles surrounded by liquid (Fig. 3-1, bottom).

3.4 Coarsening in gas-liquid mixtures by Ostwald ripening

Ostwald ripening is an out-of-equilibrium process in which large phase domains grow at the expense of smaller ones, by virtue of minimizing interfacial energy (Ostwald, 1900; Voorhees, 1992). To illustrate the ability of our model to reproduce this well known phenomenon, we simulate two vapor bubbles of different sizes in a liquid bath, and initialize the system to be at compositional equilibrium locally within each phase: $c_l=c_l^{\text{eq}}$, $c_g=c_g^{\text{eq}}$ (Fig. 3-2). Despite the initial local-equilibrium configuration,

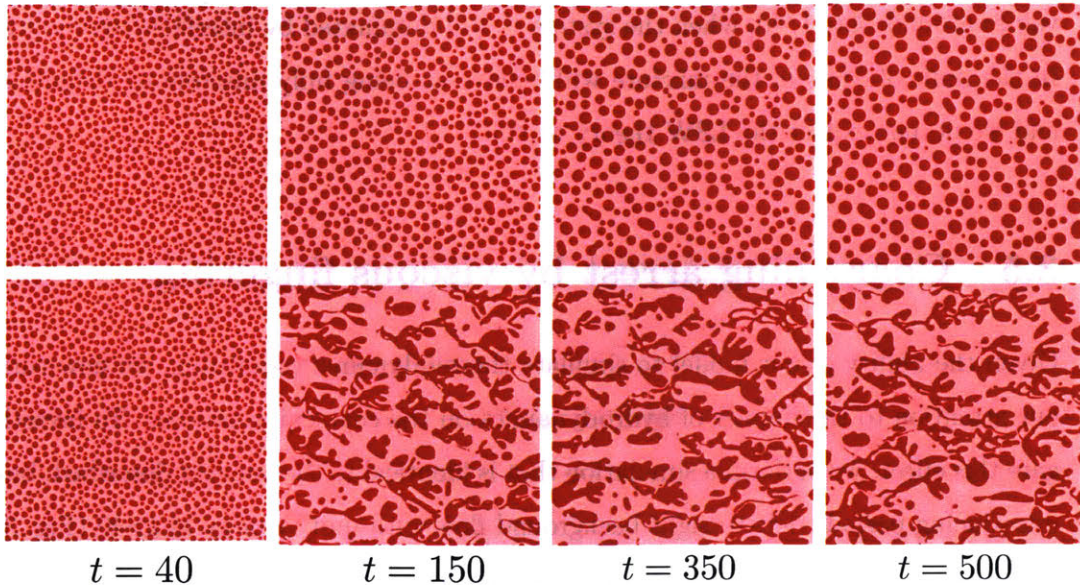


Figure 3-3: Snapshots of c at $t=40, 200, 300$ and 400 , under no flow (top) and with periodic left-to-right flow imposed at $t>40$ (bottom).

the smaller bubble dissolves into the liquid phase, leaving a patch of excess concentration that diffuses into the larger bubble, expanding its size (the larger bubble, in turn, develops a rim of undersaturated liquid around it). Over the entire process, the total gas volume fraction in the domain is unchanged.

It is well known that, as a result of Ostwald ripening, an initially nucleated domain will coarsen continuously (Fig. 3-3, top) until it consists of a single large bubble (not shown here), thereby minimizing the system's interfacial energy and chemical potential gradients. Here, we define r as the square root of the area of an individual vapor bubble. We obtain information on individual bubbles through image segmentation of the ϕ -field and compute $\langle r \rangle$ as the average length scale associated with a given domain image. We find a power-law scaling of the coarsening dynamics: $\langle r \rangle \sim t^{1/3}$ (Fig. 3-4a), indicative of diffusive-growth regime. The bubble-size distribution, $f(r)$, is time-independent when scaled by $\langle r \rangle$ (Fig. 3-4b). Both observations are in agreement with the Lifshitz–Slyozov–Wagner theory (Lifshitz and Slyozov, 1961; Wagner, 1961; Yao et al., 1993; Fan et al., 2002) of Ostwald ripening in 2D. We confirm with additional simulations (not shown here) that the power-law scaling holds for other

values around $Ma=1/40$, when the system is still dominated by interfacial dynamics. In the limit of $Ma=0$, the mixture will behave as being fully miscible by definition and we do not expect the LSW theory to hold.

3.5 Coarsening arrest by viscous fingering

Given the ability of our model to simulate thermodynamic coarsening, we now turn our attention to the impact of hydrodynamics on the coarsening process. To investigate this effect, we perform a simulation that is identical to the one just described, but introducing periodic left-to-right background flow with unit velocity at $t>40$ (Fig. 3-3, bottom). The unfavorable viscosity contrast between liquid and gas ($\mu_l/\mu_g=20.9$) leads to viscous fingering, a hydrodynamic instability when a low-viscosity fluid displaces a high-viscosity fluid (Saffman and Taylor, 1958a; Paterson, 1981; Maher, 1985; Homsy, 1987). This leads to phase branching and tip splitting (Arnéodo et al., 1989; Lajeunesse and Couder, 2000), which in our case destabilize the leading edge of gas bubbles and induce pinch-off events (Lee et al., 2002b; Cueto-Felgueroso and Juanes, 2014). As a result, vapor bubbles undergo persistent breakup and coalescence. The dynamic disorder in the phase field feeds back to the flow field through a phase-dependent viscosity Eq. (3.12), leading to the intrinsic emergence of a dynamic and highly heterogeneous flow field. By virtue of this interplay, coarsening is arrested immediately, and the system enters a statistical steady state characterized by a relatively constant arrest length scale (Fig. 3-4a) and a time-independent bubble-size distribution $f(r)$; the new distribution is more skewed, featuring a dominant presence of smaller-than-average bubbles (Fig. 3-4c). We confirm with additional simulations (not shown here) that the emergence of an arrest length scale is not observed in a fully miscible system under similar flow dynamics (Jha et al., 2011), and the effect of Korteweg stress (Chen and Meiburg, 1996; Chen et al., 2001) alone is not able to retain an arrest length scale in fully miscible mixtures.

We study the dependence of the emerging characteristic arrest length scale $\overline{\langle r \rangle}$ (time-averaged $\langle r \rangle$ during the statistical steady state) on Ca and Pe . The fundamen-

tal observation is the strong power-law decay of $\overline{\langle r \rangle}$ with Ca, and a weaker decay with Pe (Fig. 3-4d). Filtering the dependence $\sim \text{Pe}^{-0.078}$ (Fig. 3-4e, inset) allows us to robustly collapse the data as a function of Ca, $\overline{\langle r \rangle} \sim \text{Ca}^{-0.443}$ (Fig. 3-4e). This power-law behavior indicates that in the regime dominated by interfacial dynamics (Ca>1), the dependence of the emerging length scale on Ca is congruent with the one predicted by linear stability analysis of classical immiscible viscous fingering, $\sim \text{Ca}^{-0.5}$ (Homsy, 1987). We postulate that the discrepancy in the observed exponents is due to thermodynamic coarsening effects.

3.6 Permanent supersaturation in liquid phase by hydrodynamic stirring

The interplay between the hydrodynamic instability (viscous fingering) and thermodynamic coarsening (Ostwald ripening) in partially miscible mixtures turns out to have surprising macroscopic consequences. Let $\langle c_l \rangle = \iint c(1 - \phi) dx dy / \iint (1 - \phi) dx dy$ be the domain-averaged liquid phase concentration and compare $\langle c_l \rangle$ vs. t for both simulations (Fig. 3-5). In the absence of background flow, $\langle c_l \rangle$ approaches the theoretical saturation of $c_l^{\text{eq}} \approx 0.304$ from the initial supersaturation level of $\langle c_l \rangle = 0.36$. The ultimate steady state, where $\langle c_l \rangle = c_l^{\text{eq}}$, is only reached when Ostwald ripening culminates the coarsening process in a single vapor bubble (not shown here). Under background flow, in contrast, the approach towards compositional equilibrium is interrupted as soon as flow is introduced, and $\langle c_l \rangle$ fluctuates about a steady state value that, surprisingly, is above the local-equilibrium concentration: $\langle c_l \rangle \approx 0.312 > c_l^{\text{eq}}$.

We propose the following mechanism to explain the observed supersaturation in the liquid (Fig. 3-5, insets). The viscous instability leads to recurrent pinch-off of small bubbles from large patches of vapor. A newly formed small bubble is quickly consumed by surrounding larger bubbles due to Ostwald ripening. This is achieved, as shown in Fig. 3-2, by small bubbles first dissolving into the liquid. The mass transfer into large bubbles is limited by diffusion, implying that if the rate of bub-

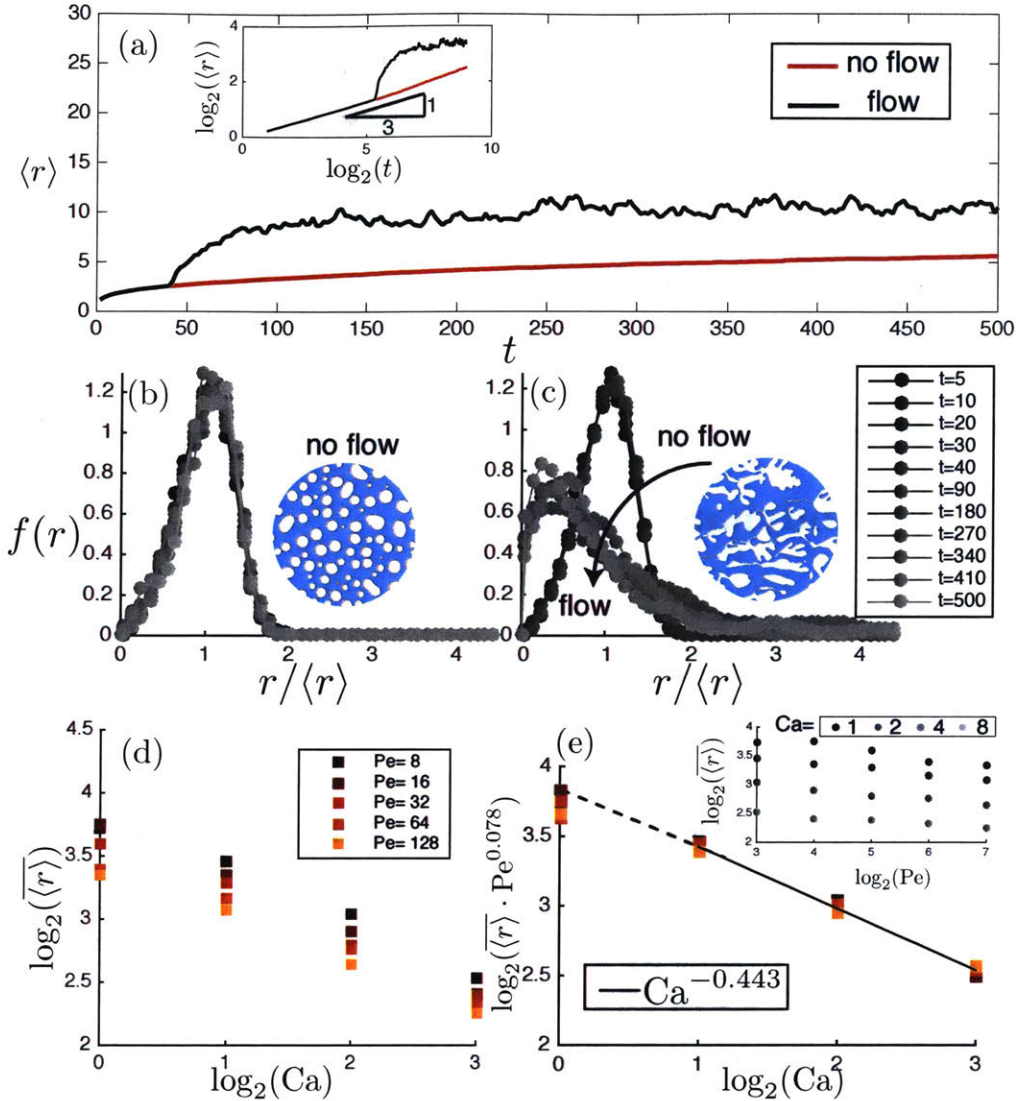


Figure 3-4: (a) $\langle r \rangle^2$ vs. t for simulations without flow (dashed red line) and with background flow after $t = 40$ (solid black line), emphasizing arrest of thermodynamic coarsening in the presence of flow. Inset: $\langle r \rangle$ vs. t in log-log scale, emphasizing algebraic growth of spinodal decomposition ($\langle r \rangle \sim t^{1/3}$) in the absence of flow. (b–c) Normalized distribution of $r/\langle r \rangle$ at sampling times for simulations without flow (b) and with flow introduced at $t = 40$ (c). (d) $\langle r \rangle$ vs. Ca for different Pe . (e) $\langle r \rangle$ rescaled with $Pe^{-0.078}$ vs. Ca . Inset: $\langle r \rangle$ vs. Pe for different Ca .

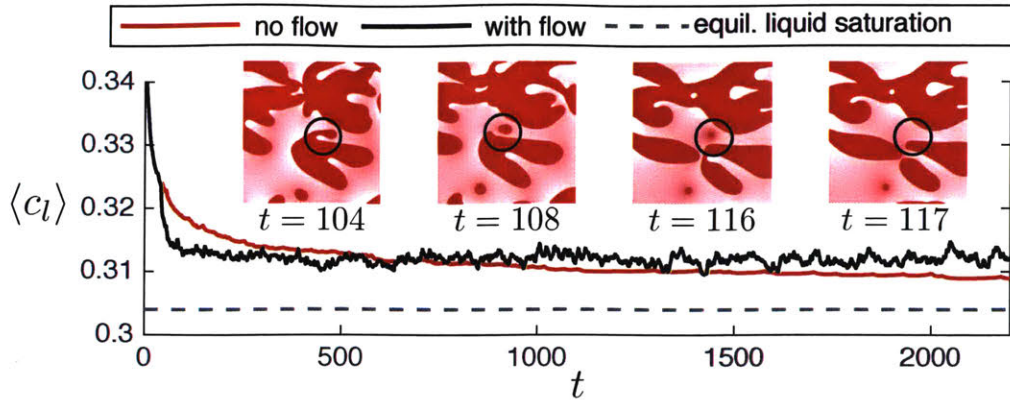


Figure 3-5: Evolution of the averaged liquid-phase concentration $\langle c_l \rangle$ for systems without background flow (red solid line) and with background flow after $t=40$ (black solid line). The gray dashed line indicates equilibrium liquid-phase concentration from the common tangent construction [Fig. 3-1(top)]. Insets: zoomed-in snapshots of c . The circle highlights pinch-off of a small bubble that quickly dissolves into the liquid—the colormap range is $(0.3, 0.35)$ to emphasize concentration variations around the c_l^{eq} .

ble shedding is large compared with the rate of diffusive mass transfer through the liquid, this disparity will result in an excess dissolved concentration. Therefore, the interplay between hydrodynamic instability and thermodynamic coarsening results in a liquid phase that is, on average, always supersaturated. In other words, the emergence of flow disorder from viscous fingering drives the mixture out of compositional equilibrium permanently.

Chapter 4

Viscous fingering with partially miscible fluids

Viscous fingering—the fluid-mechanical instability that takes place when a low-viscosity fluid displaces a high-viscosity fluid—has traditionally been studied under either fully miscible or fully immiscible fluid systems. Here we study the impact of partial miscibility (a common occurrence in practice) on the fingering dynamics. Through a careful design of the thermodynamic free energy of a binary mixture, we develop a phase-field model of fluid-fluid displacements in a Hele-Shaw cell for the general case in which the two fluids have limited (but nonzero) solubility into one another. We show, by means of high-resolution numerical simulations, that partial miscibility exerts a powerful control on the degree of fingering: fluid dissolution hinders fingering while fluid exsolution enhances fingering. We also show that, as a result of the interplay between compositional exchange and the hydrodynamic pattern-forming process, stronger fingering promotes that the system approach thermodynamic equilibrium faster. The results are submitted for publication and currently under review (Fu et al., 2017).

4.1 Introduction

When a less viscous fluid displaces a more viscous fluid, the contrast in viscosity destabilizes the fluid-fluid interface, leading to the formation of viscous fingers (Saffman

and Taylor, 1958b; Homsy, 1987; Chen, 1987). Fluid-fluid miscibility plays an important role in the fingering dynamics, and the fingering pattern can change appreciably based on the miscibility of two fluids. Thus, the subject is traditionally divided into *immiscible* and *miscible* viscous fingering. In both cases, it is viscous forces that drive the hydrodynamic instability. When two fluids are immiscible, surface tension stabilizes short-wavelength perturbations at the interface, allowing some proto-protrusions to spread readily, resulting in less ramified patterns (Paterson, 1981; Chen, 1987, 1989). When the two fluids are fully miscible, the absence of surface tension suggests a more intense fingering pattern, as demonstrated by experiments (Chen, 1987, 1989; Bischofberger et al., 2014; Chui et al., 2015) and simulations (Tan and Homsy, 1988a; Chen and Meiburg, 1998; Riaz and Meiburg, 2003b; Jha et al., 2011, 2013). Nevertheless, without surface tension, complete suppression of the onset of miscible viscous fingering is possible under certain unfavorable viscosity contrast (Lajeunesse et al., 1997; Bischofberger et al., 2014) due to 3D effects. Beyond the onset regime, (Chui et al., 2015) has shown that molecular diffusion along the interface leads to shutdown of instability at late times during radial injections. Further, it has been suggested that Korteweg stresses and other non-equilibrium surface tension effects can act to stabilize miscible displacement (Chen et al., 2001; Chen and Meiburg, 2002; Swernath et al., 2010; Truzzolillo et al., 2013).

Despite the conventional categorization into fully immiscible and fully miscible, the miscibility of two fluids can vary based on local conditions such as pressure and temperature (Henry, 1803). Between the two extremes lie fluid pairs that are *partially miscible*, exhibiting limited, but nonzero, solubility into each other. For such fluid pairs, compositional effects are introduced to two-phase problems where component exchange between phases occurs even in the presence of surface tension. This effect is relevant, for instance, during immiscible gas-in-oil injection for oil recovery where the gas and oil can become partially miscible under high pressure reservoir conditions, leading to swelling of the oil phase and enhanced recovery (Orr, 2007). Under this context, the coupling of viscous fingering with thermodynamic effects could provide new insights to controlling of the viscous instability, which has received increased

attention in recent studies (Li et al., 2009; Chen et al., 2010; Al-Housseiny et al., 2012; Pihler-Puzović et al., 2012; Jha et al., 2013; Nagatsu et al., 2014). Additionally, addressing the role of compositional effects in low Reynolds number two-phase flows is also essential to our understanding of mixing in multiphase mixtures (Ober et al., 2015), biological cell assembly (Brangwynne et al., 2015) and geologic sequestration of CO₂ (Martinez and Hesse, 2016).

Our current understanding of viscous fingering with partially miscible fluids is very limited. In an effort to address this gap, an experimental study on viscous fingering with partially miscible fluids is performed recently (Suzuki et al., 2016). The experiments use a ternary system made of water, PEG and Na₂SO₄ to produce viscously-contrasting fluid pairs that are fully miscible, immiscible or partially miscible. The experiments provide an excellent illustration on how thermodynamic effects can exert a powerful control on hydrodynamic instabilities: as the fluid pairs transition from being immiscible to partially miscible, the authors observe that formation of droplets become more common than formation of fingers. The detailed mechanisms behind the droplets formation remain to be understood. On the modeling front, a recent study (Chen and Yan, 2015) investigated radial injection under different fluid miscibility conditions using a Darcy-Cahn-Hilliard model, where the fluid miscibility is prescribed through the design of a Cahn-Hilliard type free energy (Cahn and Hilliard, 1958). Though the model is limited in its ability to explore the truly partially miscible regime, where one would expect to see effects such as finger swelling due to supersaturation, the study provides a consistent comparison between immiscible and miscible viscous fingering to demonstrate the role of compositional effects in controlling the vigor of the instability. As presented in earlier work (Chui et al., 2015; Chen et al., 2001), the study confirms that the degree of fingering instability, as measured by interface length, peaks at a transition time followed by a decay due to diffusive mixing at the interface for *miscible* systems; in *immiscible* simulations, however, where surface tension is present and component diffusion is negligible, a decay in interfacial length is not observed (Chen and Yan, 2015).

In this work, we study the interplay between hydrodynamics and nonequilibrium

compositional effects in partially miscible systems. To develop new insights into the physics of a nonlinear hydrodynamic instability out of thermodynamic equilibrium, here we develop a 2D gap-averaged model, in the spirit of a large body of literature on Hele-Shaw flows for both miscible and immiscible fluids (Tryggvason and Aref, 1983; Meiburg and Homsy, 1988; Tan and Homsy, 1988a; Linder et al., 2002; Nguyen et al., 2010; Li et al., 2009; Al-Housseiny et al., 2012; Pihler-Puzović et al., 2012; Jha et al., 2011, 2013; Cueto-Felgueroso and Juanes, 2012a, 2014). While a full 3D flow model might be desirable to eventually provide a more detailed description of the flow (as is the case for fully miscible (Petitjeans and Maxworthy, 1996; Chen and Meiburg, 1996; Lajeunesse et al., 1997; Yang and Yortsos, 1997; Aubertin et al., 2009; Bischofberger et al., 2014; Oliveira and Meiburg, 2011, 2017) and fully immiscible systems (Aussillous and Quéré, 2000; Cueto-Felgueroso and Juanes, 2012a, 2014; Levaché and Bartolo, 2014; Zhao et al., 2016)), it should build on the insights of the nonlinear analysis in 2D. We adopt a phase-field modeling approach, which has been successful at describing immiscible two-phase flow in Hele-Shaw geometry (Anderson et al., 1998a; Folch et al., 1999a,b; Hernández-Machado et al., 2003; Lee et al., 2002a,b; Sun and Beckermann, 2008; Cueto-Felgueroso and Juanes, 2012a, 2014) and in porous media (Cueto-Felgueroso and Juanes, 2008) and, more recently, the coarsening dynamics of partially miscible binary mixtures under viscous fingering (Fu et al., 2016). Under the phase-field framework, the design of thermodynamic free energy allows us to readily incorporate partial miscibility into multiphase flow. In its minimal description, the free energy of a two-phase two-component mixture follows the Cahn-Hilliard form (Cahn and Hilliard, 1958), formulated as a functional of component concentration and its gradients. Under the Cahn-Hilliard framework, fluid phase is inferred from component concentration, and not independently described. This approach is successful in capturing the dynamics of binary mixtures with fast phase-transition time scale (e.g. immiscible fluids) (Ruiz and Nelson, 1981; Wagner and Yeomans, 1998; Shou and Chakrabarti, 2000; Berthier et al., 2001; Berti et al., 2005; Perlekar et al., 2014; Chen and Yan, 2015). In contrast, our proposed model (Fu et al., 2016) allows fluid concentrations to evolve independently from the phase variable, in order

to capture the essence of *partially miscible* systems, where components can exchange between the two phases at time scales comparable to that of flow. During injection, the evolution of the invading phase variable (e.g. volume fraction of the invading phase) is driven by viscous instability, accompanied by redistribution of composition between phases and phase transformations that are driven by chemical potentials. Capturing the duality of the dynamics requires having separate evolution equations for phase and concentration, and defining a free energy that is a function of both variables. Similar two-field formulations have been extensively adopted for the simulation of binary alloys solidification Boettinger et al. (2002), but, thus far, not for interfacial flows with compositional effects. With this more general framework, we are able to investigate the two-way coupling between hydrodynamics (viscous fingering) and thermodynamics (compositional exchange between phases and phase transformation). We apply our model to the viscous fingering problem in a rectangular Hele-Shaw cell, where initially a gas band is surrounded by a liquid (Fig. 4-1, left). Gas fingers are then created by pushing the gas band leftwards with an imposed constant flux of the liquid phase of the same initial composition (Fig. 4-1, right).

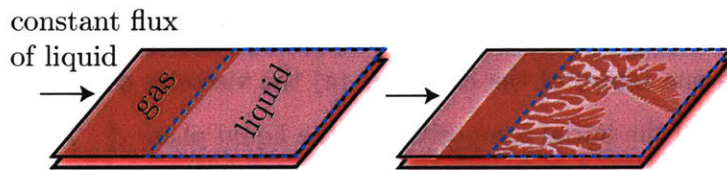


Figure 4-1: Displacement of a gas band through liquid phase in a Hele-Shaw cell: (a) initial set up (b) the displacement leads to viscous fingering due to viscosity contrast. Meanwhile, compositional exchange occurs along the fingering interface if the two fluids are out of thermodynamic equilibrium. For example, in this sample image, the liquid phase is initially supersaturated with respect to gas and will swell the gas fingers as they evolve (see Sec. 5.1.1). The blue dashed box indicates the area of study in our discussions.

4.2 Problem setup and numerical methods

We conduct high-resolution numerical simulations of our model (described in previous Chapter) for the problem described in Fig. 4-1, in which we displace a band of less

viscous gas through the more viscous ambient liquid under a constant flux of liquid of the same initial composition. Our simulations are on a domain of size 200×80 ($L_x \times L_y$) and parameter values $\text{Ch}=1/2000$, $\text{Ma}=1/200$ and $\epsilon=200$ (and parameters of the Wilson model given in Fig. ??). We perform a straightforward calculation of Ca and Pe in order to mimic an experimental fluid pairs analogous to water and methane gas (weakly soluble in water). We approximate the typical injection rate in a rectilinear geometry to be $U = 1.9 \times 10^{-3} \text{cm/s}$, based on the values reported in (Levaché and Bartolo, 2014). The surface tension is take as that of water and air at room temperature: $\epsilon_0^2 T/b = 72 \text{ dyn/cm}$. The diffusion coefficient of gas in water at 25°C is taken from (Witherspoon and Saraf, 1965) as $D = 2 \times 10^{-5} \text{ cm}^2/\text{s}$. The molar density of pure water is about 0.056 mol/cm^3 , and that of gas is about 0.00005 mol/cm^3 . Here we take an intermediate value of 0.01 mol/cm^3 for ν . Based on these values, we calculate that $\lambda_c^\phi = 1.29 \times 10^{-5} \text{cm}^3/(J \cdot \text{s})$ and $\lambda_c = 8.1 \times 10^{-7} \text{cm}^5/(J \cdot \text{s})$. The key dimensionless parameters in our system are computed as: $\text{Ca} = U/(\lambda_c^\phi \gamma) \approx 2$ and $\text{Pe} = U/\lambda_c \gamma \approx 32$.

We are interested in exploring the coupling between hydrodynamic instabilities and thermodynamic effects. Consequentially, we focus on two parameters, each of which controls one aspect of the coupling: (a) the viscosity contrast R between the two fluids and (b) the initial composition of the liquid phase c_l^0 . The parameter R is chosen here to be $R = 0, 1, 2, 3, 4$ and 5 , where the gas phase is always less (or equally) viscous than the liquid. The value of c_l^0 determines the thermodynamic response of the two fluids when interacting, where three scenarios may occur: (i) the gas dissolves, transferring CO_2 into the liquid; (ii) the gas and liquid are at equilibrium, no component exchange occurs; or (iii) the gas expands in volume by exsolving CO_2 from the liquid. As shown in Fig. ??, the common tangent construction of the bulk free energies yields the equilibrium composition of the two fluids as: $c_g^{\text{eq}} \approx 0.89$, $c_l^{\text{eq}} \approx 0.33$. Instructed by this calculation, we can re-create the three scenarios by setting the defending liquid to be initially (at $t = 0$):

(a) *undersaturated* with respect to the gas phase: $c_l^0 = 0.05 < c_l^{\text{eq}}$;

(b) *near-saturated* with respect to the gas phase: $c_l^0 = 0.33 \approx c_l^{\text{eq}}$;

(c) *supersaturated* with respect to the gas phase: $c_l^0 = 0.5 > c_l^{\text{eq}}$.

In all the simulations performed, we only vary R and c_l^0 while all other parameters are unchanged. We initialize the gas phase with a composition that is close to equilibrium values: $c_g^0 = 0.89 \approx c_g^{\text{eq}}$. Further, all simulations start with the same initial configuration in ϕ (as shown in Fig. 4-1 left):

$$\phi_0 = \begin{cases} 1, & \text{if } 0.05L_x \leq x \leq 0.4L_x \\ 0, & \text{otherwise} \end{cases} \quad (4.1)$$

The initial concentration field c_0 is computed as an affine mapping from ϕ_0 :

$$c_0 = (c_l^0 - c_g^0)(1 - \phi_0) + c_g^0. \quad (4.2)$$

We solve Eqs. (3.12)–(3.14) sequentially. We first obtain the pressure and velocity using a finite volume method with a two-point flux approximation. Next we update c and ϕ using a Fourier pseudo-spectral discretization and using a biharmonic-modified time stepping (Bertozzi et al., 2011). The domain is discretized with 2560×1024 ($N_x \times N_y$) points. The boundary conditions are periodic, but we show results only in a window of the simulation domain ($80 \leq L_x \leq 200$, indicated as the blue dashed box in Fig. 4-1) unaffected by the boundaries during the simulation period reported (that is, until the fingers reach the right boundary).

4.3 Results

4.3.1 Fingering pattern under the influence of gas dissolution and exolution

We present a summary of the final displacement pattern (in c) in a c_l^0 – R phase diagram in Fig. 4-2. The middle row of the phase diagram corresponds to a dis-

placement scenario where the two fluids are near-saturated, analogous to immiscible displacement (Maxworthy, 1986; Paterson, 1981). In this regime, viscosity ratio is understood as the control parameter for large scale structure of the pattern (Homsy, 1987; Maher, 1985). With this series of simulations, we recover the classic features of immiscible viscous fingering: shielding, spreading and tip-splitting (Homsy, 1987), as well as side-branching, merging, pinchoff of fingers, and entrapment of the defending phase towards the injection side (Park and Homsy, 1985; Arnéodo et al., 1989). The rest of the phase diagram (top and bottom rows) illustrates the effects of gas dissolution/exsolution on the displacement patterns.

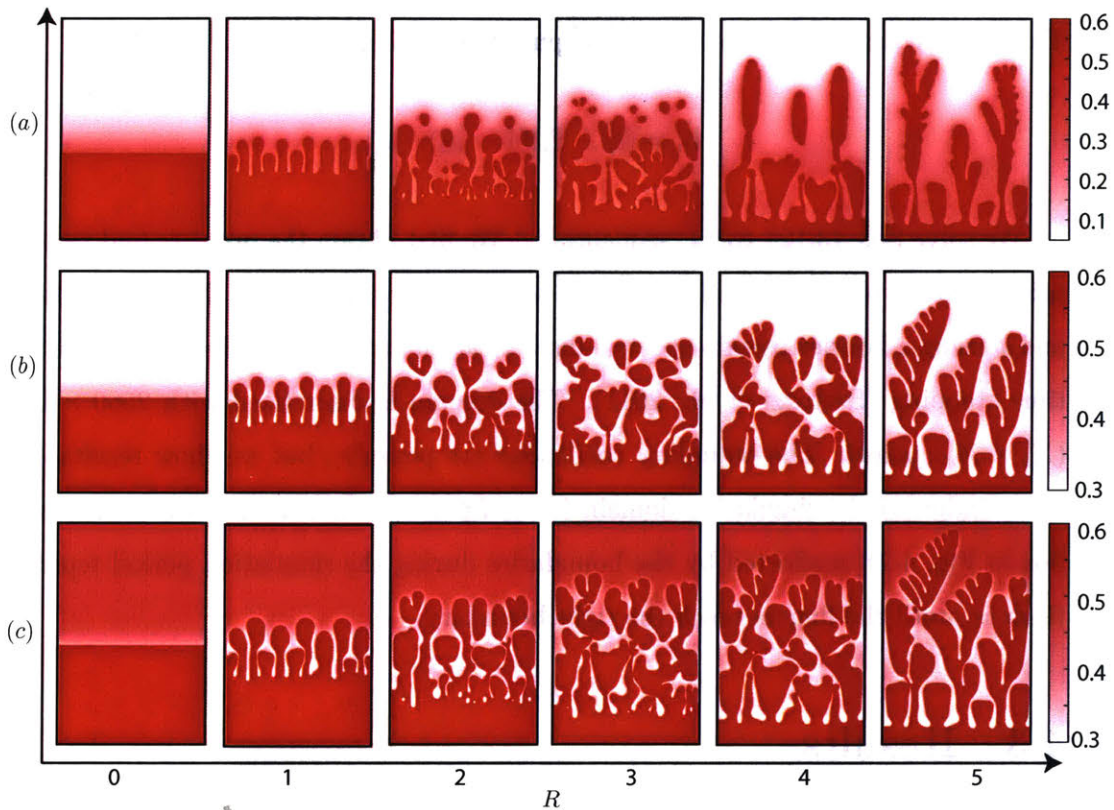


Figure 4-2: The coupling between different viscosity contrast and compositional effects lead to a rich set of viscous fingering patterns. Here we show snapshots of c at $t = 50$ for six different R values (across each row). Each of the three rows correspond to different c_i^0 values: defending liquid is (a) undersaturated; (b) near-saturated and (c) oversaturated. Note that the colormap differs between each row to reveal the detailed structures in the concentration field.

The rest of the phase diagram (top and bottom rows) illustrates the effects of phase transformations on the displacement patterns. In the top row, the defending liquid is undersaturated with respect to the gas. Upon contact, the gas volume dissolves locally to replenish the CO_2 concentration level in the ambient liquid. This dissolution process hinders the growth of young fingers, or proto-protrusions, that form along the sides of dominant fingers. By immediately stripping away any gas accumulation that fuels the growth of instability, the dissolution process inhibits proto-protrusions developing into mature fingers. This effect is most active towards the front of the invasion, where the gas phase is persistently met with undersaturated liquid. Under this effect, the un-bifurcated fingers appear slimmer ($R = 1$), and we observe disconnected droplets that become rounded due to dissolution for intermediate viscosity contrast ($R = 2, 3$); for larger viscosity contrast ($R = 4, 5$), we observe “bald” dominant fingers that lack active side branches.

An important distinction between partially and fully miscible fluids pair is the direction of component diffusion. In a fully miscible system, molecular diffusion of the components follow the direction of positive concentration gradient. In the case of partially miscible fluids, however, component diffusion is directed in the direction of chemical potential gradient, which can sometimes be the reverse of the concentration gradient. Such is the case when the gas phase is exposed to an oversaturated liquid (bottom row of the phase diagram), where the invading fingers swell by exsolving the excess CO_2 from the liquid, against the direction of concentration gradient. Exsolution into the gas phase increases the volume of gas (ϕ) and thus promotes instability in the system as it expands the radius of invading front for tip-splitting (Paterson, 1981). This results in an enhanced shielding and merging effect and more prominent side branches. Such promotion of instability is observed across all values of R where fingering occurs, and the effect is most apparent for $R = 4, 5$. In addition, the fingers also appear larger overall in comparison to the middle row.

4.3.2 The coupling between ϕ and c

We illustrate the fingering pattern using the c -field in Fig. 4-2; however, it is important to note that both ϕ and c are independently solved using separate evolution equations in our model. To demonstrate this, Fig. 4-3 shows snapshots of 1D cross section profiles of both ϕ and c side-by-side for $R = 5$ with *undersaturated* (left) and *oversaturated* (right) defending fluid. From this we observe that both ϕ and c , although independently solved, follow each other closely. The pattern in c emulates that of ϕ , although c provides more details on component distribution within each phase. There are, however, fundamental differences in how these two variables behave under their own evolution equation. The 1D profile of ϕ (Fig. 4-3 bottom, dashed blue line) is continuous but compact—a feature of immiscible invasion under diffuse-interface descriptions. Meanwhile the 1D profile of c (Fig. 4-3 bottom, solid red line) exhibits a diffuse profile that is inherent to diffusive component transport. The coupling between ϕ and c is not merely a modeling construct: rather, it provides compositional details of the two-phase system that either variable alone would not be able to reveal. This is further discussed in Sec.4.3.5.

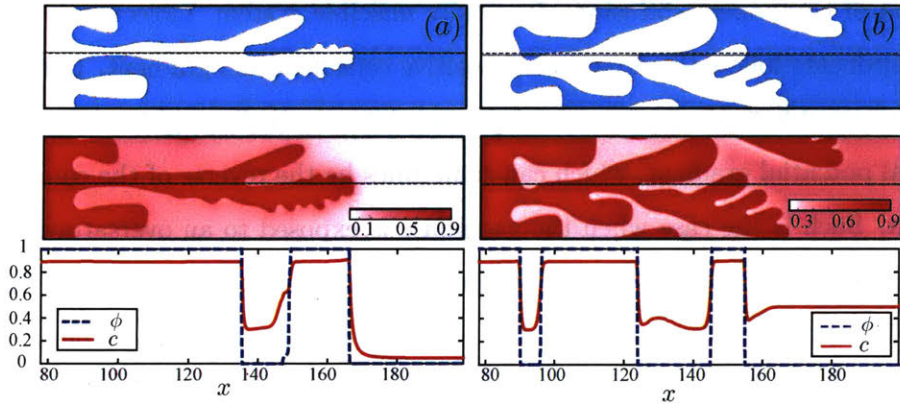


Figure 4-3: Defending fluid is (a) undersaturated or (b) supersaturated. Top: snapshots of ϕ at $t = 46$. Middle: snapshots of c at $t = 46$. Bottom: horizontal transects of ϕ (dashed) and c (solid) at $t = 46$ along the dashed lines indicated in the 2D plots in the top and middle rows. Note that regions where $c \approx 0.33$ indicate area in which local thermodynamic equilibrium is in place.

4.3.3 Thermodynamic control on the degree of fingering

Thermodynamic effects such as chemical reactions can lead to a myriad of interesting behaviors when coupled with hydrodynamic instabilities (Daccord and Lenormand, 1987; De Wit, 2001; Szymczak and Ladd, 2011b; Nagatsu et al., 2014; Haudin et al., 2014). In this work, we explore such coupling in the form of thermodynamics-driven phase transformation that leads to finger dissolution and exolution during viscous fingering. The coupling can be of particular interest in the context of controlling of the viscous instability, which has received increased attention in recent studies (Li et al., 2009; Chen et al., 2010; Al-Housseiny et al., 2012; Pihler-Puzović et al., 2012; Jha et al., 2013; Nagatsu et al., 2014). Proposed mechanisms include use of chemical reactions (Nagatsu et al., 2014), alternating injections (Jha et al., 2013), control of injection rate (Li et al., 2009; Dias et al., 2012), imposing a gradient in flow pathway (Zhao et al., 1992; Al-Housseiny et al., 2012), or confining the flow by elastic membranes (Pihler-Puzović et al., 2012).

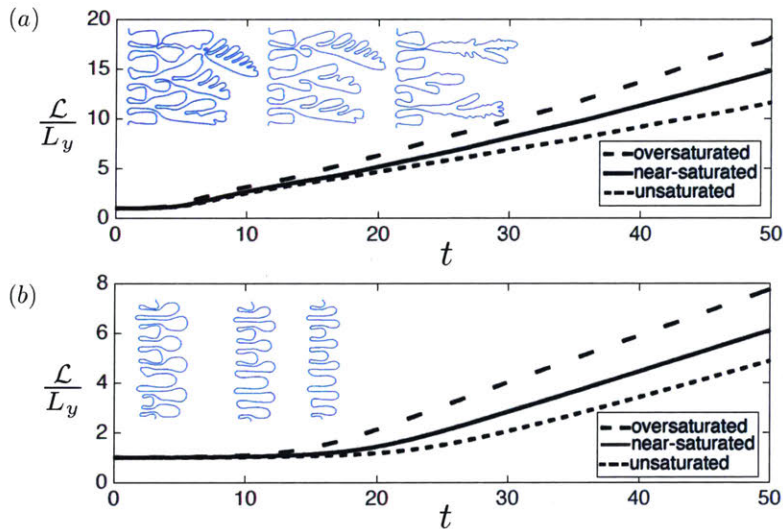


Figure 4-4: Normalized interfacial length, \mathcal{L}/L_y , as a function of time for three compositional scenarios with (a) $R = 5$ and (b) $R = 1$. In both plots, colored insets show the traced outline of the fingering front at $t = 50$ for oversaturated, near-saturated and unsaturated defending liquid (left to right).

In Section 5.1.1, we demonstrate qualitatively that thermodynamic-driven phase

transformations, resulting in fluid dissolution or exsolution, can hinder or enhance viscous fingering instabilities beyond onset regime. Here we quantify such effect by inferring the degree of fingering with direct measurement of the total interfacial length generated by the instability, using image segmentation (see examples in Fig. 4-4 insets). The interfacial length of the fingering front, \mathcal{L} , is scaled by the transversal domain length, $L_y = 80$, so that initially $\mathcal{L}/L_y = 1$ and will increase as fingers form and grow (Fig. 4-4). When $R = 0$, $\mathcal{L}/L_y = 1$ for the entirety of the simulation. In Fig. 4-4, we show the evolution of \mathcal{L}/L_y under $R = 1$ (bottom) and $R = 5$ (top) for all three compositional scenarios. The degree of fingering persistently increases under all scenarios; the instability is not suppressed due to gas dissolution. However, compared to the second scenario (the immiscible analog, solid lines), the interfacial growth is slowed down under gas dissolution (short dashed line), indicating weakening of the instability; on the other hand, the growth is significant enhanced under finger swelling (long dashed line), indicating promotion of the instability.

4.3.4 Impact of viscous fingering on the rate of gas dissolution/exolution

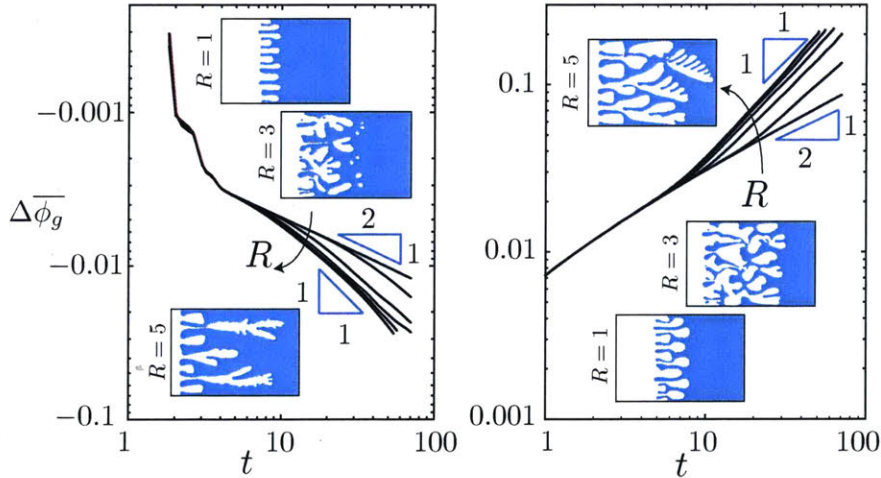


Figure 4-5: $\Delta\bar{\phi}_g(t)$ for $R = 0, 1, 2, 3, 4, 5$ (arrows indicating increasing order) when the defending phase is undersaturated (left) and supersaturated (right). The insets in both plots show snapshots of ϕ at $t = 50$ for the different values of R .

The total gas volume fraction in the system should decrease or increase due to gas dissolution or exolution, respectively. In other words, the amount of gas volume change in the domain is a global measure that reflects how much the system has progressed towards thermodynamic equilibrium.

Locally, the reduction or increase in gas volume is a direct consequence of component exchange across the phase-phase boundary. We expect that hydrodynamic instability will play an important role in this process because phase transformations take place at the invasion front where the two fluids are out-of-equilibrium, and viscous fingering deforms and lengthens such front.

Here, we define the change in gas volume fraction across the whole domain over time as:

$$\Delta\overline{\phi}_g(t) = \frac{\iint \phi(t)dxdy - \iint \phi_0dxdy}{\iint \phi_0dxdy}. \quad (4.3)$$

In Fig. 4-5, we show $\Delta\overline{\phi}_g(t)$ for different values of R when the defending fluid is undersaturated (left) and supersaturated (right). When no viscosity contrast is present ($R = 0$), the invasion front remains stable and phase transformation is limited by the rate at which CO_2 diffuses in the liquid phase in order to be transported away or towards the gas phase. This explains $|\Delta\overline{\phi}_g| \sim t^{1/2}$ for $R = 0$ in both composition scenarios. In the presence of the hydrodynamic instability ($R > 0$), the invasion-front deformation provides more interfacial area over which the two fluids can equilibrate. This mass-transfer enhancement is clearly shown in the scaling $|\Delta\overline{\phi}_g| \sim t^1$, observed for $R = 2, 3, 4, 5$.

4.3.5 Heterogeneity in phase compositions

While gas volume fraction is a measure of how the system progresses towards its thermodynamic equilibrium globally, here we show that progress towards equilibrium can be very heterogeneous within the domain. To do this, we track the liquid phase concentration, computed pointwise as:

$$c_l(x, y) = (1 - \phi(x, y))c(x, y). \quad (4.4)$$

We introduce $\bar{c}_{ly}(x)$ as the y -averaged liquid phase concentration along the x -axis. If a thermodynamic equilibrium is reached locally, $\bar{c}_{ly} \approx c_l^{\text{eq}}$ at that point; otherwise, \bar{c}_{ly} should be larger or smaller than c_l^{eq} . In Fig. 4-6 (left column), we plot $\bar{c}_{ly}(x)$ at six different times with $R = 5$ for undersaturated [Fig. 4-6(a)] and supersaturated [Fig. 4-6(b)] defending liquid. The shaded red region indicates *metastability*, where the system is close to thermodynamic equilibrium (red dashed lines Fig. 4-6). From this, we observe that the system reaches metastability towards the roots of the fingers, where two fluids have more time to equilibrate. Towards the fingering front, the fluid-fluid interface is newly created, leaving little time for component exchange to occur; therefore, the liquid composition appears to be far away from thermodynamic equilibrium at the fingering front. The spatial heterogeneity in the phase compositions and consequently in the thermodynamic equilibrium state between the fluids has implications on the pattern forming process: towards the roots of the fingers, where the system has established a thermodynamic equilibrium earlier, the fingering morphology is no longer subject to dissolution/exolution effects; towards the invasion front, freshly created fingers are subject to constant shrinkage/expansion due to gas dissolution/exolution.

4.4 Conclusions

In this Chapter, we study viscous fingering with partially miscible fluids. We introduce a new phase-field model to describe two-phase two-component flow and transport in a Hele-Shaw cell. We present high-resolution numerical simulations of the model applied to the viscous fingering problem for various viscosity contrasts and different initial fluid compositions. From the perspective of pattern formation, our results demonstrate that fluid dissolution or exsolution due to partial miscibility can hinder or enhance viscous fingering, respectively. This is shown by both directly visualizing the fingering pattern (Sec. 5.1.1), and also by quantifying the degree of fingering through the measure of interfacial length (Sec. 4.3.3).

Conversely, we also explore how the pattern forming process can impact the rate

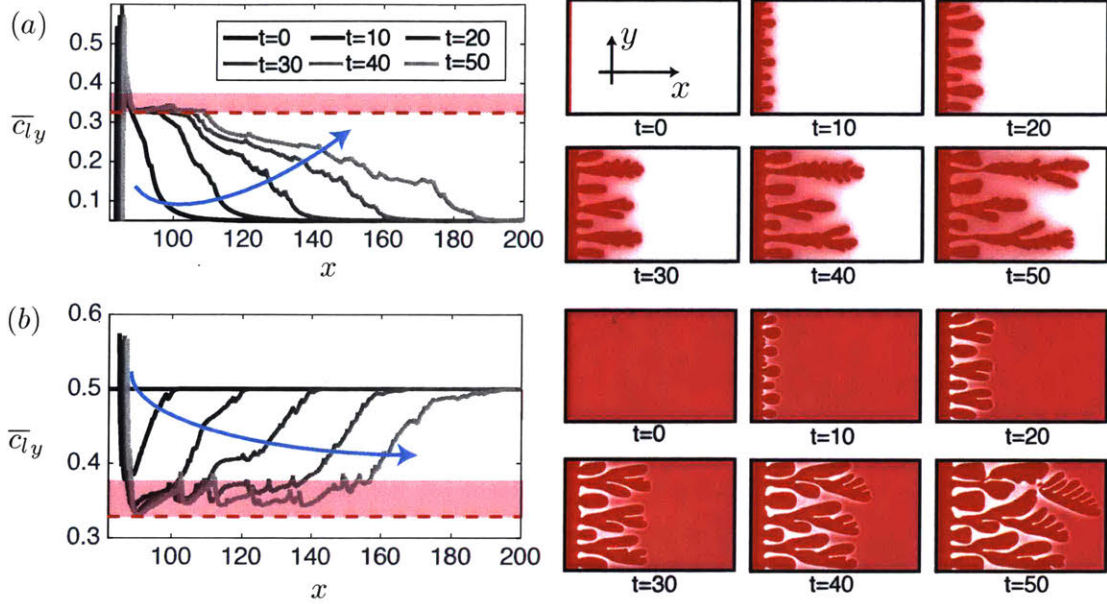


Figure 4-6: (Left) $\bar{c}_{ly}(x)$ at $t = 0, 10, 20, 30, 40$ and 50 . Blue arrow indicates direction of time. Red dashed line indicates thermodynamic equilibrium: $c_i^{\text{eq}} \approx 0.33$. Red shaded area indicates metastability. (Right) snapshots of c for the corresponding times. The defending liquid is initially undersaturated in (a) and supersaturated in (b), and all simulations correspond to $R = 5$.

at which the two fluids reach compositional equilibrium. By measuring globally the amount of gas dissolution/expansion from component mass transfer, we show that the increase in degree of fingering – and associated increase in interfacial length – is directly linked to a faster rate of thermodynamic equilibration (Sec. 4.3.4). By measuring locally the degree of equilibrium, we show that equilibrium is reached earlier towards the roots of the fingers, where the two fluids have more time to exchange components (Sec. 4.3.5). The spatial heterogeneity in the degree of thermodynamic equilibrium implies that the gas fingers are subjected to different levels of dissolution/expansion effects throughout the domain. As a result, the final fingering pattern we observe is a result of the complex nonlinear coupling between hydrodynamic instabilities and thermodynamic effects.

An important assumption we make in this Chapter is that the thermodynamic-driven component exchange does not change the density or viscosity of either fluid,

or the interfacial tension between the two phases. This assumption allows us to simplify the parameter space for our simulations and thus focus on the effect of viscosity contrast and initial fluid compositions. However, these assumptions may no longer be valid for realistic fluid pairs where density, viscosity and interfacial tension can change appreciably due to mass transfer across phases. The effect of component exchange on fluid properties could yield interesting displacement dynamics. For instance, while we only explore the displacement dynamics under a viscously unstable configuration ($R > 0$) in this work, unstable displacement could still arise under an initially viscously stable configuration ($R < 0$). Under constant fluid-fluid component exchange, this instability could be caused by, for example, nonuniform changes in local surface tension at the fluid interface (a Marangoni effect) or changes in local fluid viscosity that eventually reverse the viscosity contrast. It would be interesting to incorporate these effects in our current model in the future to fully understand ongoing experimental studies (Suzuki et al., 2016)

Chapter 5

Phase-field modeling of gas-liquid-hydrate systems

5.1 Introduction

Methane (CH_4) is a valuable source of energy but also a potent greenhouse gas. It is estimated to be responsible for about 20% of global warming induced by greenhouse gases (Kirschke et al., 2013). Assessing the global methane budget remains a challenge to date due to uncertainties in contributions from already identified sources and sinks of methane (Ruppel and Kessler, 2017).

Gas hydrates are water-based crystalline solids encapsulating gas molecules such as CH_4 ; they contain a large portion of the global mobile carbon and are often found in low temperature and high pressure environments such as arctic permafrost and deep marine sediments. Depressurization or warming could lead to dissociation of hydrates and emissions of methane into the ocean water column and potentially the atmosphere (Ferré et al., 2012; Ruppel and Kessler, 2017). This mechanism potentially explains widespread methane leakage from the seafloor of the West Spitsbergen margin (Westbrook et al., 2009), the Makran continental margin (Römer et al., 2012) and northern US Atlantic margin (Skarke et al., 2014). Large blowout events from generic marine environments (Leifer et al., 2006) or continuous seepage at shallow water depth less than 100m (McGinnis et al., 2006) could also provide a direct path

for injection of methane into the atmosphere. Regardless of the source of leakage, escaped methane in water can have an immediate impact on marine environment as well as the atmosphere.

The mechanism that triggers the onset of hydrate dissociation in marine sediments has been a subject of extensive studies (Mienert et al., 2005; Reagan and Moridis, 2008; Biastoch et al., 2011; Phrampus and Hornbach, 2012; Ferré et al., 2012); the consensus is that ocean warming at regional or global scale is the primary cause of hydrate dissociation and methane release observed around the world. On the other hand, the fate of leaked methane bubbles after entering the water column remains to be better understood. Released methane can quickly dissolve into the undersaturated water column and produce CO₂ as it is oxidized, leading to acidification and de-oxygenation of ocean waters (Mau et al., 2007). A series of work by McGinnis, Greinert and their collaborators (McGinnis et al., 2006; Greinert and McGinnis, 2009; Greinert et al., 2010) have quantified methane fluxes from ocean seeps in Black Sea shelf using a combination of field data and a parameterized model for bubble rising in ocean, considering the water column as a chemical sink during the rising process. More recent studies have also quantified methane fluxes from seafloor seeps at the Hudson Canyon (Weinstein et al., 2016) and Gulf of Mexico (Wang et al., 2016). Because the large amount of water volume serves as an effective chemical buffer, these studies conclude that most methane emitted from seafloor becomes dissolved relatively deep in the water column and does not reach the atmosphere (Ruppel and Kessler, 2017). Nevertheless, when venting sites are within the gas hydrate stability zone (GHSZ), rigid hydrate shells could form on the gas-liquid interface of the bubbles, which have been observed in field surveys (Topham, 1984; Sauter et al., 2006; Graves et al., 2015; Wang et al., 2016), field experiments (Rehder et al., 2002, 2009) and controlled laboratory experiments (Maini and Bishnoi, 1981; Chen et al., 2014, 2016; Warzinski et al., 2014). Evidence of high methane concentrations at shallow water depths over identified methane plume source deep in the ocean (Sauter et al., 2006; Westbrook et al., 2009) suggests that hydrate-coating on bubbles could play an important role in protecting methane against the ocean buffer in certain scenarios.

The hydrate coating is hypothesized to prevent rapid dissolution of methane into the water column (Rehder et al., 2002; Zhang, 2003), which could increase the lifetime of rising methane bubbles and allow more methane to reach the upper water column, changing the vertical distribution of dissolved methane (Sauter et al., 2006). However, validation of this hypothesis is currently inconclusive based on existing field data and numerical modeling studies, which suggest that the hydrate coating may or may not reduce the rate at which methane leaves rising gas bubbles (Rehder et al., 2002; Wang et al., 2016). To rigorously test out this hypothesis, we need robust physics based modeling in combination with controlled laboratory studies to understand the physics of bubble rise, the time scale of rising compared to hydrate shell formation, and the role that hydrate coating plays in transporting methane to shallow layers of the ocean. The end result should improve our assessment on how bubble rising process alter ocean biogeochemistry and contributes to atmospheric methane level.

The formation of hydrate shell on hydrocarbon droplets/bubbles in a water-rich environment is also extensively studied in flow assurance community (Aman and Koh, 2016). During transport of hydrocarbon-water mixtures in offshore pipelines, a hydrate shell can readily form on the hydrocarbon-water interface, which allows hydrate-coated droplets to agglomerate and form larger hydrate aggregates that eventually result in blockage of pipelines. A series of controlled laboratory experiments are performed to study the dynamics and morphology of shell formation on a static/suspended gas bubble (Sun et al., 2007; Peng et al., 2007; Li et al., 2014) and on a free-flowing bubble (Maini and Bishnoi, 1981; Chen et al., 2014, 2016; Warzinski et al., 2014). These experiments have elucidated fascinating morphological behaviors of the hydrate shell once it forms on a gas bubble. The most prominent observation is the buckling of fully formed hydrate shells (Sun et al., 2007; Peng et al., 2007; Li et al., 2014; Chen et al., 2014, 2016), potentially caused by an inward pressure difference generated due to gas consumption inside the bubble during hydrate formation at the gas-liquid interface. In some cases, partially formed hydrate “plates” are observed to float on the gas-liquid interface, whose movements are likely controlled by fluid flow at the bubble boundary layer and thus accumulates towards the bottom half of the

bubble (Warzinski et al., 2014). Additionally, shedding of hydrate flakes (Maini and Bishnoi, 1981; Warzinski et al., 2014), crack formation within a fully formed shell as well as wrinkling of thin hydrate film are observed (Chen et al., 2014, 2016; Warzinski et al., 2014). Understanding the morphology and mechanical stability/instability of hydrate crust in the context of a rising bubble allows us to better predict (1) the impact of hydrate coating on the rise velocity of a gas bubble and (2) the survival height of a hydrate-coated bubble before it crumbles into hydrate flakes during its ascend (Wang et al., 2016). Both issues are critical in refining our current predictions of the fate of methane bubbles escaping from the widely-observed seep sites.

On the other hand, physics and thermodynamics based modeling of interfacial hydrate formation in multiphase flow remains a challenging task (Sum et al., 2012). One approach is to develop an upscaled, parameterized model that can describe bulk behaviors of the multiphase system, without having to fully resolve, both temporally and spatially, the details of hydrate formation at a single bubble scale. For instance, CSMHyK-OLGA from Colorado School of Mines is developed on the basis of thermodynamic principles and multiphase flow physics, and parameterized with experimental observations in laboratory and flow loop studies (Sum et al., 2012). The model is used to provide upscaled prediction on when and where hydrate blockage may occur in a pipeline; however, the model is not designed to resolve the detailed multiphase hydrodynamics and thermodynamic kinetics relevant for a single hydrate-crust bubble. Similarly, to estimate the “shielding” effect of hydrate shell on the fate of natural gas bubble plumes, Wang et al. (2016) improved upon the 1D bubble plume model proposed by Clift et al. (1978) by assuming that a hydrate-crust bubble behaves as a “dirty bubble”, where the transfer coefficient at the gas-water interface is smaller than that of a clean bubble. The approach is successful in explaining some field measurements, however, the Clift bubble model does not consider the thermodynamics of hydrate formation/dissociation during the bubble ascend and thus is not able to fully explain the survival height of hydrate-crust plumes in the context of hydrate stability.

The aim of this Chapter is to develop a novel phase-field modeling framework

that is thermodynamically consistent with the methane hydrate system and able to describe the coupled hydrate-forming kinetics with multiphase hydrodynamics of a gas bubble in water. We perform numerical simulation of the new model to examine the role of hydrate armoring in slowing down methane diffusion during bubble ascent. Specifically, we seek to provide mechanistic understanding of the “shielding” effects and the morphological instability of hydrate crust by addressing the following questions:

1. What processes control hydrate formation on a gas-liquid interface?
2. What are the rate-limiting factors in hydrate formation on a gas-liquid interface?
3. How do these identified processes lead to slow-down of gas dissolution?
4. Which phase supplies the methane when hydrate forms on a gas-liquid interface?
5. Under what conditions does a hydrate-crust bubble become crumbled?

5.1.1 Predicting gas hydrate stability using thermodynamic phase diagrams

A thermodynamic phase diagram is a predictive tool used to determine the occurrence and stability of hydrate in natural environment such as marine sediments, permafrost or ocean water column, and in industrial systems such as offshore pipelines (Sloan et al., 2010). Based on input environmental parameters such as pressure, temperature or hydrocarbon concentrations, a phase diagram illustrates the *equilibrium* phase behavior of a given hydrocarbon-water system. Common phase diagrams used in hydrate research are the pressure-temperature (P - T) and temperature-composition (T - χ) phase diagrams. A phase diagram is usually calculated based on thermodynamic principle of Gibbs free energy minimization, where the equilibrium state corresponds to the state of minimum Gibbs free energy of the multiphase system. The approach requires a fundamental description of the free energy of all possible phases in the system based on classical and statistical thermodynamics. These descriptions also arrive

with a suite of parameters, some of which can be measured and some are numerically optimized in order to fit model predictions with known phase behavior from experimental measurements (Ballard and Sloan, 2002; Jager et al., 2003; Ballard, A. L. and Sloan, 2004; Ballard and Sloan, 2004). In the following, we discuss two types of phase diagrams that are important in predicting stability and occurrence of gas hydrate in natural and industrial environment. In these phase diagrams and for the rest of the Chapter, we make reference to three distinct phases: the liquid phase (L_w), which is the aqueous solution of methane dissolved in water; the gas phase (V), which consists of mainly methane and some amount of water vapor; and the hydrate phase (H). The system of interest is made of two components: water and methane.

The P - T phase diagram

A most commonly used phase diagram is drawn in the the pressure-temperature domain (Figure 4.1 in (Sloan and Koh, 2008)), where the three-phase line (L_w -H-V coexistence) divides the domain into a hydrate stable region (H- L_w coexistence) and a hydrate unstable region (L_w -V coexistence). In marine settings, one can combine the information on water temperature (hydrothermal gradient), sediment temperature (geothermal gradient) and the hydrostatic pressure (P) with the P - T phase diagram to determine the Gas Hydrate Stability Zone (GHSZ)— a depth range overlying part of the sediment and part of the water column where hydrate can be stable (Kvenvolden and Lorenson, 2001; Xu and Ruppel, 1999; Ruppel, 2007).

The T - χ phase diagram

An important limitation of the P - T phase diagram in predicting hydrate stability is that it does not consider the effect of methane saturation in water. Indeed, even with the appropriate pressure and temperature, hydrate may not form if the local saturation of methane is too small. The constraint that methane saturation imposes on hydrate formation has motivated geophysicists to refine the calculation of GHSZ using information of methane solubility in water (Zatsepina and Buffett, 1998; Xu and Ruppel, 1999; Tréhu et al., 2004, 2006). As a result, a narrower region within

the GHSZ is identified as the Gas Hydrate Occurrence Zone (GHOZ), where methane solubility is high enough to enable hydrate formations.

In addition to field-scale implications, methane saturation also exerts powerful local influence on the microstructure (fraction of cage occupancy) of hydrate during its formation. In the seminal work presented in (Huo et al., 2003), raman spectroscopy experiments show that type I methane hydrates formed at the vapor-liquid interface have a different composition from dendritic hydrates grown into the liquid phase (Fig. 5-1). The former *interfacial* hydrate has a slightly larger molar fraction of methane (≈ 0.146) compared to that of the *dendritic* hydrate formed into the liquid phase (≈ 0.139). The experimental observation and measurements are further corroborated by thermodynamic calculations presented in the form of a proposed phase diagram in the T - χ space shown in Fig. 5-2 (Huo et al., 2003; Sloan, 2003; Sloan and Koh, 2008; Sloan et al., 2010). Within the hydrate region of the T - χ phase diagram (dashed box region), hydrate composition does not take on a single value as predicted by its stoichiometry ($\text{CH}_4 \cdot 5.75\text{H}_2\text{O}$, or ≈ 0.148 methane mole fraction). Instead, hydrate composition deviates slightly from the stoichiometric prediction and is dependent on whether it forms in a methane-rich environment (vapor-liquid interface) or a water-rich environment (aqueous solution). As a result, the hydrate-only region (marked H in Fig. 5-2) takes a triangular shape and is enclosed by the L_w -H phase boundary (water-rich) and the H-V phase boundary (methane-rich) that meet at the triple-point. Note that Fig. 5-1 corresponds to the details of the dashed box in Fig. 5-2.

Three-phase coexistence in gas hydrate systems

It is important to note here that in either the P - T or the T - χ phase diagram, the coexistence of all three phases (gas, liquid and hydrate) only occurs at a very specific set of environmental conditions: in the P - T space, three-phase coexistence follows the three-phase line (a fixed pair of P, T); in the T - χ space at a given pressure, three-phase coexistence only occurs at the triple point (a fixed T). In natural or industrial environment, however, pressure, temperature and composition change con-

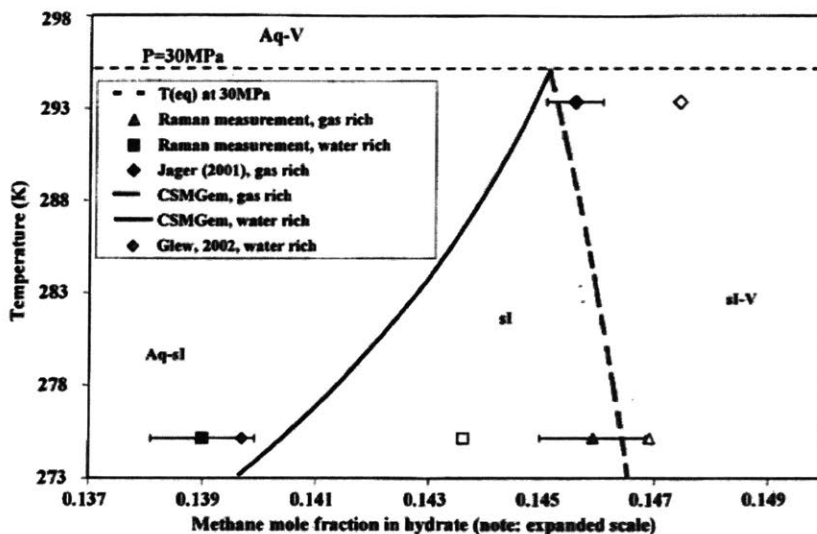


Figure 5-1: Predicted and measured hydrate compositions at 30MPa illustrated in a T - χ phase diagram. Figure is from (Huo et al., 2003). Waiting for permission from John Wiley and Sons.

stantly (e.g. heat released/consumed by hydrate formation/dissociation can change local temperature), meaning that a three-phase coexistence condition is rarely met in reality. Nevertheless, there is an overwhelming amount of observational evidence for three-phase coexistence at both short and long time scale. For instance, the phenomenon of hydrate-crusting gas bubble in water column requires all three phases coexist during the period of bubble ascend (a few minutes). At longer time scale, field surveys reveal that gas pockets can coexist with hydrate and water for a long period of time within marine sediment (Suess et al., 1999). While classical thermodynamic analysis provides a reliable description of hydrate system at equilibrium, the phase diagram alone does not describe non-equilibrium behaviors that are ubiquitous in hydrate systems.

5.1.2 Laboratory experiments

In this section, we briefly describe a high-pressure microfluidic experiment to study the controlled expansion of a hydrate-crusting bubble of xenon (also a hydrate-former), in

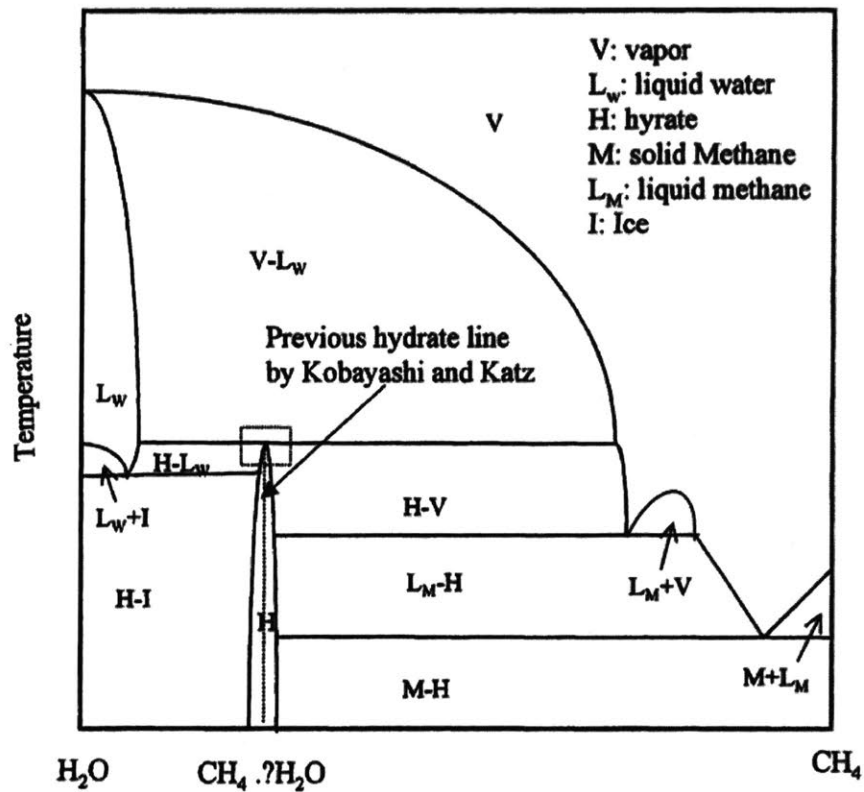


Figure 5-2: The temperature-composition phase diagram for methane-water system from (Huo et al., 2003; Sloan and Koh, 2008; Sloan et al., 2010). Here concentration is given in methane mole fraction. The diagram is not plot to scale in order to emphasize certain features. Figure is taken from (Huo et al., 2003). Waiting for permission from John Wiley and Sons.

a water-filled and pressurized Hele-Shaw cell of 1 mm thickness. The experiments are conducted by Joaquin Jimenez-Martinez and collaborators at Los Alamos National Laboratory. The experimental procedure is designed to replicate the 2D version of previous (Chen et al., 2014, 2016; Warzinski et al., 2014) and ongoing 3D experiments studying the depressurization of a hydrate-crust gas bubble in water column. Experiments in 3D can demonstrate realistic behavior of a free-moving gas bubble under hydrate crust (Chen et al., 2014, 2016; Warzinski et al., 2014); however, capturing the full details of a three-dimensional bubble becomes more challenging. Experiments in 2D have the advantage of being able to image a gas bubble at rest and in a reduced dimensional space; a 2D view of the cross-sectional area of the hydrate-crust bubble provides valuable details for modeling.

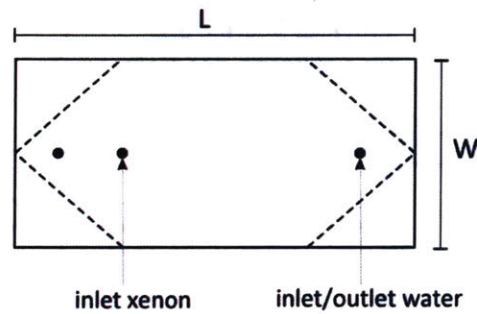


Figure 5-3: Illustration of the Hele-Shaw cell showing the inlet/outlet for water and inlet for Xe.

The system, as shown in Fig. 5-3, is initially pressurized from the xenon gas inlet (i.e., from the Xe gas bubble) and maintained at a constant pressure of 7.5 MPa and constant temperature of 25 °C for 18 hours to ensure equilibrium between xenon-gas and liquid water around the gas bubble (Fig. 5-4, $t = 0$ s). A layer of hydrate shell forms at the gas-liquid interface during this period as the condition is well within the hydrate stability zone for xenon-hydrate (Fig. 5-4). At the end of the 18 hours, the gas inlet is disconnected from the system, and the entire cell is depressurized from the surrounding liquid phase at a constant rate of 0.5 MPa/min. The depressurization process follows the red arrow shown in Fig. 5-4. Fig. 5-5 shows snapshots of the experiments at various times.

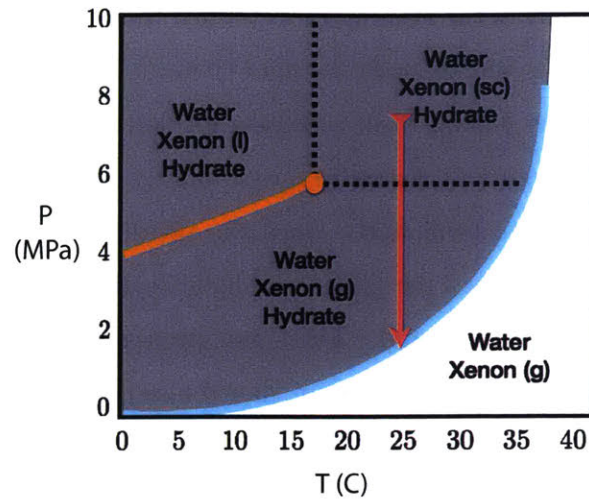


Figure 5-4: Phase diagram for xenon-water system at various pressure and temperature. The orange line marks the gas-liquid phase boundary for xenon. The dashed black box marks the supercritical region of xenon. The blue curve marks the phase boundary for xenon-hydrate stability region (shaded grey). The phase boundaries for xenon-water system (blue and orange) are plotted based on measurements from (Ohgaki et al., 2000) and CSMGem calculations (Sloan and Koh, 2008).

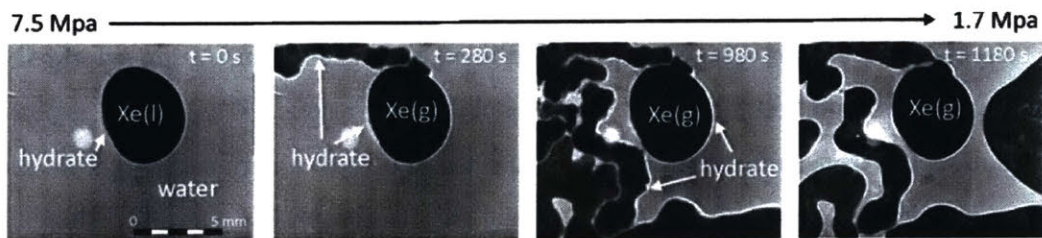


Figure 5-5: Time-lapse of Xe bubble (black) depressurization from the surrounding water (grey) in a Hele-Shaw cell. Gas expands during depressurization, causing a hydrate-encrusted finger to form and migrate.

During depressurization, the expansion of the gas bubble is controlled by three processes illustrated in Fig. 5-6: (1) the volumetric expansion of gas due to changes in pressure; (2) the rupture of the existing hydrate shell that encapsulates the expanding gas phase; and (3) the spontaneous formation of hydrate along the evolving gas-liquid interface. The interplay among these processes results in gas fingering that forms a complex labyrinth pattern, in contrast to the circular gas expansion that would occur in the absence of hydrate formation. Once the pressure drops below the hydrate stability zone, two processes take place: the hydrate shell quickly dissociates, and xenon gas exsolves from the liquid. These two processes lead to the formation of bubbles, followed by their coalescence (not shown here).

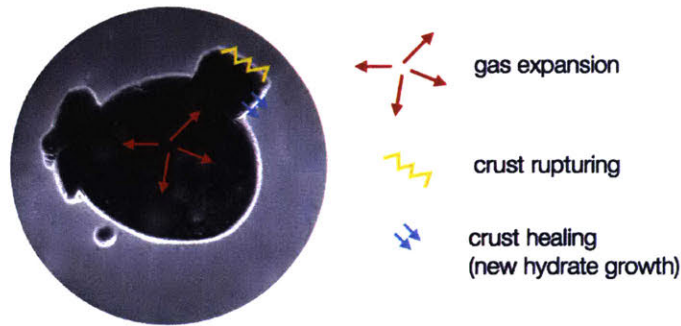


Figure 5-6: The controlled expansion of the hydrate-crust bubble can be decomposed into three mechanisms: gas expansion, crust rupturing and crust healing/growth

In the rest of this Chapter, we describe modeling and simulation efforts that aim to understand some of these experimental observations. We propose a phase-field model that describes the nucleation and thickening of a permeable hydrate shell on a moving gas-liquid interface. In section 5.2, we propose a simplified design of bulk free energy for each of the three phases and demonstrate that our simplified description can replicate the equilibrium phase behavior of methane-water systems in terms of the T - χ phase diagram shown in Fig. 5-2. In section 5.3, we complete the description of total free energy to rigorously account for interfacial effects and phase transformation dynamics (hydrate formation and disappearance, gas dissolution and

exsolution). In section 5.4, we perform numerical simulations of our model to illustrate phase separation dynamics of the methane-water system above and below the triple-point temperature. In section 5.5, we focus on the growth of hydrate on a gas-liquid interface and discuss the key processes that modulate hydrate thickening and methane transport across the interface. In section 5.6, we incorporate gas compressibility into the model to describe the pressure-triggered gas volume expansion. In section 5.7, we model the hydrate shell as a highly viscous fluid phase with shear-thinning rheology to reproduce the rupturing behavior of the hydrate shell.

5.2 Hydrate phase diagram through a simplified free energy description

In this Thesis, we focus on the phase behavior of methane-water system above the freezing point (above the H-I region in Fig. 5-2), where the temperature is high enough and there is always some dissolved methane so that pure water ice does not form. The region of interest entails three key features: (1) a triple point temperature, where all three phases coexist in thermodynamic equilibrium (point 7 in Fig. 5-2); (2) above the triple point, a two-phase region where gas and liquid phases coexist; and (3) below the triple point and above the freezing point, a hydrate-forming region where the thermodynamic equilibrium ends at a gas-hydrate or a liquid-hydrate coexistence, but not all three phases can coexist. There is also a boiling point temperature in our region of interest, above which only vapor phase is possible. The goal of this section is to build a simplified analytical formulation of bulk free energies that can readily replicate the phase behavior of the three-phase system at different temperature and compositions within our interest region. The bulk free energy description is an essential component of our phase-field model introduced in Sec. 5.3. At the end of this section, we demonstrate how our simplified bulk free energy can replicate the three key features of the T - χ phase diagram.

5.2.1 Motivation for a simplified free energy description

Phase-field modeling is a mathematical framework that describes systems that are out of thermodynamic equilibrium (Bray, 1994; Anderson et al., 1998b). First introduced in the context of solidification process and phase transitions (Cahn and Hilliard, 1958), it has since been adopted in the field of multiphase flow (Lowengrub and Truskinovsky, 1998; Sun and Beckermann, 2010; Cueto-Felgueroso and Peraire, 2008; Cueto-Felgueroso and Juanes, 2012b). This approach is particularly fitting in studying bubble dynamics because it provides a natural way to incorporate surface tension effects (Gomez et al., 2010). For a non-hydrated methane bubble, which is a

two-component (CH₄ and water), two-phase (gas and liquid) fluid system, the phase-field approach is built upon a mathematical description of the energy in the system. A phase variable, usually denoted ϕ and $\phi \in [0, 1]$, is chosen to represent the volume fraction of the gas or liquid phase at any given point in the domain. Then the system energy, written as a function of ϕ , can be obtained by summing the *bulk free energy*, which is associated with the gas and liquid in the domain and the *interfacial energy*, which is defined on the gas-liquid interface. Under this framework, the gas-liquid interface is then naturally described as a diffusive, rather than sharp profile of ϕ , which is advantageous from a computation point of view because we do not have to track the interface explicitly in the computational domain.

In addition to numerical robustness, it is also important to ensure that our mathematical description predicts thermodynamic equilibria that are consistent with the physical system. In other words, a thermodynamically-consistent phase-field model should be able to produce a phase diagram that is similar (if not exactly the same) as the real system. In classical thermodynamics simulators (non phase-field framework), the process of constructing phase diagrams based on energy descriptions is often referred to as Gibbs free energy minimization, where the equilibrium states along with some undetermined energy parameters are solved for through an iterative optimization procedure, constrained by experimental measurements (Ballard, A. L. and Sloan, 2004). Under phase-field modeling framework, the advantage of working with pre-determined algebraic expressions of the Gibbs free energies allow us to simplify the construction process. Instead of solving a nonlinear optimization problem with many equations and undetermined parameters, we can obtain equilibrium analytically through the mathematical technique of *common tangent construction* (see Sec. 5.2.5). The idea has been adopted in many phase-field models, in the context of alloy solidification (Nestler et al., 2000), liquid phase separation (Tegze et al., 2005) and hydrate formation in two-phase systems (Svandal et al., 2006). Specifically, the study by (Svandal et al., 2006) uses phase-field framework to model hydrate formation in an aqueous solution at the nano meter scale within micro seconds, but their Gibbs free energy formulations are not readily extendable to describe macroscopic

processes at the temporal and spatial scale applicable to a single gas bubble. In this work, we simplify the Gibbs free energy to more tractable, explicit algebraic expressions, so that they can be readily incorporated to study macroscopic processes. This is similar to the approaches used by (Nestler et al., 2000) in describing binary alloys. The simplified Gibbs free energy allows our model to be thermodynamically consistent while numerically tractable, as it describes the phenomenological *nonequilibrium* dynamics of the hydrate system at a single bubble scale, while still predicting the correct thermodynamic equilibrium.

In the following, we describe the design and construction of simplified Gibbs free energies for a three-phase two-component system analogous to that of methane-water. Our end goal is to produce a phase diagram of our *model* system that is similar to the proposed diagram for methane-water system (Fig. 5-2). The Gibbs free energy is a key component of the total free energy, which we introduce in Sec. 5.3 to describe nonequilibrium dynamics.

5.2.2 Primary variables

In its minimal form, the system we study consists of three phases (methane gas, liquid water and solid hydrate) and two components (CH_4 and H_2O). The gas phase ($\phi_g = 1$) is made of mostly CH_4 and the liquid phase ($\phi_l = 1$) is made of mostly H_2O ; the hydrate phase ($\phi_s = 1$) is made of some CH_4 . We denote ϕ_α as the volumetric fractions of phase α and at any given point in the domain requires that:

$$\phi_g + \phi_l + \phi_s = 1. \quad (5.1)$$

The multiphase mixture is also characterized by the mass fraction of methane, χ , which is the mass of methane (m_{CH_4}) over the total mass at any given point in space:

$$\chi = \frac{m_{\text{CH}_4}}{m_{\text{CH}_4} + m_{\text{H}_2\text{O}}}$$

Alternatively, one can also describe the local composition using molar fraction, C , which is the number of moles of methane (n_{CH_4}) over the total number of moles of components at any given point in space:

$$C = \frac{n_{\text{CH}_4}}{n_{\text{CH}_4} + n_{\text{H}_2\text{O}}}$$

The relationship between the mass fraction χ and the molar fraction C can be derived as:

$$\chi = \frac{M_{\text{CH}_4}C}{M_{\text{CH}_4}C + M_{\text{H}_2\text{O}}(1 - C)},$$

where $M_{\text{CH}_4} = 16\text{g/mol}$ and $M_{\text{H}_2\text{O}} = 18\text{g/mol}$ are the molar mass of methane and water molecules respectively. In the special case of methane-water system, because the molar mass of the two components are very similar, we can approximate the molar fraction with the mass fraction (see also Fig. 5-7 left):

$$\chi = \frac{16C}{16C + 18(1 - C)} \approx C.$$

For xenon-water system, the atomic mass of Xe is 131 g/mol, which is much larger than that of water. Therefore, the same approximation of C as χ would not hold (see Fig. 5-7 right).

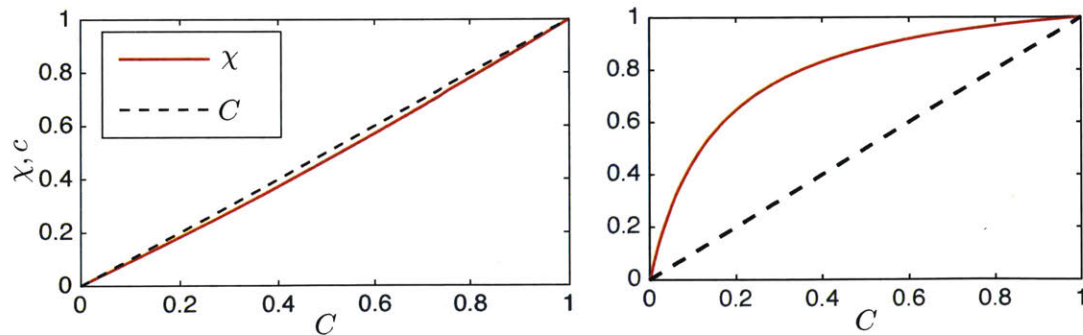


Figure 5-7: Comparison between χ and C as a function of C for methane-water (left) and xenon-water system (right) .

5.2.3 Basic elements in a free energy functional

The total free energy F for our system is expressed as a function of the volume fraction of each phases (ϕ_α) as well as the component molar fractions (χ). One can also include the dependence on pressure (p) and temperature (T) for non-isobaric and non-isothermal systems. For now, we do not consider the effect of pressure in F (so that changes in pressure do not affect thermodynamic equilibrium). The free energy functional describes the energy landscape of the three-phase system, and ultimately defines the equilibrium state where the energy reaches a local minimum. The exact shape of F dictates the path the system takes to get to the minima. In general, F consists of two parts: the bulk free energy and the interfacial energy. In the following section, we focus on the design of the single phase Gibbs free energy (f_α), which is a primary component in the bulk free energy (f_0). In section 5.3, we describe the full formulation of F .

5.2.4 Single phase Gibbs free energy $f_\alpha(\chi)$

We start by describing the Gibbs free energy of each of the three phases in the system. Consider a single phase α , we denote its Gibbs free energy as f_α , and formulate it as a function of local composition χ . Eqs. (5.2)-(5.3) are the Wilson's model of excess Gibbs free energy for the liquid and gas phases (Wilson, 1964). We use a parabolic form for the free energy of the solid phase (Eq. (5.4)), as suggested by the solidification literature (Nestler et al., 2000; Moelans, 2011; Cogswell and Carter, 2011). The expressions inside the curly brackets are dimensionless and the free energies are made dimensional when multiplied by a characteristic energy density ω_{mix} , which has an unit of J/cm³.

$$f_l(\chi) = \omega_{mix} \{ \chi \log(\chi) - (1 - \chi) \log(1 - a_l \chi) - \chi \log(1 - b_l(1 - \chi)) + f_{l0} \}; \quad (5.2)$$

$$f_g(\chi) = \omega_{mix} \{ \chi \log(\chi) - (1 - \chi) \log(1 - a_g \chi) - \chi \log(1 - b_g(T)(1 - \chi)) + f_{g0} \}; \quad (5.3)$$

$$f_s(\chi) = \omega_{mix} \{ a_s(T)(\chi - \chi_s)^2 + b_s(T) + f_{s0} \}. \quad (5.4)$$

The parameters used in these equations control the shapes and relative positions of f_α 's. In Fig. 5-8, we visualize a representative configuration of the three curves (the dimensionless part) using parameter values given in Table 5.1.

Table 5.1: Summary of parameter values used for Gibbs free energy calculations in Eqs. (5.2)-(5.4) and Fig. 5-8.

Parameters in f_l			Parameters in f_g			Parameters in f_s			
a_l	b_l	f_{l0}	a_g	b_g	f_{g0}	a_s	χ_s	b_s	f_{s0}
-3.71×10^8	1	-20	1	-5.94×10^9	-20	1400	0.147	4.52	-42

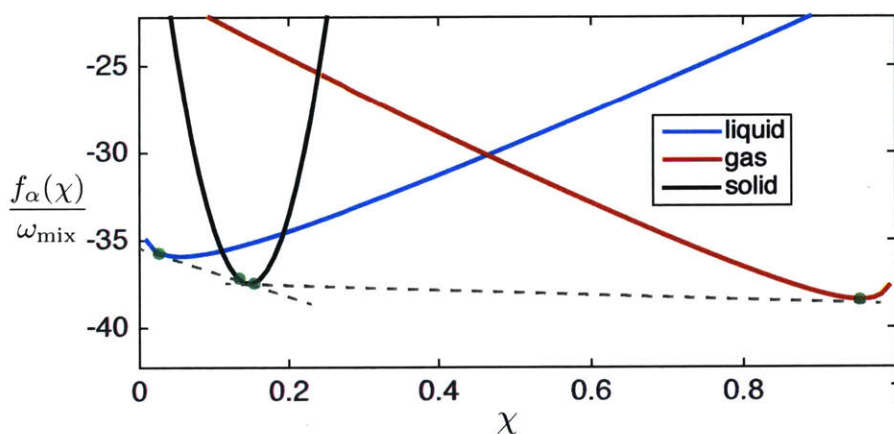


Figure 5-8: The bulk free energy of each phases, $f_\alpha(\chi)$, as introduced in Eq. (5.2)-(5.4): gas (red), liquid (blue) and solid (black). The grey dashed lines are the common tangents for liquid-solid and gas-solid curves. The green dots mark the tangent points obtained from the constructions. The common tangent for liquid-gas pair is not shown here.

The derivative of the Gibbs free energy, $\partial f_\alpha(\chi)/\partial\chi$, is the chemical potential (Ψ_α) that drives equilibration process. Its magnitude is linearly proportional to the instantaneous rate of phase evolution/reaction. The equilibrium composition of α , χ_α^{eq} , is located at the local minima of $f_\alpha(\chi)$. For instance, in the system described by Eqs. (5.2)-(5.4) and Fig. 5-8, the liquid phase at equilibrium has a composition of $\chi_l^{\text{eq}} \approx 0.05$ and similarly $\chi_g^{\text{eq}} \approx 0.95$, $\chi_s^{\text{eq}} \approx 0.15$. However, these equilibrium points no longer apply if one phase is in the presence of a second phase. When two phases coexist in the system, the equilibrium compositions are obtained through common tangent constructions.

5.2.5 The common tangent construction technique for three-phase system

The common tangent construction (van der Waals, 1894; J., 1875; Rowlinson, 1979), as described in Chapter 3, is a mathematical technique to obtain equilibrium compositions between two phases given the description of their Gibbs free energy, $f_\alpha(\chi)$. For a given phase pair i and j , the construction is intended to locate a composition in each phase (χ_i and χ_j) such that their chemical potentials (the slopes of f_α , or f'_α) are identical and equal to the slope of the straight line (tangent line) that connects the two points. Mathematically, this can be posed as solving the system of two equations for the equilibrium compositions χ_i and χ_j :

$$f'_i(\chi_i) = f'_j(\chi_j); \quad (5.5)$$

$$f_i(\chi_i) - f_j(\chi_j) = (\chi_i - \chi_j)f'_i(\chi_i), \quad (5.6)$$

where Eq. (5.5) enforces the equivalence of chemical potentials and Eq. (5.6) enforces the equivalence of the tangent line slope to the chemical potential. Because f_α is nonlinear in our system, we solve for χ_i, χ_j using `fsolve` in MATLAB .

This technique can be readily extended to three-phase system, where the construction is performed three times, one for each phase pairing. An example of this construction is shown in Fig. 5-8, where we plot the common tangents for gas-hydrate and liquid-hydrate pairing. Here, we do not show the gas-liquid construction because their tangent points fall into the metastable region of the other constructions, rendering the gas-liquid construction irrelevant (because their equilibrium points are unstable under the influence of the hydrate phase). The common tangent constructions in Fig. 5-8 describes that:

1. At liquid-hydrate equilibrium: $\chi_l^{\text{eq}} \approx 0.03$ and $\chi_s^{\text{eq}} \approx 0.141$;
2. At hydrate-gas equilibrium: $\chi_g^{\text{eq}} \approx 0.96$ and $\chi_s^{\text{eq}} \approx 0.146$

Notice that these equilibrium compositions do not necessarily coincide with the values of single phase equilibrium described in Sec. 5.2.4. In addition, the hydrate phase

compositions differs between the two types of equilibrium, where hydrate has a higher composition when formed in equilibrium with the gas phase. This observation is consistent with recent experimental measurements and CSMGem calculations (Huo et al., 2003; Sloan et al., 2010), as we discussed earlier in Sec. 5.1.1.

5.2.6 Single phase Gibbs free energy $f_\alpha(\chi, T)$

Phase-phase equilibrium is not only defined by composition, but also often times controlled by temperature. For instance, gas solubility in water often decreases as temperature increases. To incorporate temperature effects on phase equilibrium, we need to introduce T into the description of f_α 's. To a first-order effect, this is often achieved via multiplying the entire expression by T . However, many others (Wilson, 1964; Wheeler et al., 1993; Nestler et al., 2000; Moelans, 2011; Plapp, 2011; Choudhury et al., 2011) have proposed alternative ways of formulating nonlinear dependence on T into algebraic free energy expressions similar to the ones in Eqs. (5.2)-(5.4). Here, we modify Eqs. (5.2)-(5.4) to account for temperature dependence of Gibbs free energy as suggested by (Wilson, 1964) for gas and liquid, in Eqs. (5.7)-(5.8), and as suggested by the solidification literature (Nestler et al., 2000; Moelans, 2011; Cogswell and Carter, 2011) for the solid phase, in Eq. (5.9).

$$f_l(\chi, T) = \omega_{\text{mix}} \{ \chi \log(\chi) - (1 - \chi) \log(1 - a_l(T)\chi) - \chi \log(1 - b_l(1 - \chi)) + f_{l0} \}; \quad (5.7)$$

$$f_g(\chi, T) = \omega_{\text{mix}} \{ \chi \log(\chi) - (1 - \chi) \log(1 - a_g\chi) - \chi \log(1 - b_g(T)(1 - \chi)) + f_{g0} \}; \quad (5.8)$$

$$f_s(\chi, T) = \omega_{\text{mix}} \{ a_s(T)(\chi - \chi_s)^2 + b_s(T) + f_{s0} \}, \quad (5.9)$$

where some parameters depend on T (unit in $^{\circ}C$):

$$\begin{aligned} a_l &= a_{l0}/(T/T_c)^4; \\ b_g &= b_{g0}/(T/T_c)^2; \\ a_s &= a_{s0}(T/T_c)^{1/3}; \quad b_s = b_{s0}(T/T_c)^{6/5} \end{aligned} \tag{5.10}$$

Here $T_c = 1^{\circ}C$ is used to render the temperature dependent coefficients dimensionless. Using the updated expressions, we visualize the free energy curves and their common tangent constructions at four different temperatures in Fig. 5-9 using the parameter values given in Table 5.2.

Table 5.2: Summary of parameter values used for Gibbs free energy calculations in Eqs. (5.7)-(5.9) along with the temperature dependent parameters described in Eq. (5.10).

Parameters in f_l			Parameters in f_g			Parameters in f_s			
a_{l0}	b_l	f_{l0}	a_g	b_g	f_{g0}	a_s	χ_s	b_s	f_{s0}
-1×10^9	1	8	1	-1×10^9	8	500	0.14	0.5	-15

Fig. 5-9 illustrates a few key behaviors of the methane-water system at different temperatures:

- At high enough temperature ($T = 20^{\circ}C, 60^{\circ}C$), hydrate does not form. The equilibrium is defined by two composition values: χ_l^{eq} and χ_g^{eq} . To the left of χ_l^{eq} is a single phase region of aqueous phase (L_w); to the left of χ_g^{eq} is a single phase region of gas phase (V); in between the two points is a two-phase region (L_w - V);
- Within the no-hydrate region, the L_w - V two-phase equilibrium compositions change as temperature changes ($T = 20^{\circ}C, 60^{\circ}C$);
- At the *triple point* temperature ($T^T = 18.6^{\circ}C$), a straight line can be drawn tangent to all three energy curves, indicating that all three phases can coexist at this temperature and at the composition values indicated by the tangent points.

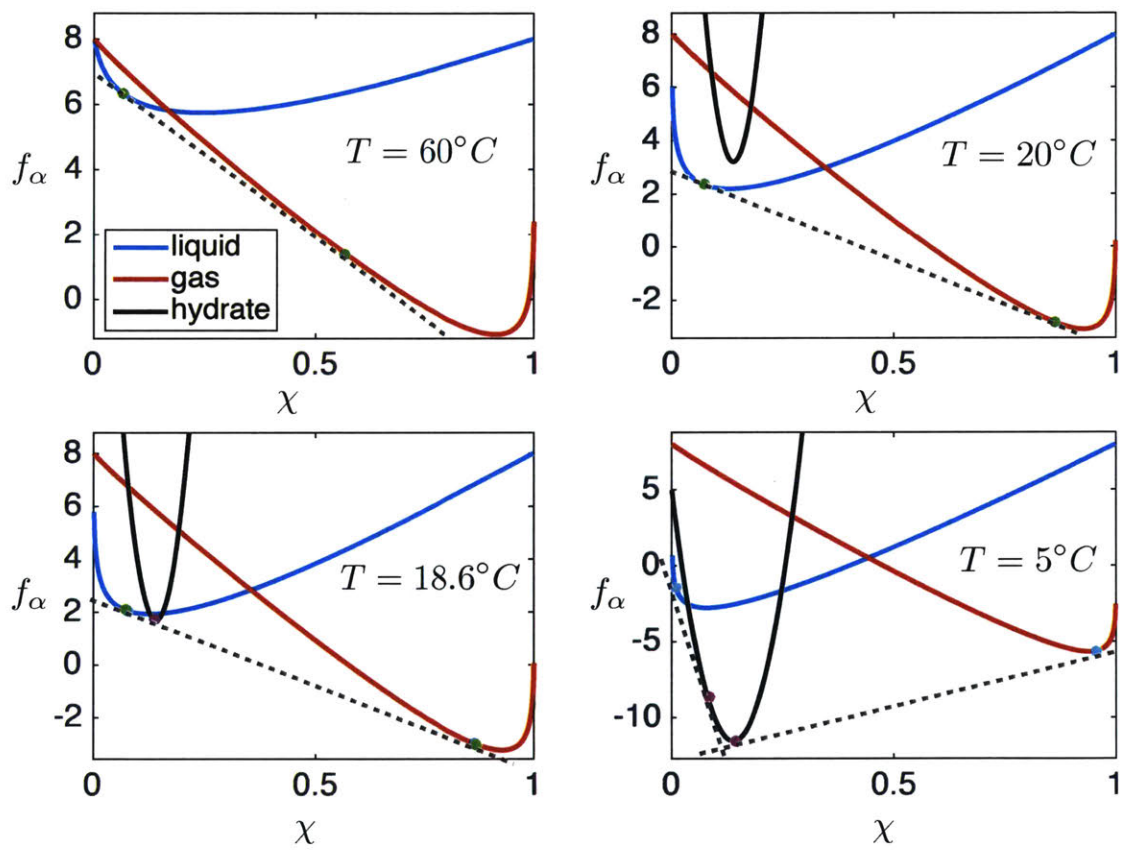


Figure 5-9: Gibbs free energy of all phases (f_α) at various temperatures. The feasible common tangent constructions are plotted in dashed grey line.

- At $T = 5^\circ C$, the temperature drops below the triple point and hydrate can readily form. The equilibrium is defined by four composition values (from left to right in the figure): $\chi_l^{\text{eq}} \approx 0.0092$, $\chi_{sl}^{\text{eq}} \approx 0.0824$, $\chi_{sg}^{\text{eq}} \approx 0.1442$, $\chi_g^{\text{eq}} \approx 0.958$. These four points divide the domain into five segments, corresponding to five equilibrium scenarios. The domain averaged composition ($\bar{\chi}$) determines which equilibrium the system will arrive at : (1) If $\bar{\chi} < 0.0092$, the equilibrium consists of only liquid; (2) If $0.0092 < \bar{\chi} < 0.0824$, the equilibrium consists of liquid and hydrate; (3) If $0.0824 < \bar{\chi} < 0.1442$, the equilibrium consists of only hydrate; (4) If $0.1442 < \bar{\chi} < 0.958$, the equilibrium consists of gas and hydrate; (5) If $\bar{\chi} > 0.958$, the equilibrium consists of only gas.

5.2.7 An isobaric phase diagram based on simplified Gibbs free energy

Following the exercise in Sec. 5.2.6 for a given temperature, here we perform the calculations for all temperatures between $T = 4^\circ C$ and $T = 80^\circ C$ (with a temperature increment of $0.1^\circ C$) and plot the equilibrium compositions as a function of temperature (Nestler et al., 2000; Tegze et al., 2005; Svandal et al., 2006). This yields an isobaric (fixed pressure) T - χ phase diagram shown in Fig. 5-10. The structure of the phase diagram bears good resemblance to that for methane-water system (Fig. 5-2 and (Huo et al., 2003; Sloan et al., 2010)). In this *model* system, the triple point is determined to be $T^T \approx 18.6^\circ C$ and $\chi_l = 0.07, \chi_s \approx 0.138, \chi_g = 0.87$. In the real methane hydrate system, the corresponding value would be $\chi_l = 0.0014, \chi_s = 0.14, \chi_g = 0.9997$ (Huo et al., 2003; Sloan et al., 2010). In the next section, we discuss how model parameters can be optimized to better match triple point values with experimental measurement.

5.2.8 Isobaric phase diagram at different pressures

In this section, we introduce a parameter optimization framework that allows us to design modeled T - χ phase diagrams that best imitates the real system. The ability to parameter-fit our model to existing experimental measurements allows us to refine

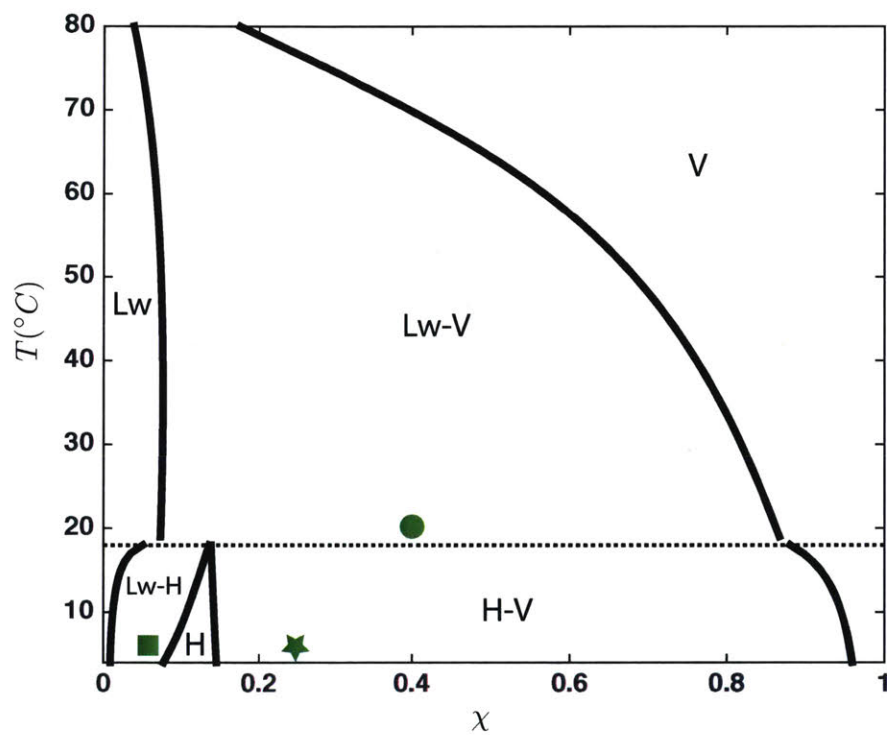


Figure 5-10: The $T - \chi$ phase diagram obtained analytical from our *model* three-phase system based on Eqs. (5.7)-(5.9) and Eq. (5.10). The parameter values come from Table 5.2.

the important features of the phase diagram (e.g. the hydrate-only region in Fig. 5-1), providing a strong connection of our model to the real system. Additionally, it also allows us to simulate the systems at different pressures, given that we have pre-existing knowledge on how pressure can change some important features of the phase diagram (Kamath, 1984; Sloan and Koh, 2008). In Fig. 5-11, we enumerate three key features of the methane-water phase diagram above the freezing point. The diagram is a conceptual cartoon drawing of the proposed one in Fig. 5-2, where the hydrate-forming region is not drawn to scale. Specifically, we identify three temperatures and their associated composition points:

1. The boiling point T^B and the boiling point composition χ^B ;
2. The triple point T^T and the relevant compositions: $\chi_l^T, \chi_s^T, \chi_g^T$;
3. A temperature above the freezing point, denoted T^F , and the relevant compositions at that temperature: $\chi_l^F, \chi_{sl}^F, \chi_{sg}^F, \chi_g^F$. Note the choice of this temperature is rather arbitrary and depends on availability of experimental data on the relevant compositions.

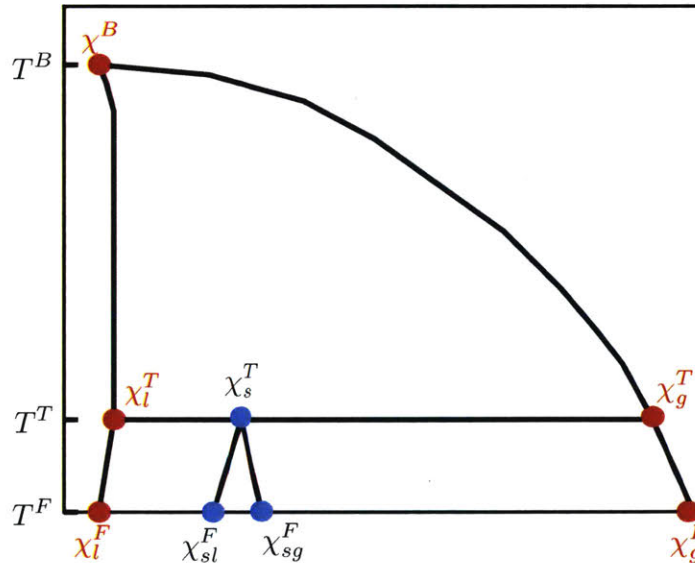


Figure 5-11: The $T-\chi$ phase diagram obtained analytical from our *model* three-phase system.

Given the proposed form of $f_\alpha(\chi, T)$ in Eqs. (5.7)–(5.9), here we adopt a slightly simplified formula for the temperature dependent parameters (note slight modification from Eqs. (5.10)):

$$\begin{aligned} a_l &= a_{l0}/(T/T_c)^4; \\ b_g &= b_{g0}/(T/T_c)^2; \\ a_s &= a_{s0}(T/T_c); \quad b_s = b_{s0}(T/T_c) \end{aligned} \tag{5.11}$$

In Eqs. (5.7)–(5.9), we assume the fixed parameters are b_l , f_{l0} , a_g , f_{g0} , f_{s0} , whose values are given in Table 5.3.

Table 5.3: Summary of fixed parameter values used for free energy calculations in Eqs. (5.7)–(5.9)

Parameters in f_l		Parameters in f_g		Parameters in f_s
b_l	f_{l0}	a_g	f_{g0}	f_{s0}
1	−20	1	−20	−42

Additionally, we assume that the following values are known *a priori*:

$$T^B, T^T, T^F, \chi_s^T, \chi_{sg}^F, \chi_{sl}^F.$$

Specifically, we can calculate the triple point temperature of the methane-water system at a given temperature using the following formula provided in Kamath (1984) (note: this formula requires $T \in [0, 25]^\circ\text{C}$):

$$P[\text{kPa}] = \exp(a + b/T^T[\text{K}]); \quad a = 38.98, \quad b = -8533.8 \tag{5.12}$$

The rest of the parameters can be obtained from existing experiments such as (Huo et al., 2003) or empirical formulas. There are five unknown parameters in the free energies:

$$a_{l0}, b_{g0}, a_{s0}, b_{s0}, \chi_s$$

along with five undetermined values (free parameters) in the phase diagram:

$$\chi^B, \chi_g^T, \chi_l^T, \chi_g^F, \chi_l^F$$

In order to determine the 10 unknown parameters (five from free energies and five from phase diagram), we solve the following system of 10 equations (this guarantees a determined system):

- At boiling point temperature T^B :

$$f'_g(\chi^B, T^B) = f'_l(\chi^B, T^B); \quad (5.13)$$

$$f_g(\chi^B, T^B) = f_l(\chi^B, T^B); \quad (5.14)$$

- At triple point temperature T^T and given χ_s^T :

$$f'_g(\chi_g^T, T^T) = f'_l(\chi_l^T, T^T); \quad (5.15)$$

$$f'_l(\chi_l^T, T^T) = f'_s(\chi_s^T, T^T); \quad (5.16)$$

$$f_g(\chi_g^T, T^T) - f_l(\chi_l^T, T^T) = (\chi_g^T - \chi_l^T) f'_g(\chi_g^T, T^T) \quad (5.17)$$

$$f_g(\chi_g^T, T^T) - f_s(\chi_s^T, T^T) = (\chi_g^T - \chi_s^T) f'_g(\chi_g^T, T^T) \quad (5.18)$$

- At temperature T^F , given χ_{sl}^F from the L_w-H equilibrium:

$$f'_l(\chi_l^F, T^F) = f'_s(\chi_s^F, T^F); \quad (5.19)$$

$$f_l(\chi_l^F, T^F) - f_s(\chi_s^F, T^F) = (\chi_l^F - \chi_s^F) f'_l(\chi_l^F, T^F) \quad (5.20)$$

- At temperature T^F , given χ_{sg}^F from the H-V equilibrium:

$$f'_g(\chi_g^F, T^F) = f'_s(\chi_s^F, T^F); \quad (5.21)$$

$$f_g(\chi_g^F, T^F) - f_s(\chi_s^F, T^F) = (\chi_g^F - \chi_s^F) f'_g(\chi_g^F, T^F) \quad (5.22)$$

In the following two sections, we demonstrate how this technique is applied to construct T - χ phase diagram at two different pressures.

Isobaric T - χ phase diagram at $P = 5\text{MPa}$

At $P = 5\text{MPa}$, we calculate using Eq. (5.12) that the triple point temperature is $T^T = 6.85^\circ\text{C}$ (or 280 K). The boiling point of water at 5MPa is about $T^B = 264^\circ\text{C}$ (or 537.15 K). We take $T^F = 4^\circ\text{C}$ and use the data reported in (Huo et al., 2003) (note the data is at 30MPa): $\chi_{sl}^F \approx 0.141$, $\chi_{sg}^F \approx 0.1465$. We report the optimized parameters in table 5.4 and plot the phase diagram in Fig. 5-12. In keeping with similar diagrams reported in earlier literature (Huo et al., 2003; Sloan et al., 2010), we convert the unit of temperature to Kelvin here.

Table 5.4: Summary of parameter values used for Gibbs free energy calculations in Eqs. (5.7)-(5.9) and Eq. (5.10) to produce the phase diagram in Fig. 5-12 at $P = 5\text{MPa}$.

Parameters in f_l			Parameters in f_g			Parameters in f_s			
a_{l0}	b_l	f_{l0}	a_g	b_g	f_{g0}	a_s	χ_s	b_s	f_{s0}
-9.5×10^{10}	1	-20	1	-9.5×10^{10}	-20	350	0.147	1.13	-42

We want to point out that the shape and features of our modeled phase diagram is very similar to the one reported in experimental studies (Huo et al., 2003) at 5MPa (Fig. 5-2, above the freezing point).

Isobaric T - χ phase diagram at $P = 30\text{MPa}$

At $P = 30\text{MPa}$, the triple point temperature is calculated as $T^T = 24.5^\circ\text{C}$ (or 297 K) based on Eq. (5.12). A boiling point does not exist at 30MPa, so here we do not perform parameter fitting of the L_w -V region and focus on the region around the triple point. We take $T^F = 4^\circ\text{C}$ and use the data reported in (Huo et al., 2003) for 30MPa: $\chi_{sl}^F \approx 0.141$, $\chi_{sg}^F \approx 0.1465$. We report the optimized parameters in table 5.5 and plot the phase diagram in Fig. 5-13. Note that the hydrate forming region (Fig. 5-13b) bears good resemblance to the ones proposed in (Huo et al., 2003) at 30MPa.

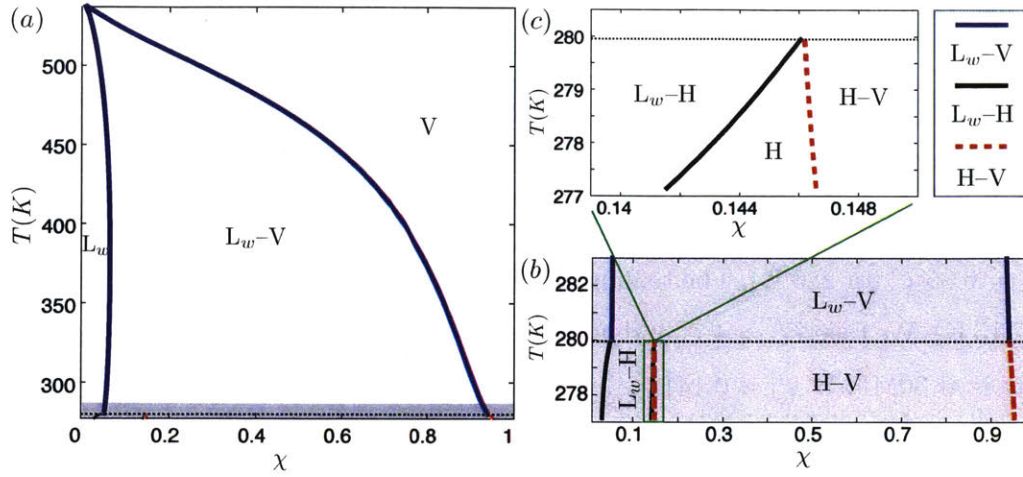


Figure 5-12: The $T - \chi$ phase diagram obtained analytical from our *model* three-phase system at $P = 5$ MPa. The blue line represents compositions calculated for L_w -V equilibrium. Similarly, the red dashed lines are for H-V equilibrium and the black line is for L_w -H equilibrium. Sub figure (b) is the enlarged version of the shaded grey area in (a). Sub figure (c) is the blowup of the green box in (b). The dashed line marks the triple point temperature in all sub figures.

Table 5.5: Summary of parameter values used for Gibbs free energy calculations in Eqs. (5.7)-(5.9) and Eq. (5.10) to produce the phase diagram in Fig. 5-13 at $P = 30$ MPa.

Parameters in f_l			Parameters in f_g			Parameters in f_s			
a_{l0}	b_l	f_{l0}	a_g	b_g	f_{g0}	a_s	χ_s	b_s	f_{s0}
-1×10^9	1	-20	1	-1×10^9	-20	1200	0.146	0.65	-40

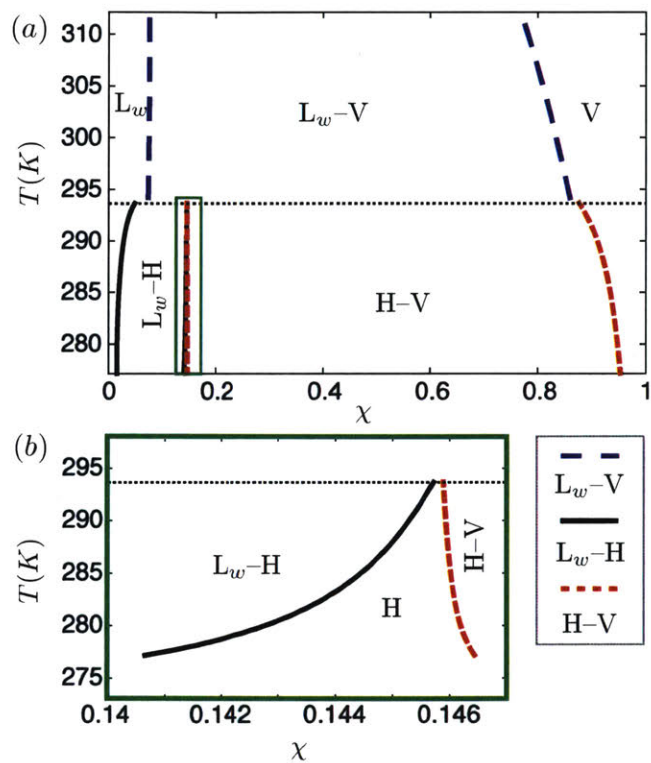


Figure 5-13: The $T-\chi$ phase diagram obtained analytical from our *model* three-phase system at $P = 30\text{MPa}$. The blue dashed line represents compositions calculated for L_w-V equilibrium. Similarly, the red dashed lines are for $H-V$ equilibrium and the black line is for L_w-H equilibrium. Sub figure (b) is the blowup of the green box in (a). The dashed line marks the triple point temperature.

5.3 Phase-field modeling of phase separation dynamics

In previous section, we describe how to predict phase equilibriums in a three-phase system using the technique of common tangent constructions. Through this technique, we can arrive at equilibrium phase behaviors at a given temperature. In this section, we complete the description of the total free energy F and use it to predict the nonequilibrium dynamics of phase separation processes towards these equilibriums. We first finish the description of the bulk free energy f_0 in section 5.3.1 and then add the interfacial terms in section 5.3.2. We then proceed to introduce the evolution equations for χ and ϕ_α in Sec. 5.3.3 and 5.3.4. In Sec. 5.4, we show high-resolution simulations of phase separation dynamics of our model system at different temperatures.

5.3.1 The bulk free energy density of a three-phase system

To consider the coexistence of multiple phases, here we formulate a more general energy description that incorporates (1) the single phase behaviors of all phases and (2) a functional description of phase-separation and coexistence. In its simplest form, this is achieved by constructing the bulk free energy density, $f_0(\chi, \{\phi\}, T)$, as summation of two parts:

$$f_0(\chi, \{\phi_\alpha\}, T) = \omega_{\text{mix}} \left\{ G_g(\{\phi_\alpha\}) f_g(\chi, T) + G_l(\{\phi_\alpha\}) f_l(\chi, T) + G_s(\{\phi_\alpha\}) f_s(\chi, T) \right\} \\ + \omega_{gl} \phi_g^2 \phi_l^2 + \omega_{gs} \phi_g^2 \phi_s^2 + \omega_{sl} \phi_s^2 \phi_l^2. \quad (5.23)$$

The first row of Eq. (5.23) is the blended energy of f_α from all phases. The blending functions, $G_\alpha(\{\phi_\alpha\})$, are chosen so that the following criteria are met:

$$G_j(\phi_i, \phi_j, 0) = 1 - G_i(\phi_i, \phi_j, 0); \quad (5.24)$$

$$\frac{\partial}{\partial \phi_i} G_i(1, 0, 0) = 0; \quad (5.25)$$

$$\frac{\partial}{\partial \phi_i} G_i(0, \phi_j, \phi_k) = 0. \quad (5.26)$$

The first constraint serves to conserve the summation of all phase variables (volume fractions) to be one. The second and third constraints are to prevent negative phase fractions when one solves for the dynamical evolution of the system numerically. In this work, we take the blending function for a three-phase system suggested by (Folch and Plapp, 2005):

$$G_i(\{\phi_\alpha\}) = \frac{\phi_i^2}{4} \left\{ 15(1 - \phi_i)[1 + \phi_i - (\phi_k - \phi_j)^2] + \phi_i(9\phi_i^2 - 5) \right\}. \quad (5.27)$$

The second row of Eq. (5.23) is the triple-well energy that enforces phase separation. Mathematically, this construction encourages the phase volume fractions to take a value of 0 or 1 at a given point in the domain. Any values between 0 and 1, or outside of the interval $[0, 1]$ are penalized energetically.

5.3.2 Total free energy of a three-phase system

The total free energy, made of the bulk free energy $f_0(\alpha)$ and the interfacial energy (gradient square terms in the following equation), is defined as:

$$\begin{aligned} F(\chi, \{\phi\}, T) = \int_V & \left[f_0(\chi, \{\phi\}, T) \right. \\ & + \left(\epsilon_{gl}^2(T) \nabla \phi_g \cdot \nabla \phi_l + \epsilon_{gs}^2(T) \nabla \phi_g \cdot \nabla \phi_s + \epsilon_{sl}^2(T) \nabla \phi_s \cdot \nabla \phi_l \right) \\ & + \left(\epsilon_g^2(T) |\nabla \phi_g|^2 + \epsilon_l^2(T) |\nabla \phi_l|^2 + \epsilon_s^2(T) |\nabla \phi_s|^2 \right) \\ & \left. + \epsilon_c^2(T) |\nabla \chi|^2 \right] dV. \end{aligned} \quad (5.28)$$

The parameters ϵ_α^2 and $\epsilon_{\alpha\beta}^2$ are positive coefficients related to the interfacial tension originated from phase-phase interactions and compositional gradients. These parameters are directly related to the thickness of the physical phase-phase interface: $\epsilon_\phi^2 = \mathcal{H}b^2$, where \mathcal{H} is the nucleation barrier energy and b is the interface thickness. Because surface tension generally decreases as temperature increases, it is important to consider these interfacial parameters temperature-dependent. Here, we prescribe that:

$$\epsilon_\alpha^2(T) = \epsilon_\alpha^{2,\text{ref}} / \sqrt{T/T_{\text{ref}}}, \quad (5.29)$$

where $\epsilon_\alpha^{2,\text{ref}}$ is a reference value at a reference temperature T_{ref} . Numerically, the value of ϵ_α^2 controls the thickness of the diffuse interface: a larger ϵ_α^2 produces a thicker interface under a well-resolved numerical grid.

5.3.3 Conservation of methane mass

For now, we assume that all phases have the same constant density ρ and no flow is present; then the conservation of methane mass is described by:

$$\frac{\partial \rho \chi}{\partial t} - r_\chi \nabla \cdot \left(D(\{\phi_\alpha\}) \rho \nabla \Psi_c \right) = 0. \quad (5.30)$$

The parameter r_χ is compositional mobility, which is related to the diffusion coefficient:

$$r_\chi = \frac{D_c / \nu}{RT}, \quad (5.31)$$

with D_c being a characteristic diffusion coefficient and ν molar density. The dimensionless $D(\{\phi_\alpha\})$ is a mixture diffusion coefficient that enforces drastically different diffusive time scales inside each phase. We take the average of the three diffusion coefficients, weighted by the respective phase fraction ϕ_α and reach the mixture diffusion coefficient (dimensionless):

$$D(\{\phi_\alpha\}) = \phi_l D_l + \phi_s D_s + \phi_g D_g \quad (5.32)$$

The dimensionless diffusion coefficients for each phase, D_l , D_g and D_s are normalized by the gas-phase diffusion coefficient D_{gas} . Thus $D_g = 1$ in all cases. The point-wise chemical potential (density of potential) that drives diffusion is defined as the variational derivative of the free energy functional with respect to χ :

$$\begin{aligned}\Psi_c &= \frac{\partial F}{\partial \chi} - \nabla \cdot \left(\frac{\partial F}{\partial (\nabla \chi)} \right) \\ &= \omega_{\text{mix}} \left(G_g(\{\phi_\alpha\}) f'_g(\chi) + G_s(\{\phi_\alpha\}) f'_s(\chi) + G_l(\{\phi_\alpha\}) f'_l(\chi) \right) - 2\epsilon_c^2 \nabla^2 \chi.\end{aligned}\quad (5.33)$$

5.3.4 Evolution equation for ϕ_α

The evolution equations for the phase variables are formulated as simple kinetic reaction equations, where the reactive sink/source terms are driven by the phase potentials. In the context of phase-field models, these are called Allen-Cahn equations, which are used to describe the evolution dynamics for non-conserved order parameters such as ϕ_α :

$$\frac{\partial \phi_\alpha}{\partial t} + r_\phi \Psi_\alpha = 0, \quad (5.34)$$

subject to the constraint that:

$$\phi_l + \phi_g + \phi_s = 1. \quad (5.35)$$

Here we implement the constraint using the method of Lagrange multiplier, where $\lambda = 1/3 \sum \partial \phi_\alpha / \partial t$ is the Lagrange multiplier when solving Eq. (5.34). The point-wise phase potentials are given as:

$$\begin{aligned}\Psi_g &= \frac{\partial F}{\partial \phi_g} - \nabla \cdot \left(\frac{\partial F}{\partial (\nabla \phi_g)} \right) \\ &= \omega_{\text{mix}} G'_g(\{\phi_\alpha\}) f_g(\chi) + 2\phi_g(\omega_{gl} \phi_l^2 + \omega_{gs} \phi_s^2) - (2\epsilon_g^2 \nabla^2 \phi_g + \epsilon_{gl}^2 \nabla^2 \phi_l + \epsilon_{gs}^2 \nabla^2 \phi_s);\end{aligned}\quad (5.36)$$

$$\begin{aligned}
\Psi_l &= \frac{\partial F}{\partial \phi_l} - \nabla \cdot \left(\frac{\partial F}{\partial (\nabla \phi_l)} \right) \\
&= \omega_{\text{mix}} G'_l(\{\phi_\alpha\}) f_l(\chi) + 2\phi_l(\omega_{gl}\phi_g^2 + \omega_{sl}\phi_s^2) - (\epsilon_{gl}^2 \nabla^2 \phi_g + 2\epsilon_l^2 \nabla^2 \phi_l + \epsilon_{sl}^2 \nabla^2 \phi_s);
\end{aligned} \tag{5.37}$$

$$\begin{aligned}
\Psi_s &= \frac{\partial F}{\partial \phi_s} - \nabla \cdot \left(\frac{\partial F}{\partial (\nabla \phi_s)} \right) \\
&= \omega_{\text{mix}} G'_s(\{\phi_\alpha\}) f_s(\chi) + 2\phi_s(\omega_{gs}\phi_g^2 + \omega_{sl}\phi_l^2) - (\epsilon_{gs}^2 \nabla^2 \phi_g + \epsilon_{sl}^2 \nabla^2 \phi_l + 2\epsilon_s^2 \nabla^2 \phi_s);
\end{aligned} \tag{5.38}$$

5.3.5 Summary of model equations and parameters

In table 5.6, we provide a summary of model parameters used in Eqs. (5.30),(5.33)-(5.38). In dimensionless form, the model equations can be rewritten as:

$$\frac{\partial \chi}{\partial t} - R_\chi \nabla \cdot \left(D(\{\phi_\alpha\}) \nabla \Psi_c \right) = 0; \tag{5.39}$$

$$\frac{\partial \phi_l}{\partial t} + R_\phi \Psi_l = 0; \tag{5.40}$$

$$\frac{\partial \phi_g}{\partial t} + R_\phi \Psi_g = 0; \tag{5.41}$$

$$\frac{\partial \phi_s}{\partial t} + R_\phi \Psi_s = 0; \tag{5.42}$$

$$\phi_l + \phi_g + \phi_s = 1, \tag{5.43}$$

with the dimensionless potentials given by:

$$\Psi_c = \frac{1}{\text{Ma}} \left(G_g(\{\phi_\alpha\}) f'_g(\chi) + G_s(\{\phi_\alpha\}) \phi_s f'_s(\chi) + G_l(\{\phi_\alpha\}) f'_l(\chi) \right) - \frac{2\epsilon}{\sqrt{T/T_{\text{ref}}}} \nabla^2 \chi. \quad (5.44)$$

$$\Psi_g = \frac{1}{\text{Ma}} G'_g(\{\phi_\alpha\}) f_g(\chi) + 2\phi_g \left(\frac{1}{\text{Ch}_{gl}} \phi_l^2 + \frac{1}{\text{Ch}_{gs}} \phi_s^2 \right) - \frac{1}{\sqrt{T/T_{\text{ref}}}} (2\epsilon^g \nabla^2 \phi_g + \epsilon^{gl} \nabla^2 \phi_l + \epsilon^{gs} \nabla^2 \phi_s); \quad (5.45)$$

$$\Psi_l = \frac{1}{\text{Ma}} G'_l(\{\phi_\alpha\}) f_l(\chi) + 2\phi_l \left(\frac{1}{\text{Ch}_{gl}} \phi_g^2 + \frac{1}{\text{Ch}_{sl}} \phi_s^2 \right) - \frac{1}{\sqrt{T/T_{\text{ref}}}} (\epsilon^{gl} \nabla^2 \phi_g + 2\epsilon^l \nabla^2 \phi_l + \epsilon^{sl} \nabla^2 \phi_s); \quad (5.46)$$

$$\Psi_s = \frac{1}{\text{Ma}} G'_s(\{\phi_\alpha\}) f_s(\chi) + 2\phi_s \left(\frac{1}{\text{Ch}_{gs}} \phi_g^2 + \frac{1}{\text{Ch}_{sl}} \phi_l^2 \right) - \frac{1}{\sqrt{T/T_{\text{ref}}}} (\epsilon^{gs} \nabla^2 \phi_g + \epsilon^{sl} \nabla^2 \phi_l + 2\epsilon^s \nabla^2 \phi_s). \quad (5.47)$$

Here the dimensionless kinetic coefficients R_χ and R_α are defined as:

$$R_\chi = \frac{r_\chi \epsilon_\phi^2 t_c}{b^4}; \quad R_\alpha = \frac{r_\alpha \epsilon_\phi^2 t_c}{b^2}, \quad (5.48)$$

where t_c is the characteristic time scale and b is the characteristic length. The solutal Marangoni number Ma (Fu et al., 2016), which sets the ratio between interfacial energy and mixing energy, is defined as:

$$\text{Ma} = \frac{\epsilon_\phi^2 / b^2}{\omega_{\text{mix}}}, \quad (5.49)$$

where ϵ_ϕ^2 / b is a characteristic surface tension. The Cahn numbers, which control the thickness of the numerical interfaces, are defined as:

$$\text{Ch}_{\alpha\beta} = \frac{\epsilon_\phi^2 / b^2}{\omega_{\alpha\beta}}; \quad \text{Ch}_\alpha = \frac{\epsilon_\phi^2 / b^2}{\omega_\alpha} \quad (5.50)$$

The ϵ 's are dimensionless gradient energy coefficients:

$$\epsilon = \frac{\epsilon_c^{2,\text{ref}}}{\epsilon_\phi^2}; \quad \epsilon^\alpha = \frac{\epsilon_\alpha^{2,\text{ref}}}{\epsilon_\phi^2}; \quad \epsilon^{\alpha\beta} = \frac{\epsilon_{\alpha\beta}^{2,\text{ref}}}{\epsilon_\phi^2} \quad (5.51)$$

Table 5.6 and 5.7 provide a summary of the parameters used in our model equations. In section 5.4 and 5.5, we perform numerical simulations of the dimensionless model equations.

Table 5.6: Summary of model parameters in total free energy

Variable	Definition	Unit
χ	molar fraction of methane	[1]
ϕ_α	volume fraction of phase α	[1]
T	temperature	$^\circ C$ or K
T_{ref}	reference temperature (for gradient energy)	$^\circ C$
F	total free energy	J
f_0	bulk free energy density	J/cm^3
f_α	Gibbs free energy density of phase α	J/cm^3
G_α	blending function for phase α	[1]
Ψ_c	compositional potential density	J/cm^3
Ψ_α	α phase potential	J/cm^3
ω_{mix}	characteristic mixing energy	J/cm^3
$\omega_{\alpha\beta}$	phase separation energy between α and β	J/cm^3
ϵ_ϕ^2	characteristic gradient energy coefficient	J/cm
$\epsilon_{\alpha\beta}^2$	gradient energy coefficient between phases	J/cm
ϵ_α^2	gradient energy coefficient of phase α	J/cm
ϵ_c^2	compositional gradient energy coefficient	J/cm
$\epsilon_{\alpha\beta}^{2,\text{ref}}$	reference gradient energy coefficient between phases	J/cm
$\epsilon_\alpha^{2,\text{ref}}$	reference gradient energy coefficient of phase α	J/cm
$\epsilon_c^{2,\text{ref}}$	reference compositional gradient energy coefficient	J/cm

Table 5.7: Summary of model parameters related to phase separation dynamics

Variable	Definition	Unit
$r_\chi = (D_c/\nu)/RT$	composition mobility	$\text{cm}^5/(J \cdot s)$
D_c	characteristic diffusion coefficient	cm^2/s
ν	molar density	mol/cm^3
R	Ideal gas constant	$J/(K \cdot \text{mol})$
$D(\{\phi_\alpha\})$	mixture diffusion coefficient	[1]
ρ	mixture density	g/cm^3
$r_\alpha = (D_c/\nu)/(b^2RT)$	phase mobility	$\text{cm}^3/(J \cdot s)$
b	characteristic length	cm
t_c	characteristic time	s
λ	Lagrange multiplier	1/s

5.4 Phase separation simulations above and below the triple point

In this section, we show three simulations that explore the phase separation dynamics at various regions of the $T - \chi$ phase diagram. We solve Eqs. (5.39)–(5.42) in a 2D circular geometry with a diameter of $L = 10$. The domain is discretized with a regular triangular mesh with a resolution $dx = L/128$. The system of four PDEs are solved implicitly in COMSOL. We use the Gibbs free energy proposed in Eq. (5.7)–(5.9), with the parameters given in Table 5.2, which produce the phase diagram in Fig. 5-10 and a triple point temperature of $T^T \approx 18.6^\circ\text{C}$. In addition to the free energy parameters in Table 5.2, we use the following values for our dimensionless model parameters:

Table 5.8: Summary of parameter values used in Sec. 5.4 and 5.5.

R_χ	R_g	R_l	R_s	Ma	Ch _g	Ch _l	Ch _s	Ch _{gl}	Ch _{sl}	Ch _{gs}
1/400	1/20	1/20	1/40	1/20	1/200	1/200	1/200	1/200	1/200	1/200
ϵ	ϵ^g	ϵ^l	ϵ^s	ϵ^{gl}	ϵ^{gs}	ϵ^{sl}	T_{ref}	D_g	D_l	D_s
20	5	5	5	6.67	6.67	6.67	5°C	1	1	1

5.4.1 Phase separation in vapor-liquid region

In the simulation shown in Fig. 5-14, we set $T = 20^\circ\text{C} > T^T$ and fill the domain with a randomly perturbed mixture with an average composition $\bar{\chi} = 0.4$, a point well within the vapor-liquid two-phase zone in the phase diagram (green circle in Fig. 5-10). In Fig. 5-14, we show the evolution dynamics of χ field illustrating the nucleation and coarsening of gas bubbles in liquid. At close to equilibrium, we measure the compositions inside the gas and liquid phase and find that $\bar{\chi}_g \approx 0.875$ and $\bar{\chi}_l \approx 0.08$. These equilibrium values match that predicted by the phase diagram calculated in Fig. 5-10.

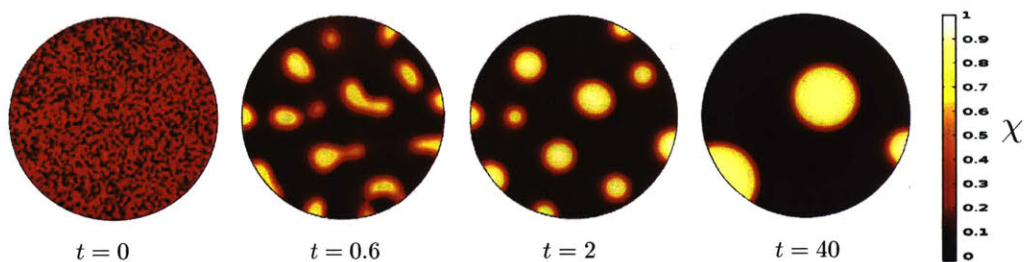


Figure 5-14: At $T = 20$, an initially perturbed mixture with an average molar fraction of $\bar{\chi} = 0.4$ phase separates into gas and liquid. At equilibrium, $\bar{\chi}_g \approx 0.875$ and $\bar{\chi}_l \approx 0.08$. The snapshots are shown at $t = 0, 0.6, 2$ and 40 . These equilibrium values match that predicted by the phase diagram calculated in Fig. 5-10.

5.4.2 Phase separation in hydrate-forming region

In the next two simulations shown in Fig. 5-15- Fig. 5-16, we set $T = 5^\circ\text{C} < T^T$, meaning that hydrate can readily form. We describe the results of the simulations by plotting time snapshots of ϕ_s (top row) and χ (bottom row). We use results of ϕ_g and ϕ_l to infer local phase compositions in our discussion but do not show their corresponding snapshots here. The colormap for χ in Fig. 5-16 (and Fig. 5-18 in Sec. 5.5) are chosen to emphasize the details between $\chi \in [0, 0.2]$, where the hydrate and liquid phases reside.

Equilibrium in H-V region

In the simulation shown in Fig. 5-15, we start with a domain occupied by three gas bubbles with composition $\chi_g = 0.9$ and an ambient liquid with $\chi_l = 0.01$; no hydrate is present initially. The domain-average molar fraction is $\bar{\chi} = 0.238$. This puts the system in a region of the phase diagram where one expects a gas-hydrate coexistence at equilibrium (green star in Fig. 5-10). Indeed, Fig. 5-15 illustrates the dynamics of how a gas-liquid domain transforms into a gas-hydrate domain via the directional solidification of hydrate into the liquid phase. The snapshot at $t = 0.6$ shows that hydrate initially grows at the gas-liquid interface, however, at a small expense of methane stored in the gas bubbles. This is evident by the shrinkage in bubble sizes between $t = 0$ and $t = 0.6$, where all bubbles dissolve a small amount to replenish

the liquid, which forms hydrate later. Note that such transfer of methane from gas to liquid phase is conducted through the mass diffusion within the hydrate layer. From $t = 2$ to $t = 10$, the liquid phase has become completely converted into hydrate; the gas-hydrate mixture then undergoes the Ostwald ripening process, where methane bubbles coarsen through the ambient hydrate phase (Ostwald ripening).

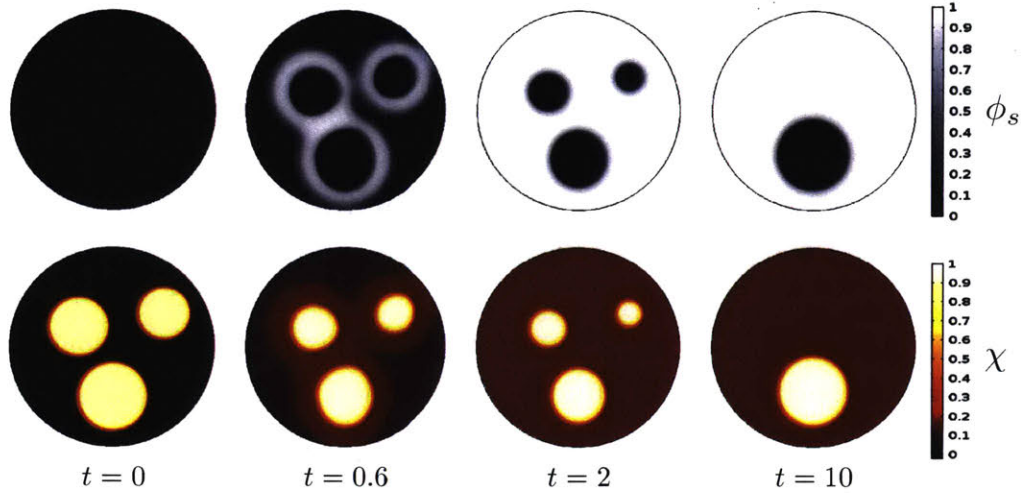


Figure 5-15: At $T = 5$, a temperature when hydrate can form, the domain is initially occupied by three gas bubbles with $\chi_g = 0.9$ surrounded by liquid with $\chi_l = 0.01$; no hydrate is present initially. The average molar fraction in the entire domain is $\bar{\chi} = 0.238$. As the mixture evolves, hydrate first forms at the gas-liquid interface, then hydrate preferentially grow into the liquid phase, which has an elevated χ due to some initial gas dissolution. At equilibrium, there are only gas and hydrate present and $\bar{\chi}_g \approx 0.968$ and $\bar{\chi}_s \approx 0.149$. These equilibrium values match that predicted by the phase diagram calculated in Fig. 5-2.

Equilibrium in L_w -H region

In the simulation shown in Fig. 5-16, we initialize the domain with a single gas bubble with $\chi_g = 0.9$ and an ambient liquid with $\chi_l = 0.01$; no hydrate is present initially. The domain-average molar fraction is $\bar{\chi} = 0.066$, which puts the system in a region of the phase diagram where a liquid-hydrate coexistence is expected at equilibrium (green square in Fig. 5-10). The dynamics towards this equilibrium, as illustrated in Fig. 5-16, starts with hydrate formation on the gas-liquid interface ($t = 0.6$). Similar

to the second simulation, here the gas bubble shrinks in order to replenish dissolved methane level in the liquid and to form hydrate. This process eventually leads to the complete consumption of this gas bubble ($t = 2$), leaving the domain with only liquid and hydrate. From $t = 2$ to $t = 10$, hydrate continues to form into the liquid phase until the two phases reach a thermodynamic equilibrium.

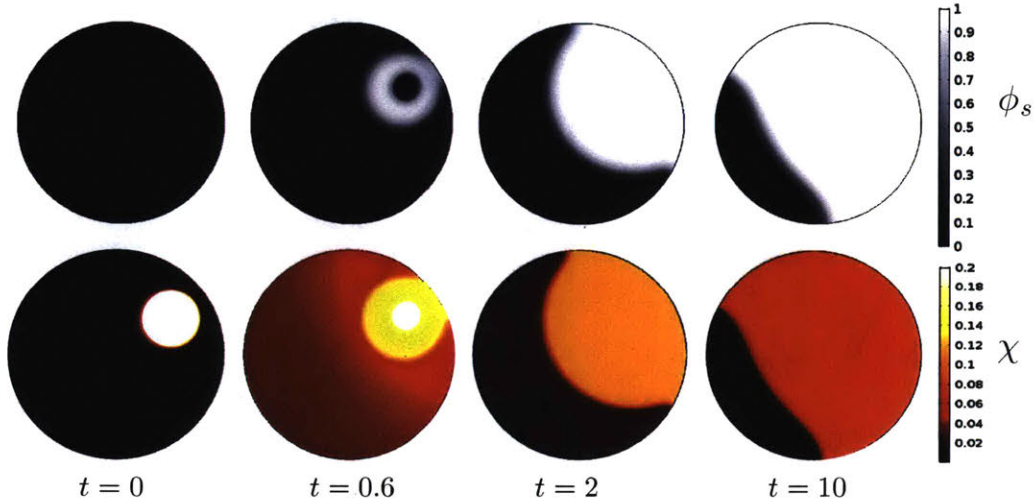


Figure 5-16: At $T = 5$, a temperature when hydrate can form, the domain is initially occupied by a single gas bubbles with $\chi_g = 0.9$ surrounded by liquid with $\chi_l = 0.01$; no hydrate is present initially. The average molar fraction in the entire domain is $\bar{\chi} = 0.066$. As the mixture evolves, hydrate first forms at the gas-liquid interface, then hydrate preferentially grow into the gas phase and eventually replaces the gas bubble completely. At equilibrium, there are only liquid and hydrate present with $\bar{\chi}_l \approx 0.0088$ and $\bar{\chi}_s \approx 0.079$. These equilibrium values match that predicted by the phase diagram calculated in Fig. 5-2.

5.4.3 Phase separation dynamics in a ternary diagram

In Fig. 5-17, we visualize the phase separation processes shown in Fig. 5-15 and 5-16 in terms of temporal trajectories in the ternary diagram. Trajectory 1 in Fig. 5-17 corresponds to the simulation in Fig. 5-15, where the system starts with approximately 0.25/0.75 of V/ L_w and ends at 0.12/0.88 of V/H. Trajectory 2 in Fig. 5-17 corresponds to the simulation in Fig. 5-16, where the system starts with approximately 0.08/0.92 of V/ L_w and ends at 0.2/0.8 of L_w /H.

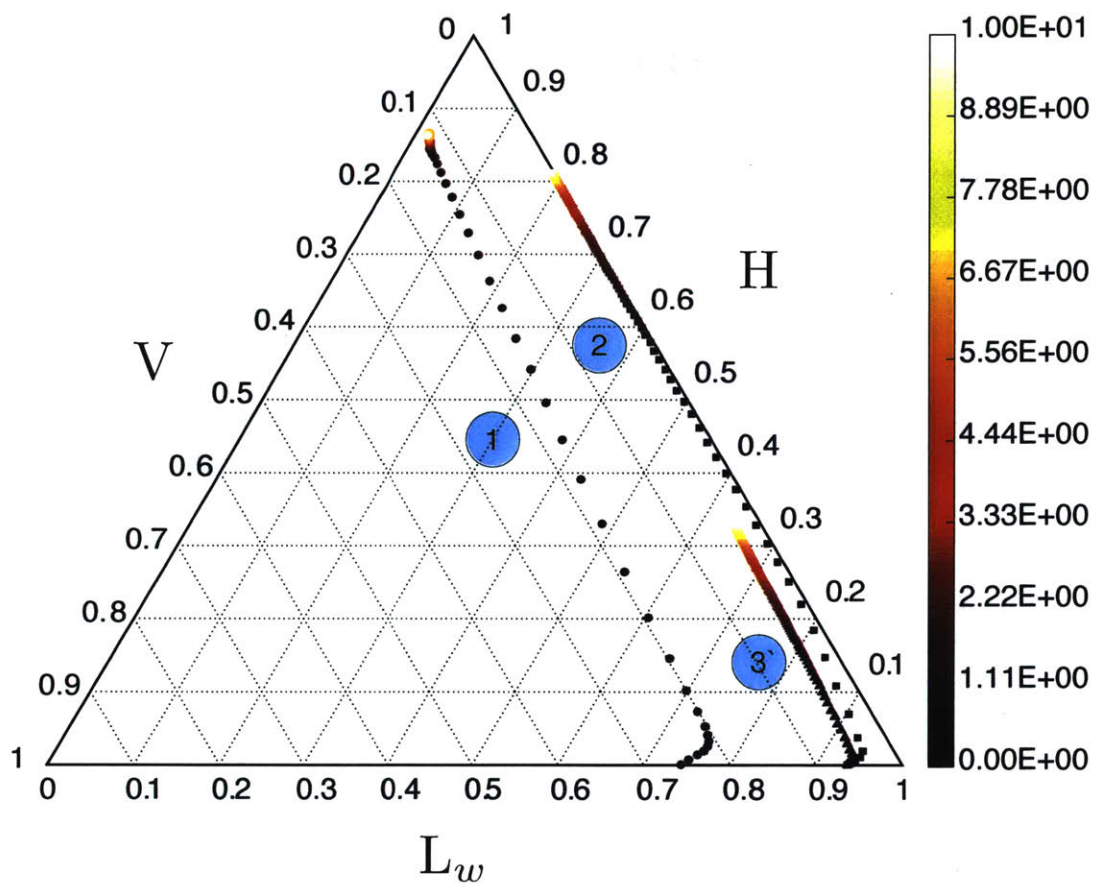


Figure 5-17: Phase separation dynamics drawn in a ternary diagram. The colormap references time. Trajectory 1 corresponds to simulation shown in Fig. 5-15 or the green star in Fig. 5-10. Trajectory 2 corresponds to simulation shown in Fig. 5-16 or the green square in Fig. 5-10. Trajectory 3 corresponds to simulation shown in Fig. 5-18, where diffusion inside hydrate is much slower compared to that in Fig. 5-16. Note trajectory 2 and 3 start at the same location but terminate at different points.

5.5 Growth kinetics of hydrate on a gas-liquid interface

In the previous section, we demonstrate that our proposed model and simulations can correctly predict the equilibrium phase partitioning of methane-water system above and below the triple point temperature. Specifically, our dynamic phase separation simulations arrive at the correct equilibrium phase coexistence as well as the phase compositions indicated by the T - χ phase diagram. In this section, we turn our focus to the nonequilibrium dynamics of phase separation. First, we use our model to explore the effect of very slow mass diffusion within the hydrate layer on the phase separation problem (Sec. 5.5.1). Second, we address how the aqueous phase saturation can impact the effective growth rate of hydrate film on a gas-liquid interface (Sec. 5.5.3).

5.5.1 Slow diffusion within hydrate layer leads to prolonged three-phase coexistence

In the simulations performed in Sec. 5.4, we assume that the rate of methane diffusion is the same in all three phases. In practice, however, methane diffuses at rates that are orders of magnitude different within each phase. Diffusion coefficient is around $0.167 \text{ cm}^2/\text{s}$ in gas, $2 \times 10^{-5} \text{ cm}^2/\text{s}$ in water (Witherspoon and Saraf, 1965) and $7 \times 10^{-11} \text{ cm}^2/\text{s}$ in hydrate (Peters et al., 2008).

In this section, we adopt different diffusion coefficients for each phase to emulate the real system where methane would diffuse slowly in liquid and much slower in hydrate. Specifically, we use the following values, where the magnitude differences are smaller than that suggested by (Witherspoon and Saraf, 1965; Peters et al., 2008):

$$D_l = 0.01; \quad D_s = 10^{-5} \quad D_g = 1$$

We probe the effect of diffusion kinetics on the growth pattern by repeating the third simulation (Fig. 5-16) with the updated D_α . The results, shown in Fig. 5-18, illustrate a drastically different pattern of growth. As a result of very slow diffusion

inside the hydrate layer, we observe that the coexistence of gas bubble, hydrate and liquid persists till at least $t = 10$, much longer than that observed in Fig. 5-16, where the gas phase disappears by $t = 2$. The slow diffusion inside hydrate also gives rise to a two-layer structure in χ inside the hydrate layer ($t = 2$ and $t = 10$). Specifically, the yellow colored sub layer has an average composition of $\chi \approx 0.144$, which is the predicted equilibrium hydrate composition under hydrate-gas coexistence (Fig. 5-10). The orange colored sub layer has an average composition of $\chi \approx 0.08$, which is the predicted equilibrium hydrate composition under hydrate-liquid coexistence (Fig. 5-10). Such two-layer structure is first observed experimentally by (Huo et al., 2003), where they refer to the yellow-colored hydrate layer (higher methane concentration) as *interfacial* hydrate and the orange-colored hydrate layer (lower methane concentration) as *dendritic* hydrate.

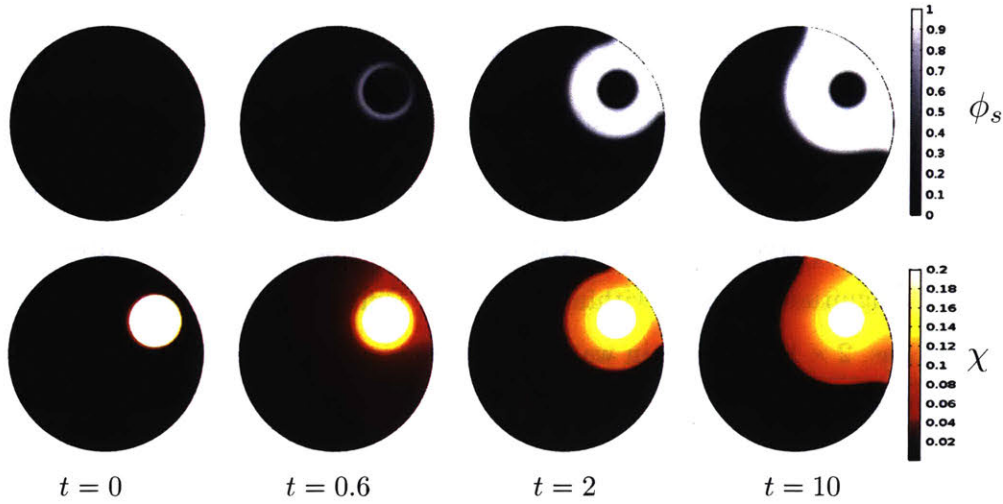


Figure 5-18: This simulation uses the same parameters as in Fig. 5-16, but diffusion coefficients are assigned differently. In Fig. 5-16, $D_l = D_s = D_g = 1$. In this simulation, $D_l = 0.1$, $D_s = 10^{-5}$, $D_g = 1$.

In the long term, the composition within the hydrate layer should become spatially uniform through two parallel processes: (1) the inner gas phase is converted to hydrate and the excess methane needs to be transferred towards the aqueous phase to fuel *dendritic* hydrate formation (2) water from the outer aqueous phase needs to be transported towards the inner gas phase to support *interfacial* hydrate formation.

Both processes are limited by diffusion, which is very small inside hydrate. As a result, the system appears to be in a steady-state even though thermodynamic equilibrium is not reached.

Similar to previous two simulations, we can visualize the phase separation trajectory in the ternary diagram for the current simulation. Trajectory 3 in Fig. 5-17 corresponds to the simulation in Fig. 5-18, where the system starts at the same location as trajectory 2 (approximately 0.25/0.75 of V/L_w). Even though both simulations start at the same point, because of the diffusion-limited transport within the hydrate layer, trajectory 3 and 2 end at different locations. Specifically trajectory 3 becomes stuck at a point where all three phases exist: 0.64/0.03/0.33 of $L_w/V/H$, while trajectory 2 ends at a two-phase coexistence point: 0.12/0.88 of V/H .

5.5.2 Implications for the fate of hydrate-crusted bubbles

Given that methane diffusion coefficient inside hydrate is in the order of 10^{-11} cm^2/s , it takes about 4 years to diffuse through 1mm of hydrate layer, a time scale orders of magnitude longer than advective time scale in water column. Thus, a diffusion-limited transport of methane within the hydrate layer significantly hinders the growth of hydrate on a gas-liquid interface and prevents the system to reach true thermodynamic equilibrium. At observable time scale of laboratory experiments such as the ones in (Huo et al., 2003; Taylor et al., 2007; Chen et al., 2014, 2016; Warzinski et al., 2014), the prolonged coexistence of hydrate, gas and liquid is likely caused by this effect, and as a consequence, one would need to consider nonequilibrium thermodynamics to model and understand experimental observations.

This effect also has significant implications in understanding methane transport via a hydrate-crusted bubble in the water column. It has been conjectured that a hydrate layer on the bubble acts as a shield against methane diffusion towards water. Our physics based modeling has verified that this shielding effect is caused by a very slow diffusion rate within the hydrate layer, which effectively slows down the mass transfer rate from methane bubble to water column. In future work, we will quantify how much does the formation of a hydrate layer modify the effective mass transfer

rate at the bubble-water interface. A quantitative understanding of the effective mass transfer rate is valuable in improving upscaled bubble plume models used to predict fate of bubble plumes with hydrate crusts (Clift et al., 1978; Wang et al., 2016).

5.5.3 The rate of hydrate film growth: diffusion-limited and kinetically-controlled regimes

The formation and growth of hydrate on a gas-liquid interface is a complex process that may be controlled by kinetic, heat and mass transfer limitations (Sloan and Koh, 2008). For instance, hydrate nucleation rate and film growth rate increases with aqueous methane concentration as well as degree of subcooling (Saito et al., 2010; Walsh et al., 2011). In Sec. 5.5.1, we discuss how slow diffusion within hydrate layer, a mass transfer limitation, can reduce hydrate growth rate and result in prolonged period of three-phase coexistence. Because of its complexity, there has been numerous attempts in creating parameterized models to describe the growth kinetics of hydrate films on a gas-liquid interface (Mori and Mochizuki, 1998, 2000; Mochizuki and Mori, 2000; Abay and Svartaas, 2011; Meindinyo and Svartaas, 2016). At the heart of this challenge is to describe the macroscopic film growth rate, which decreases to zero over time and depends on local aqueous methane saturation and local temperature (non constant due to heat generation). In this section, we use our proposed model to explore a quantitative understanding on how aqueous methane saturation can change the hydrate film growth rate. We assume a constant temperature and do not consider the thermal effect on hydrate growth rate.

We perform a series of 1D film growth simulations in a domain of length $L = 50$ (discretized with $N = 1280$ points). We use the parameters in Table 5.1 to describe our free energies and set the temperature to be $T = 4^\circ C$. The free energies curves along with the common tangent constructions are shown in Fig. 5-8. Specifically, the system has two equilibrium scenarios:

1. At liquid-hydrate equilibrium: $\chi_l^{\text{eq}} \approx 0.03$ and $\chi_s^{\text{eq}} \approx 0.141$;
2. At hydrate-gas equilibrium: $\chi_g^{\text{eq}} \approx 0.96$ and $\chi_s^{\text{eq}} \approx 0.146$

In this 1D domain, we place a gas bubble of composition $\chi_g = 0.88$ in a liquid phase of initial composition $\chi_{l0} = 0.01, 0.02, 0.03, 0.04$ or 0.06 (different χ_{l0} for each simulation; Fig. 5-19 top plots initial conditions). The initial aqueous phase methane

concentrations are chosen so that we can sample methane concentration below, at and above the aqueous solubility in the presence of hydrate ($\chi_t^{\text{eq}} \approx 0.03$, see Fig. 5-20a). For all five simulations, the domain-averaged composition is within the H-V region, meaning the system should evolve towards H-V coexistence at equilibrium (but we do not simulate the system to equilibrium and only focus on the film growth regime). We use the following diffusion coefficients:

$$D_l = 0.1; \quad D_s = 10^{-5} \quad D_g = 1.$$

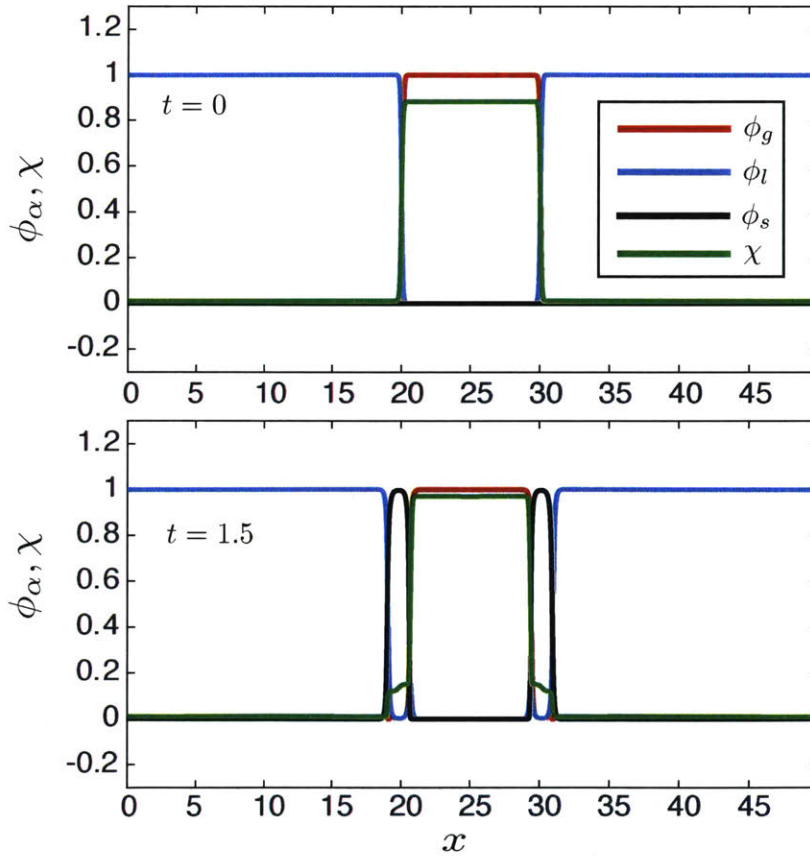


Figure 5-19: Sample profiles of ϕ_g (red), ϕ_l (blue), ϕ_s (black) and χ (green) of a series of simulations performed in Sec. 5.5.3. (Top): initial condition; (bottom): end of simulation at $t = 1.5$.

In Fig. 5-19 bottom, we show a sample snapshot of the 1D profiles at the end of our simulation ($t = 1.5$), where a hydrate layer (black line) has formed at the gas-liquid

interface. We measure the domain averaged hydrate volume fraction $\overline{\phi_s}$ as a function of time for all simulations (Fig. 5-20b). At a first glance, the film growth curves in Fig. 5-20b show well-understood regimes: after a brief period of film nucleation (linear growth), the asymptotic growth regime starts, where the growth rate decreases with time and eventually becomes zero (not shown here). In Fig. 5-21, we re-plot the same data from Fig. 5-20b in log-log scale. Again, the initial t^1 scaling for all simulations correspond to the film nucleation regime. During the asymptotic growth regime, we observe that the growth kinetics is mostly diffusion-limited ($t^{1/2}$ scaling) if $\chi_{l0} < \chi_l^{\text{eq}}$ and (thermodynamic) kinetically-limited (t^k with $k > 1/2$) if $\chi_{l0} \geq \chi_l^{\text{eq}}$.

5.5.4 Implications for predicting occurrence of hydrate-crusted bubbles in natural water columns

These results implicate that the growth kinetics of hydrate film on a gas-liquid interface depend significantly on the aqueous phase methane saturation. If the liquid is under-saturated in methane, hydrate film growth is likely to exhibit diffusion-limited kinetics, where the hydrate formation is limited by the supply of methane at the solidification front. On the other hand, if the aqueous methane saturation is at or above the solubility level, the film growth kinetics could exhibit a super-diffusive (but sub-linear) regime, where hydrate thickening is limited by the kinetics of thermodynamic phase transition. Our simulations have also shown that hydrate film can readily form on a gas-liquid interface even if the liquid phase is under-saturated in methane. While this has been demonstrated experimentally by (Chen et al., 2014, 2016), the work by (Warzinski et al., 2014) shows that a fully saturated water column is required to observe hydrate formation on a methane bubble in their experimental setup. Here, we agree with the previous conclusion by (Chen et al., 2014, 2016), that aqueous saturation is not a required condition for hydrate film growth, *given* that other thermodynamic forcing such as pressure and subcooling can facilitate hydrate formation. In the context of a hydrate-crusted bubble rising in the water column, this confirms with a long standing speculation that once bubble escapes the seafloor, the

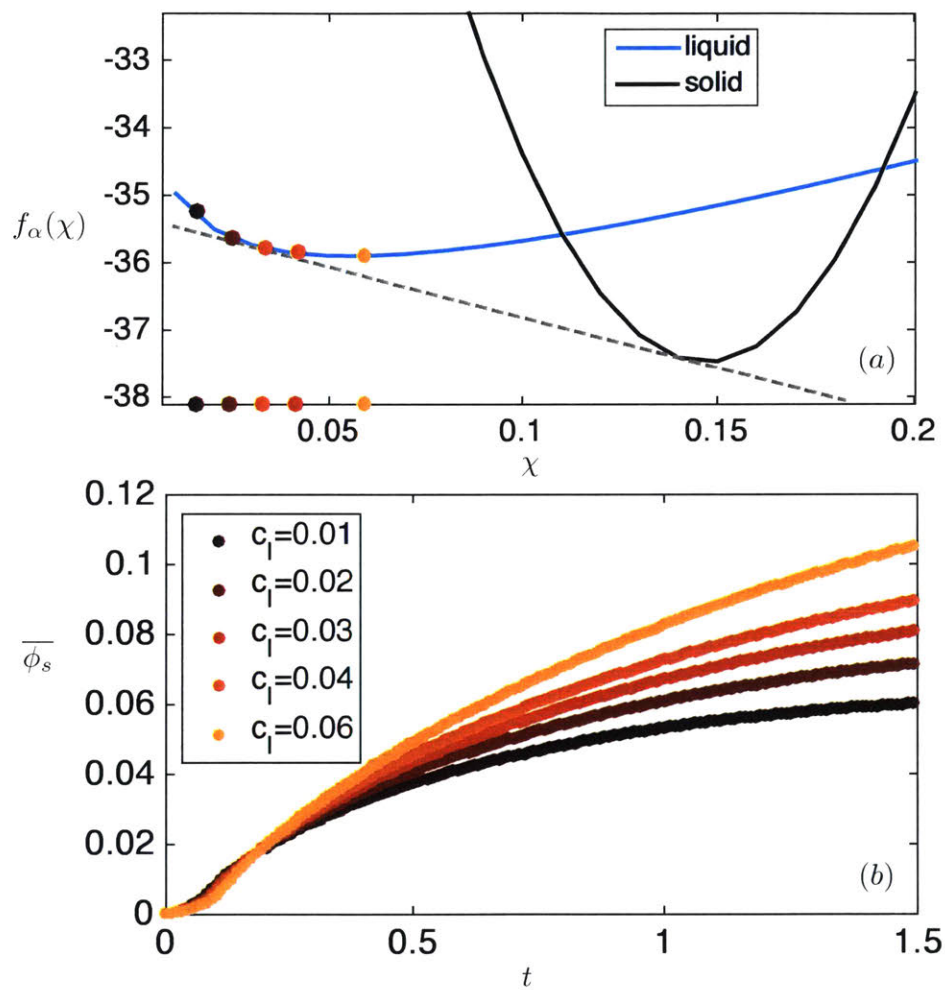


Figure 5-20: (a) Zoomed-in view of the free energy curves shown in Fig. 5-8. Here we focus on the L_w -H region. The colored dots mark the liquid phase compositions for each simulation. Note that $\chi_l^{\text{eq}} \approx 0.03$ is the 3rd dot from left. (b) The corresponding hydrate film thickness (here calculated as the domain averaged hydrate volume fraction $\overline{\phi}_s$) as a function of time for all simulations.

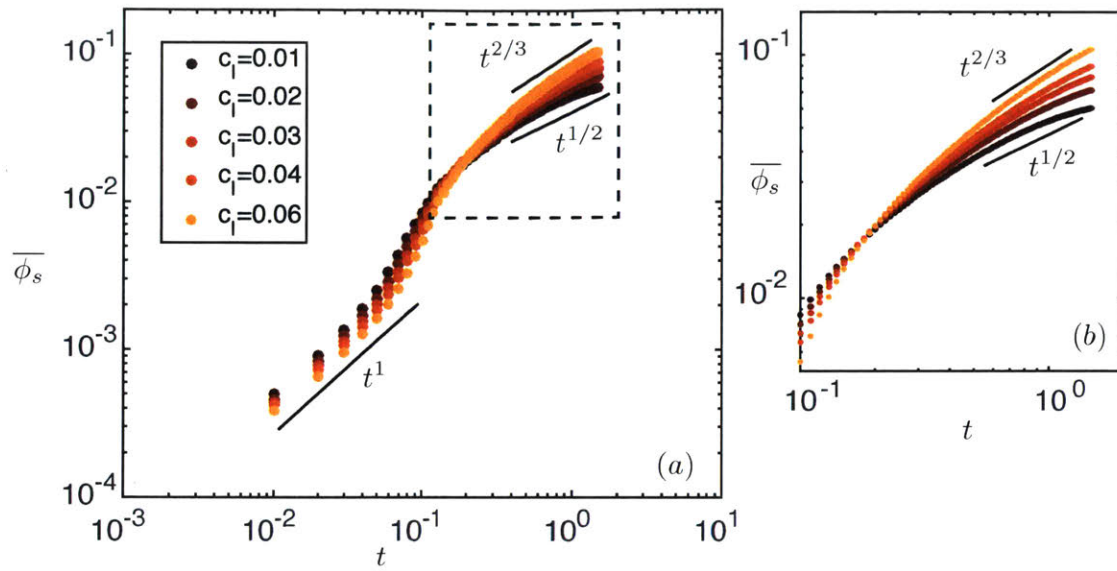


Figure 5-21: (a): $\bar{\phi}_s$ vs. t in log-log scale. (b) enlarged view of the dashed box in (a).

ambient water can be below methane solubility and still support hydrate formation at the gas-liquid interface.

5.6 Compressibility of mixtures

In this section, we introduce fluid compressibility into the model Eq. (5.30) and Eq. (5.34) in order to capture the volumetric expansion of the gas phase under depressurization (Sec. 5.1.2). The assumption of equal and constant densities of each phase no longer holds. We prescribe the high compressibility in gas phase using a pressure-dependent density:

$$\rho_g = \frac{p}{z_g(p)RT}, \quad (5.52)$$

where $z_g(p)$ is the compressibility factor of gas that is also a function of pressure. For a natural gas mixture in the temperature (277K- 297K) and pressure range (less than 50MPa or 5000 meters of water) we investigate here, z_g may exhibit non-monotonic behavior with p (Dranchuk and Abou-Kassem, 1975); however, the variation in z_g is small compared to the average value z_g within the investigated pressure range. Thus, we approximate the compressibility factor with an average value and independent of pressure:

$$z_g(p) = 0.98. \quad (5.53)$$

The liquid phase is assumed to be weakly compressible, with density changing only slightly with pressure:

$$\rho_l = \frac{\rho_{l0}}{1 - \frac{p - p_0}{z_l}}, \quad (5.54)$$

where z_l is a constant liquid compressibility factor (bulk modulus of liquid). For water, $z_l = 2150\text{MPa}$; therefore, for the range of pressure we investigate (less than 50MPa or 5000 meters of water), the density of water does not change appreciably with pressure. Last, we assume a constant density for the hydrate phase:

$$\rho_s = \rho_{s0}. \quad (5.55)$$

In Fig. 5-22, we plot the density of the three phases as a function of pressure up to $p = 7.5\text{MPa}$. The density of hydrate is approximated with that of ice. The plots in

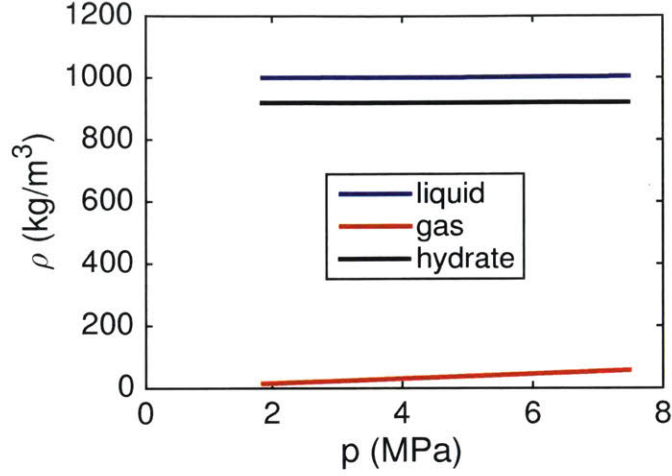


Figure 5-22: Density of methane gas, liquid water and hydrate as a function of pressure.

Fig. 5-22 show that the density dependence in pressure is almost linear for all phases. Therefore, here we simplify our description of phase compressibility by imposing a linear pressure dependence in density for all three phases:

$$\rho_{\alpha} = \rho_{\alpha 0} + c_i^{\alpha} p \quad (5.56)$$

Finally, it is convenient for modeling to define a mixture density, which is the mass per volume at a given point in the domain. Here we describe the mixture density as a ϕ_{α} -weighted average:

$$\rho = \rho_l \phi_l + \rho_g \phi_g + \rho_s \phi_s. \quad (5.57)$$

5.6.1 Three-phase mixture velocity under Darcy's law

Instead of identifying and tracking velocities within each phase, we assume a mixture velocity (at each point in the domain) that obeys Darcy's law:

$$\mathbf{u}(x, y) = \frac{-k}{\mu(\phi_g, \phi_l, \phi_s)} \nabla p, \quad (5.58)$$

where k is permeability. We model all three phases as fluid with a certain viscosity. Specifically, we assume that hydrate phase is the most viscous and gas the least viscous phase. We assume that viscosities of all phases are independent of composition and normalize the values by the liquid water viscosity μ_{water} so that:

$$\mu_g = 1/M, \quad \mu_l = 1, \quad \mu_s = M,$$

where M is the viscosity contrast: $M = \mu_s/\mu_l$. We define a mixture viscosity by blending the three viscosities by a phase-weighted average:

$$\mu(\{\phi_\alpha\}) = \mu_{\text{water}}(\mu_g\phi_g + \mu_l\phi_l + \mu_s\phi_s), \quad (5.59)$$

where μ_{water} is the viscosity of water. This blending formulation is consistent with what is done to diffusion coefficients (Eq. (5.32))

5.6.2 Evolution equations with advection

We update the system of equations in Eqs. (5.30) and Eq. (5.34) to include the effect of density change and fluid flow. The total mass of the mixture (methane plus water) should be conserved:

$$\frac{\partial \rho}{\partial t} + \nabla \cdot (\rho \mathbf{u}) = 0. \quad (5.60)$$

Additionally, we have the conservation of mass of methane considering advection:

$$\frac{\partial \rho \chi}{\partial t} + \nabla \cdot (\rho \chi \mathbf{u}) - r_\chi \nabla \cdot (D(\{\phi_\alpha\}) \rho \nabla \Psi_c) = 0. \quad (5.61)$$

Lastly, we complete the system with a non-conserved Allen-Cahn evolution equation for ϕ_g and ϕ_s in an advective form:

$$\frac{\partial \phi_\alpha}{\partial t} + \mathbf{u} \cdot \nabla \phi_\alpha + r_\phi \Psi_\alpha = 0. \quad (5.62)$$

5.6.3 Discretization of pressure equation

We combine the mixture Darcy velocity, Eq. (5.58), and mixture density definition, Eq. (5.57), into the total mass conservation (Eq. (5.60)) to arrive at a time-dependent parabolic pressure equation (Eq. (5.64)). Given

$$\rho = \rho_l \phi_l + \rho_g \phi_g + \rho_s \phi_s,$$

and

$$\rho_\alpha = \rho_{\alpha 0} + c_i^\alpha p,$$

the time derivative of ρ can be written as:

$$\begin{aligned} \frac{\partial \rho}{\partial t} &= c_{lg} \phi_g \frac{\partial p}{\partial t} + \rho_g \frac{\partial \phi_g}{\partial t} + c_{ll} \phi_l \frac{\partial p}{\partial t} + \rho_l \frac{\partial \phi_l}{\partial t} + c_{ls} \phi_s \frac{\partial p}{\partial t} + \rho_s \frac{\partial \phi_s}{\partial t} \\ &= (c_{lg} \phi_g + c_{ll} \phi_l + c_{ls} \phi_s) \frac{\partial p}{\partial t} + \rho_g \frac{\partial \phi_g}{\partial t} + \rho_l \frac{\partial \phi_l}{\partial t} + \rho_s \frac{\partial \phi_s}{\partial t} \\ &= c_i^* \frac{\partial p}{\partial t} + \rho_g \frac{\partial \phi_g}{\partial t} + \rho_l \frac{\partial \phi_l}{\partial t} + \rho_s \frac{\partial \phi_s}{\partial t}, \end{aligned}$$

where we define the *mixture compressibility* as:

$$c_i^* = c_{lg} \phi_g + c_{ll} \phi_l + c_{ls} \phi_s \quad (5.63)$$

Now apply the definition above to the pressure equation to arrive at:

$$c_i^* \frac{\partial p}{\partial t} + \nabla \cdot \left(-\rho \frac{k}{\mu(\phi_g, \phi_l, \phi_s)} \nabla p \right) = -\rho_g \frac{\partial \phi_g}{\partial t} - \rho_l \frac{\partial \phi_l}{\partial t} - \rho_s \frac{\partial \phi_s}{\partial t}. \quad (5.64)$$

5.6.4 Example in 1D: hydrate growth on an expanding gas bubble

In this section, we test the compressible version of our model in 1D. The simulation starts with a hydrate-crust gas bubble surrounded by a liquid with some level of dissolved methane ($\chi_l \approx 0.14$). We adopt the Gibbs free energy described in Eqs. (5.7)-(5.9). Given the domain-averaged composition of $\bar{\chi} = 0.27$, the system

should arrive at a liquid-hydrate coexistence at equilibrium, meaning that the gas bubble will eventually disappear. However, we slow down the consumption of the gas bubble by adopting realistic diffusion coefficients as described in Sec. 5.5; this allows us to preserve the three-phase coexistence configuration, as in the case of hydrate-crusted gas bubble, throughout the simulation. The initial pressure and density are uniform: $p_0 = 2$ and $\rho = 1$ across all phases. A pressure-dependent density is prescribed for each phase:

$$\rho_g = 0 + 0.5p; \quad \rho_l = 0.98 + 0.01p; \quad \rho_s = 0.98 + 0.01p.$$

The domain is then depressurized through the left and right boundaries at a constant rate of 0.0001 per time step for 8000 time steps; the pressure is then fixed at $p(x = 0, 1) = 1.2$ until time step 20000 to give the domain enough time to equilibrate.

Numerical methods

The simulation is implemented in MATLAB, where we solve the five PDEs described in Eqs. (5.60)-(5.62) using an IMPES scheme (Implicit Pressure Explicit Saturation). At each time step, the pressure is solved implicitly and the phase and mass fractions are evolved explicitly. We discretize Eq. (5.64) in time as the following:

$$\frac{c_t^{*n}}{\Delta t}(p^{n+1} - p^n) + \rho_g^n \frac{\partial \phi_g}{\partial t}|^n + \rho_l^n \frac{\partial \phi_l}{\partial t}|^n + \rho_s^n \frac{\partial \phi_s}{\partial t}|^n + \nabla \cdot \left(-\rho^n \frac{k}{\mu(\phi_g^n, \phi_s^n, \phi_l^n)} \nabla p^{n+1} \right) = 0;$$

or after rearrangement, becomes:

$$\frac{c_t^{*n}}{\Delta t} p^{n+1} + \nabla \cdot \left(-\rho^n \frac{k}{\mu(\phi_g^n, \phi_s^n, \phi_l^n)} \nabla p^{n+1} \right) = \frac{c_t^{*n}}{\Delta t} p^n - \left(\rho_g^n \frac{\partial \phi_g}{\partial t}|^n + \rho_l^n \frac{\partial \phi_l}{\partial t}|^n + \rho_s^n \frac{\partial \phi_s}{\partial t}|^n \right). \quad (5.65)$$

Step 0: At the current time step, we have information on the following: ϕ^n , χ^n , p^n , u_x^n , ρ^n , c_t^{*n} , $\frac{\partial \phi^n}{\partial t}$. Additionally, we define the methane mass density as $c^n = \rho^n \chi^n$.

Step 1: Update the pressure at the boundary to simulate depressurization:

$$p(x = 0) = p_0 - k_p t; \quad p(x = L) = p_0 - k_p t$$

Step 2: Solve Eq. (5.65) with the updated boundary condition for pressure at the next time step: p^{n+1} and then compute

$$u_x^{n+1} = -\frac{k}{\mu(\phi^n)} \frac{\partial p^{n+1}}{\partial x}.$$

Step 3: Using semi-implicit method to solve for ϕ^{n+1} using Eq. (??):

$$\phi^{n+1} + (\epsilon r_\phi \Delta t) \frac{\partial^2 \phi^{n+1}}{\partial x^2} = \phi^n + (\epsilon r_\phi \Delta t) \frac{\partial^2 \phi^n}{\partial x^2} + \Delta t \left(-u_x^n \frac{\partial(\phi^n)}{\partial x} - r_\phi \frac{\partial}{\partial x} \left(\frac{\delta F^n}{\delta \phi} \right) \right) \quad (5.66)$$

Step 4: Compute $\frac{\partial \phi^n}{\partial t}$ (used in the next iteration of pressure solver):

$$\frac{d\phi^n}{dt} = (\phi^{n+1} - \phi^n) / \Delta t. \quad (5.67)$$

Step 5: Using semi-implicit method to solve for $c^{n+1} = \rho^{n+1} \chi^{n+1}$ using Eq. (??):

$$c^{n+1} + (\epsilon r_\chi \Delta t) \frac{\partial^4 c^{n+1}}{\partial x^4} = c^n + (\epsilon r_\chi \Delta t) \frac{\partial^4 c^n}{\partial x^4} + \Delta t \left[-\frac{\partial}{\partial x} (u_x^n c^n) + r_\chi \frac{\partial}{\partial x} \left(\rho^n \frac{\partial}{\partial x} \left(\frac{\delta F^n}{\delta \chi} \right) \right) \right] \quad (5.68)$$

Step 6: Compute χ^{n+1} :

$$\chi^{n+1} = c^{n+1} / \rho^n \quad (5.69)$$

Step 7: Update gas, liquid and mixture density with the new pressure:

$$\rho_g^{n+1} = \rho_{g0} + c_i^g p^{n+1} \quad (5.70)$$

$$\rho_l^{n+1} = \rho_{l0} + c_i^l p^{n+1} \quad (5.71)$$

$$\rho^{n+1} = \rho_l^{n+1} (1 - \phi^{n+1}) + \rho_g^{n+1} \phi^{n+1} \quad (5.72)$$

5.6.5 Results and discussion

In Fig. 5-23, we plot snapshots of the simulation in three key variables: χ , ϕ_s and ρ . The density is initially uniform across all phases ($t = 0$) and starts to decrease inside the gas phase as a result of pressure decrease across the domain. We plot the corresponding pressure distribution and the generated Darcy velocity (u_x) in Fig. 5-24 and 5-25. The constant-rate depressurization lasts until time step 8000 ($t = 2000, 7500$ in Fig. 5-23-5-25), during which time the gas bubble has significantly expanded (grey dashed box indicates the initial gas bubble), accompanied by the instantaneous growth of hydrate on the moving interface. The hydrate layer also continues to thicken during this process. The high compressibility of the gas phase allows the pressure inside to build up, which creates a pressure gradient across the interface and creates high velocity locally (Fig. 5-25). This pressure gradient drives the expansion of gas bubble against the more viscous hydrate and liquid surrounding it, allowing partial relief of the pressure accumulation inside the gas phase (Fig. 5-24 $t = 2000, 7500$). After 8000 time steps, we stop the depressurization and allow the system to relax. During the relaxation process, the gas bubble continues to expand for some time before the movement stops ($u_x = 0$ as shown in Fig. 5-25 at $t = 20000$).

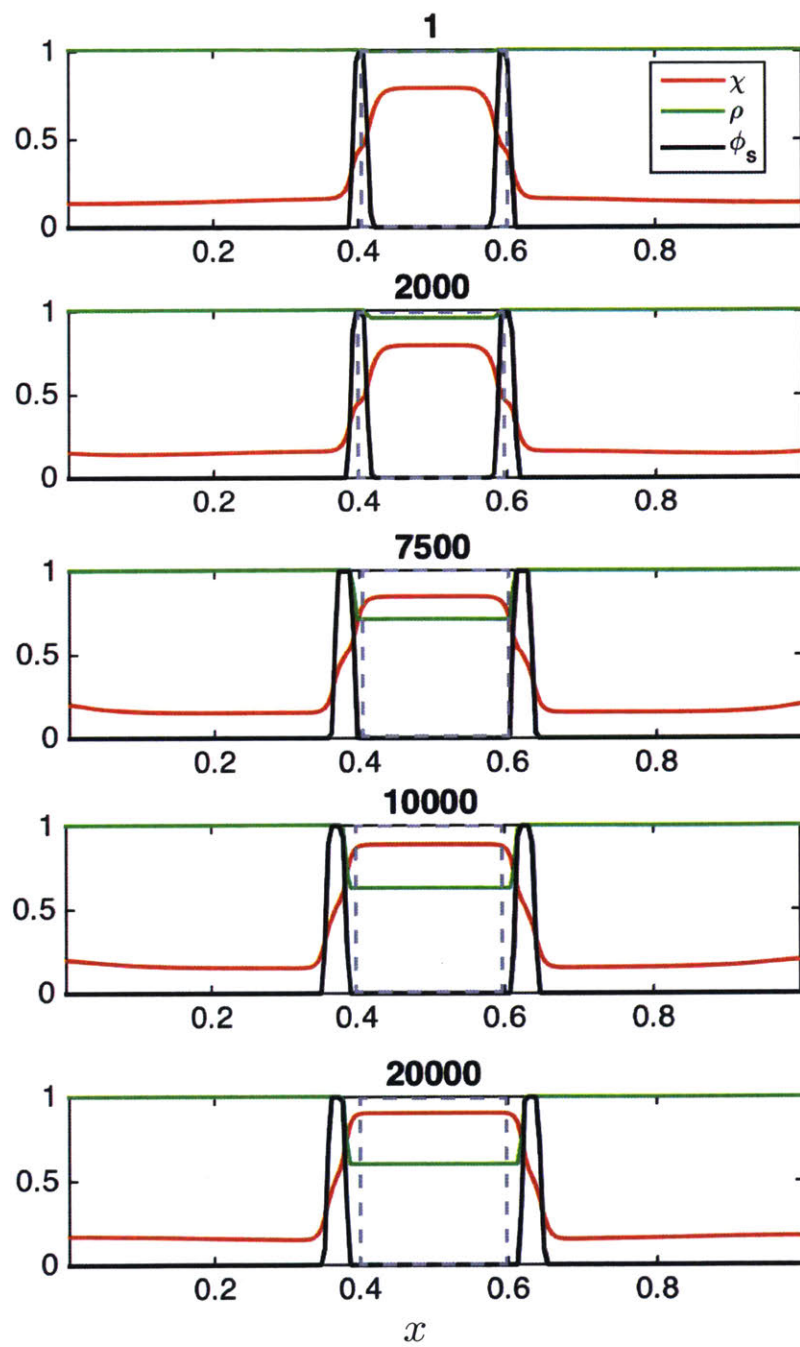


Figure 5-23: Snapshots of χ , ϕ_s and ρ describing the details of an expanding hydrate-crusted bubble.

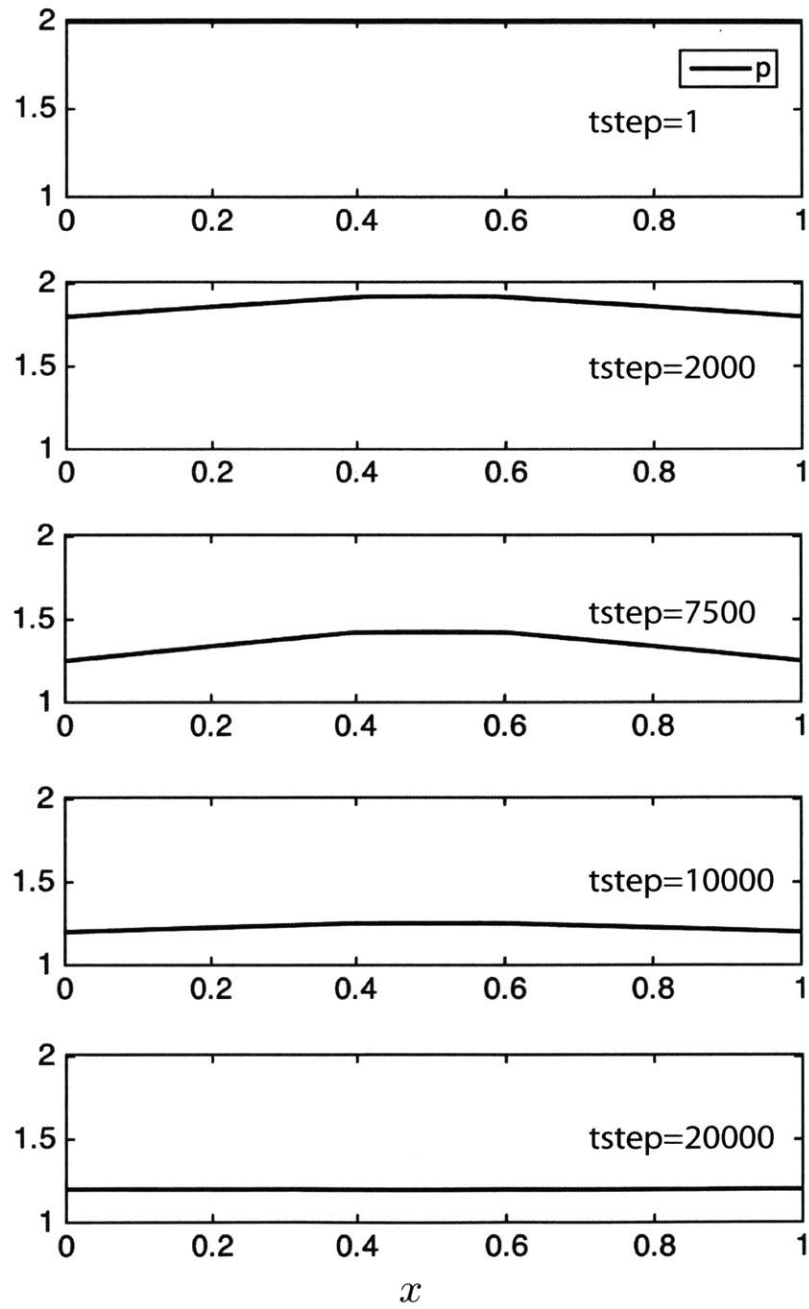


Figure 5-24: Snapshots of p during the expansion of a hydrate-crust bubble.

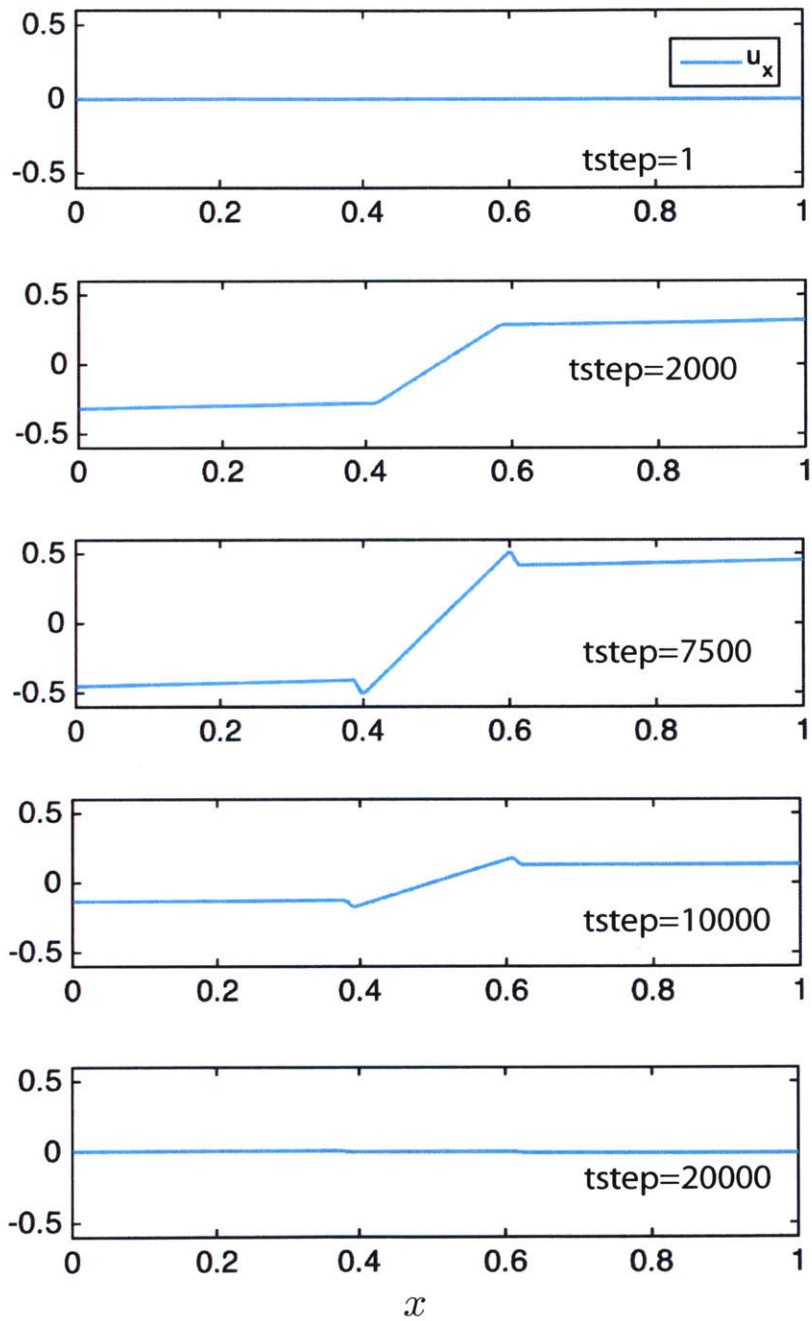


Figure 5-25: Snapshots of u_x during the expansion of a hydrate-crusted bubble.

5.7 Modeling rupturing behavior of a hydrate shell

To mimic the solid, shell-like behavior in the hydrate crust, we now assume that solid phase behaves as a highly viscous non-Newtonian fluid ($\mu_s > \mu_l$) with shear-thinning behavior:

$$\mu_s = \mu_s(\dot{\gamma}), \quad (5.73)$$

where $\dot{\gamma}$ is the shear rate.

5.7.1 General viscosity law for non-Newtonian fluid in bulk flow

In general, viscosity of a non-Newtonian fluid is described as a function of shear rate (Eq. (5.73)). We start by defining the shear rate, which is computed as a function of the strain-rate tensor ($\bar{\bar{\epsilon}}$):

$$\dot{\gamma} = (2\bar{\bar{\epsilon}} : \bar{\bar{\epsilon}})^{\frac{1}{2}}; \quad \bar{\bar{\epsilon}} = \frac{1}{2}(\nabla\mathbf{u} + \nabla\mathbf{u}^T)$$

Given that the velocity field in 2D is denoted as

$$\mathbf{u}(x, y) = \begin{bmatrix} u(x, y) \\ v(x, y) \end{bmatrix},$$

we can rewrite the shear rate in terms of the velocity field as:

$$\dot{\gamma} = \sqrt{2 \left(\frac{\partial u}{\partial x} \right)^2 + \left(\frac{\partial u}{\partial y} + \frac{\partial v}{\partial x} \right)^2 + 2 \left(\frac{\partial v}{\partial y} \right)^2}.$$

The Carreau-Yasuda model

This model is commonly used to describe viscosity of power-law fluids that exhibits shear-thinning or shear-thickening behavior:

$$\mu = \mu_0 [1 + (\tau\dot{\gamma})^2]^{(n-1)/2}, \quad (5.74)$$

where τ is the relaxation time of the stress, $n < 1$ for shear thinning fluids and $n > 1$ for shear-thickening fluids.

The Trompert-Hansen-Tackley model

This model is used in mantle convection simulations to generate pseudo-plasticity and plate-like behavior in fluids (Trompert and Hansen, 1998; Tackley, 2000a,b; van Heck and Tackley, 2008). Starting with a stress-dependent viscosity ($\mu_{\dot{\gamma}}$), the key ingredient of the method is to incorporate a critical yield-stress (σ^*) that renders the fluid shear-thinning once the local stress exceeds a critical value:

$$\mu_{\dot{\gamma}} = \mu^* + \frac{\sigma^*}{\dot{\gamma}}; \quad \sigma^* = \sigma^*(z).$$

The yield stress, σ^* , is a function of depth z (direction of gravity) so that the yield stress is largest at the top of the convection cell. In the context of thermal convection, the viscosity is also a function of local temperature:

$$\mu_T = \exp(-RT)$$

The total fluid viscosity is constructed as the harmonic mean between a temperature-dependent viscosity and a stress-dependent viscosity:

$$\mu = \frac{2}{\frac{1}{\mu_T} + \frac{1}{\mu_{\dot{\gamma}}}}.$$

5.7.2 A generalized Darcy's law for viscoelastic fluid in a Hele-Shaw cell

When the flow of interest is occurring in an unconfined domain, one often uses the Navier-Stokes equation to describe the momentum evolution. Under the Navier-Stokes framework, modeling viscosity of non-Newtonian fluid as a function of local shear rate ($\dot{\gamma}$) is a common practice. When flow occurs within a thin gap, as is

the case within a Hele-Shaw cell, the momentum equation simplifies to Darcy's law (Eq. (5.58)), and the description of shear-dependent viscosity can be simplified as well. A generalized Darcy's law for shear-thinning or shear-thickening fluids within a Hele-Shaw cell is proposed by Fast and coauthors (Fast et al., 2001):

$$\mathbf{u} = \frac{-k}{\mu(\text{We}^2|\nabla p|^2)}\nabla p, \quad (5.75)$$

where We is the Weissenberg number that compares the rate of advection to the rate of stress relaxation in the fluid:

$$\text{We} = \frac{12\tau U}{b},$$

where U is the characteristic velocity, b is the gap thickness of the Hele-Shaw cell and τ is the stress relaxation time.

For *weakly shear-thinning* fluids, (Fast et al., 2001) derived the following analytical expression that provides good approximation for viscosity law:

$$\mu_s = \mu_s^0 \frac{1 + \alpha|\text{We}\nabla p|^2}{1 + |\text{We}\nabla p|^2}, \quad (5.76)$$

where $\alpha > 1/9$ and μ_s^0 is the initial/maximum viscosity of the fluid. Note that here ∇p is in its dimensionless form.

For *strongly shear-thinning* fluids, there is no known analytical approximation. However, (Nguyen et al., 2010) have shown that at high shear-rate, the viscosity behavior can be modeled asymptotically as: $\mu_s \sim (\text{We}|\nabla p|)^{(n-1)/n}$. We reformulate this as:

$$\mu_s = \mu_s^0 \Delta\epsilon (\text{We}|\nabla p| + \Delta\epsilon)^{(n-1)/n}, \quad (5.77)$$

where $\Delta\epsilon$ is a regularization term and $n = 0.5$ in (Nguyen et al., 2010). In figure 5-26, we show the behavior of weakly and strongly thinning viscosities as a function of pressure gradient squared, where $\mu_s^0 = 10$, $\text{We} = 0.5$, $\alpha = 0.15$, $\Delta\epsilon = 0.1$ and $n = 0.5$.

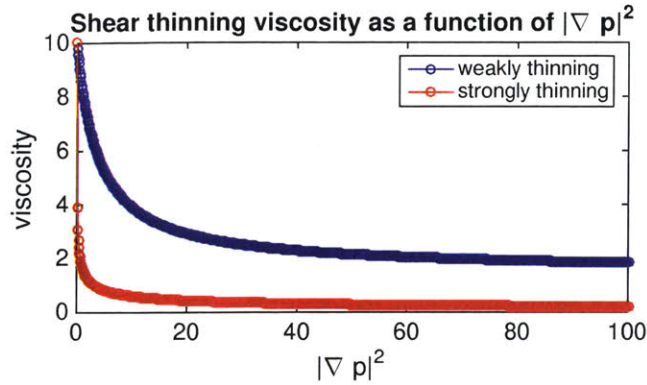


Figure 5-26: Shear thinning viscosities as a function of $|\nabla p|^2$ for weakly shear thinning (blue, Eq. (5.76)) and strongly shear-thinning (red, Eq. (5.77)) fluids.

5.7.3 2D simulation of hydrate shell rupturing

We perform the following simulation to demonstrate the ability of the above method to capture the rupturing behavior of a hydrate shell. In a long rectangular domain filled with mostly liquid, we introduce a volume of gas at the left of domain; initially a small amount of hydrate readily forms at the slightly perturbed gas-liquid interface (Fig. 5-27, $t = 0.3$). We then inject more gas through the left boundary under a constant flux so that the gas-liquid interface moves rightward. Due to a higher gas mobility, the initial protrusion on the gas-liquid interface becomes unstable, forming a gas finger that evades into the liquid. Meanwhile, the gas finger is also separated from the liquid by a hydrate layer that readily forms at the interface. The hydrate layer is much more viscous, which slows down the rate of gas invasion; however, the shear-thinning property of the hydrate allows the layer to be ruptured at the *thinnest* section, which is usually at the tip of the finger. The coupled fingering-rupturing process results in a meandering behavior of the gas finger, because the direction of movement is randomly determined by the thinnest section of the shell at a given time.

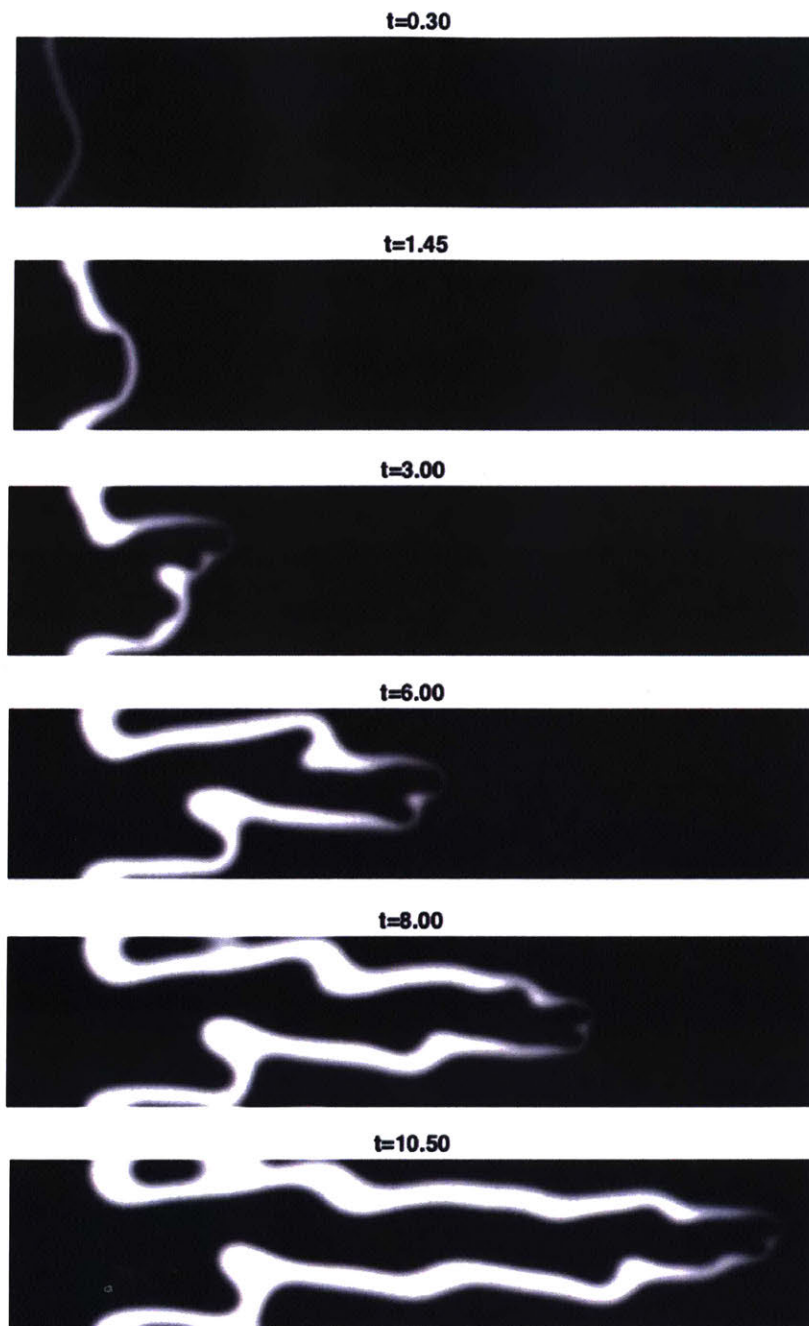


Figure 5-27: Evolution of the hydrate-crusted gas-liquid interface under a constant gas injection from left. The colors here correspond to volume fraction of hydrate (ϕ_s), where white indicates 1 and black indicates 0.

Chapter 6

Implications, discussions and conclusions

In this Thesis, we explore fundamental mechanisms controlling the physics of geologic CO₂ sequestration and natural gas hydrate systems, with an emphasis on the interplay between multiphase flow—the simultaneous motion of several fluid phases—and phase transitions—the creation or destruction of fluid or solid phases due to thermodynamically driven reactions.

In Chapter 2, we study the fate of CO₂ in saline aquifers in the presence of CO₂-brine-carbonate geochemical reactions. We use high-resolution simulations to examine the interplay between the density-driven convective mixing and the rock dissolution reactions. Our study considers a simplified geochemical system that only leads to mineral dissolutions. In practice, the presence of other minerals (e.g. gypsum) and ions can complicate the geochemical setup and lead to simultaneous dissolution and precipitation of different minerals (Elkhoury et al., 2013). Another limitation of our study is the assumption of homogeneous rock formation. In natural settings, rock formation is heterogeneous both in terms of permeability values and mineral compositions. This could change the coupled hydrodynamics and geochemical reactions significantly. However, the main conclusions from this study still provide valuable insights to the role of geochemical reactions during CO₂ sequestration. We find that dissolution of carbonate rock initiates in regions of locally high mixing, but that

the geochemical reaction shuts down significantly earlier than shutdown of convective mixing. This early shutdown reflects the important role that chemical speciation plays in this hydrodynamics–reaction coupled process. In the context of geologic CO₂ sequestration, we find that mineral dissolution reactions are most active towards the top boundary layer, where high concentration gradients lead to more fluid mixing. As a result, the permeability towards the top of the domain is significantly increased, which consequently increases the rate of CO₂ dissolution flux into the brine (faster solubility trapping).

In the rest of the Thesis, we study hydrodynamic and thermodynamic processes pertaining to a gas hydrate system under changing temperature and pressure conditions. The framework for our analysis is that of phase-field modeling of binary mixtures far from equilibrium. In Chapter 3 and 4, we focus on vapor–liquid mixtures made of two components and discuss the impact of two-way coupling between multiphase hydrodynamics and thermodynamically-driven phase transitions.

In Chapter 3, we demonstrate that the interplay between phase separation and hydrodynamic instability can arrest the Ostwald ripening process characteristic of nonflowing mixtures. As a result, the binary mixture maintains a statistical steady-state (coarsening is arrested), as measured by the average gas phase droplet size under the imposed flow. We also show that the liquid phase becomes permanently oversaturated because the thermodynamic equilibration process is interrupted by the imposed flow. In Chapter 4, we show that thermodynamic effects in the form of fluid partial miscibility exert a powerful control on the degree of viscous fingering in a gas–liquid system, whereby fluid dissolution hinders fingering while fluid exsolution enhances fingering.

In both Chapter 3 and Chapter 4, we do not consider the effect of density differences between the gas and liquid on the phase separation dynamics and hydrodynamics. We also assume that interfacial tension and fluid viscosity do not change as a result of component exchange between the two phases. This assumption allows us to simplify the parameter space for our simulations and thus focus on the effect of viscosity contrast and initial fluid compositions. However, these assumptions may no

longer be valid for realistic fluid pairs where density, viscosity and interfacial tension can change appreciably due to mass transfer across phases. It would be interesting to incorporate these effects in our current model in the future to fully understand ongoing experimental studies (Suzuki et al., 2016).

In Chapter 5, we employ the theoretical phase-field modeling approach to explain observations of bubble expansion coupled with gas dissolution and hydrate formation in controlled laboratory experiments. We focus on the growth of hydrate film on a gas-liquid interface and show that diffusion-limited transport of methane within the hydrate layer significantly hinders the thickening of hydrate film and prevents the system to reach true thermodynamic equilibrium. In the context of an ascending hydrate-crust bubble, our analysis provides a mechanistic understanding on how the hydrate crust could slow down the transport of methane into the water column. In future work, we will quantify the “shielding” effect by studying how much the mass transfer coefficient is reduced as a result of hydrate crust. We also address the issue of hydrate growth kinetics on a gas-liquid interface. Our results elucidate that aqueous methane saturation plays an important role in how fast hydrate thickens: when the liquid is undersaturated in methane (solubility measured as liquid phase composition at equilibrium with hydrate), the growth of hydrate is limited by transport of methane towards the solidification front and the phase transition is transport-limited; when the liquid is oversaturated, the growth is limited by the rate of thermodynamic phase transitions (kinetic-limited). The two regimes exhibit different scaling laws, where the kinetic-limited regime yields a higher effective growth rate. Our simulations have also shown that hydrate film can readily form on a gas-liquid interface even if the liquid phase is undersaturated in methane. This helps resolve a debated question from earlier experimental studies on whether aqueous phase saturation is required for hydrate formation on a gas bubble. Here, we agree with the conclusion by Chen et al. (2014, 2016) that aqueous saturation is *not* a required condition for hydrate film growth, given that other thermodynamic forcing such as pressure and sub-cooling can facilitate hydrate formation.

An important limitation of the study performed in Chapter 5 is that we do not

consider the density difference amongst the phases or the compressibility of gas in a closed system. We recognize that this will have an important impact on some of the conclusions. Specifically, if we consider realistic density and compressibility scenarios, the gas phase would have likely disappeared sooner in the simulations shown in sections 5.4 and 5.5. To overcome this shortcoming, in section 5.6 we describe ongoing work in improving our model to consider density contrast and fluid compressibility. We believe continued effort in this direction will improve our description of the rheology and pressure distribution of a hydrate-crust bubble, which will help us unravel the coupling between pressure and hydrate formation that lead to the buckling of a hydrate shell. A mechanistic explanation of the buckling process will inform our understanding of the fate of hydrate-crust methane bubbles in the ocean water column and the migration of gas pockets in hydrate-bearing sediments.

Bibliography

- Abay, H. K. and T. M. Svartaas. On the kinetics of methane hydrate formation: a time-dependent kinetic rate model. In *Proceedings of the 7th International Conference on Gas Hydrates*, 2011.
- Al-Housseiny, T. T., P. A. Tsai, and H. A. Stone. Control of interfacial instabilities using flow geometry. *Nat. Phys.*, 8(10):747–750, 2012.
- Allen, S. M. and J. W. Cahn. A microscopic theory for antiphase boundary motion and its application to antiphase domain coarsening. *Acta Metall.*, 27(6):1085–1095, 1979.
- Aman, Z. M. and C. A. Koh. Interfacial phenomena in gas hydrate systems. *Chem. Soc. Rev.*, 45:1678–1690, 2016.
- Anderson, D. M. , G. B. McFadden, and A. A. Wheeler. Diffuse-interface methods in fluid mechanics. *Annu. Rev. Mater. Res.*, 30:139–165, 1998.
- Anderson, D. M., G. B. McFadden, and A. A. Wheeler. Diffuse-interface methods in fluid mechanics. *Annu. Rev. Fluid Mech.*, 30(1):139–165, January 1998.
- Andre, B. J. and H. Rajaram. Dissolution of limestone fractures by cooling waters: Early development of hypogene karst systems. *Water Resour. Res.*, 41(1):W01015, 2005.
- Arnéodo, A., Y. Couder, G. Grasseau, V. Hakim, and M. Rabaud. Uncovering the analytical Saffman-Taylor finger in unstable viscous fingering and diffusion-limited aggregation. *Phys. Rev. Lett.*, 63:984–987, 1989.
- Aubertin, A., G. Gauthier, J. Martin, D. Salin, and L. Talon. Miscible viscous fingering in microgravity. *Phys. Fluids*, 21:054107, 2009.
- Aussillous, P. and D. Quéré. Quick deposition of a fluid on the wall of a tube. *Phys. Fluids*, 12:2367–2371, 2000.
- Backhaus, S., K. Turitsyn, and R. E. Ecke. Convective instability and mass transport of diffusion layers in a Hele-Shaw geometry. *Phys. Rev. Lett.*, 106(10):104501, 2011.
- Ballard, A. L. and E. D. Sloan. The next generation of hydrate prediction: I. Hydrate standard states and incorporation of spectroscopy. *Fluid Phase Equilib.*, 194-197: 371–383, 2002.

- Ballard, A. L. and E. D. Sloan. The next generation of hydrate prediction IV: A comparison of available hydrate prediction programs. *Fluid Phase Equilib.*, 216(2): 257–270, 2004a.
- Ballard, A. L. and E. D. Sloan. The next generation of hydrate prediction: Part III. Gibbs energy minimization formalism. *Fluid Phase Equilib.*, 218(1):15–31, 2004b.
- Berthier, L., J.-L. Barrat, and J. Kurchan. Phase separation in a chaotic flow. *Phys. Rev. Lett.*, 86(10):2014–2017, 2001.
- Berti, S., G. Boffetta, M. Cencini, and A. Vulpiani. Turbulence and coarsening in active and passive binary mixtures. *Phys. Rev. Lett.*, 95(22):224501, 2005.
- Bertozzi, A. L., N. Ju, and H.-W. Lu. A biharmonic-modified forward time stepping method for fourth order nonlinear diffusion equations. *J. Discrete Continuous Dyn. Syst.*, 29(4):1367–1391, 2011.
- Biastoch, A., T. Treude, L. H. Rüpke, U. Riebesell, C. Roth, E. B. Burwicz, W. Park, M. Latif, C. W. Böning, G. Madec, and K. Wallmann. Rising arctic ocean temperatures cause gas hydrate destabilization and ocean acidification. *Geophys. Res. Lett.*, 38(8):L08602, April 2011.
- Bischofberger, I., R. Ramachandran, and S. R. Nagel. Fingering versus stability in the limit of zero interfacial tension. *Nat. Comm.*, 5:5265, 2014.
- Boettinger, W. J. , J. A. Warren, C. Beckermann, and A. Karma. Phase-Field simulation of solidification. *Annu. Rev. Mater. Res.*, 32:163–194, 2002.
- Bolster, D. The fluid mechanics of dissolution trapping in geologic storage of CO₂. *J. Fluid Mech.*, 740:1–4, 2014.
- Brangwynne, C. P., P. Tompa, and R. V. Pappu. Polymer physics of intracellular phase transitions. *Nat. Phys.*, 11(November):899–904, 2015.
- Bray, A. J. Theory of phase ordering kinetics. *Adv. Phys.*, 43:357–459, 1994.
- Bray, A. J. Theory of phase ordering kinetics. *Adv. Phys.*, 43:357–459, 1995.
- Cahn, J. W. and J. E. Hilliard. Free energy of a nonuniform system. I. Interfacial free energy. *J. Chem. Phys.*, 28(2):258, 1958.
- Carroll, S., Y. Hao, M. Smith, and Y. Sholokhova. Development of scaling parameters to describe CO₂-rock interactions within Weyburn-Midale carbonate flow units. *Int. J. Greenh. Gas Control*, 16:S185–S193, 2013.
- Chen, C.-Y. and E. Meiburg. Miscible displacements in a capillary tube. part 2. numerical simulations. *J. Fluid Mech.*, 326:57–90, 1996.

- Chen, C.-Y. and E. Meiburg. Miscible porous media displacements in the quarter five-spot configuration. Part 1. The homogeneous case. *J. Fluid Mech.*, 371:233–268, 1998.
- Chen, C.-Y. and E. Meiburg. Miscible displacements in capillary tubes: Influence of Korteweg stresses and divergence effects. *Phys. Fluids*, 14(7):2052–2058, 2002.
- Chen, C.-Y. and P.-Y. Yan. A diffuse interface approach to injection-driven flow of different miscibility in heterogeneous porous media. *Phys. Fluids*, 27(8):083101, 2015.
- Chen, C.-Y., L. Wang, and E. Meiburg. Miscible droplets in a porous medium and the effects of Korteweg stresses. *Phys. Fluids*, 13(9):2447–2456, 2001.
- Chen, C.-Y., C. W. Huang, L. C. Wang, and J. A. Miranda. Controlling radial fingering patterns in miscible confined flows. *Phys. Rev. E*, 82:056308, 2010.
- Chen, C.-Y., Y.-C. Huang, Y.-S. Huang, and J. A. Miranda. Enhanced mixing via alternating injection in radial Hele-Shaw flows. *Phys. Rev. E*, 92:043008, 2015.
- Chen, J.-D. Fingering in Hele-Shaw cells. *Exp. Fluids*, 5:363–371, 1987.
- Chen, J.-D. Growth of radial viscous fingers in a Hele-Shaw cell. *J. Fluid Mech.*, 201(-1):223, 1989.
- Chen, L., J. S. Levine, M.W. Gilmer, E. Dendy Sloan, C. A. Koh, and A. K. Sum. Methane hydrate formation and dissociation on suspended gas bubbles in water. *J. Chem. Eng. Data*, 59(4):1045–1051, 2014.
- Chen, L., J. S. Levine, M.W. Gilmer, E. Dendy Sloan, C. A. Koh, and A. K. Sum. Correction to “Methane hydrate formation and dissociation on suspended gas bubbles in water”. *J. Chem. Eng. Data*, 61(7):2647–2647, 2016.
- Choudhury, A., M. Plapp, and B. Nestler. Theoretical and numerical study of lamellar eutectic three-phase growth in ternary alloys. *Phys. Rev. E*, 83(5):1–20, 2011.
- Chui, J. Y. Y., P. de Anna, and R. Juanes. Interface evolution during radial miscible viscous fingering. *Phys. Rev. E*, 92:041003, 2015.
- Clerk-Maxwell, J. . On the dynamical evidence of the molecular constitution of bodies. *Nature*, 11:357–359, 1875.
- Clift, R., J.R. Grace, and M.E. Weber. *Bubbles, Drops, and Particles*. Academic Press, 1978.
- Cogswell, D. A. and W. C. Carter. Thermodynamic phase-field model for microstructure with multiple components and phases: The possibility of metastable phases. *Phys. Rev. E*, 83(6):1–13, 2011.

- Cueto-Felgueroso, L. and R. Juanes. Nonlocal interface dynamics and pattern formation in gravity-driven unsaturated flow through porous media. *Phys. Rev. Lett.*, 101:244504, 2008.
- Cueto-Felgueroso, L. and R. Juanes. Macroscopic phase-field model of partial wetting: bubbles in a capillary tube. *Phys. Rev. Lett.*, 108(14):144502, 2012a.
- Cueto-Felgueroso, L. and R. Juanes. Macroscopic phase-field model of partial wetting: bubbles in a capillary tube. *Phys. Rev. Lett.*, 108(14):144502, April 2012b.
- Cueto-Felgueroso, L. and R. Juanes. A phase-field model of two-phase Hele-Shaw flow. *J. Fluid Mech.*, 758:522–552, 2014.
- Cueto-Felgueroso, L. and J. Peraire. A time-adaptive finite volume method for the Cahn-Hilliard and Kuramoto-Sivashinsky equations. *J. Comput. Phys.*, 227(24): 9985–10017, December 2008.
- Daccord, G. and R. Lenormand. Fractal patterns from chemical dissolution. *Nature*, 325(6099):41–43, 1987.
- De Simoni, M., J. Carrera, X. Sánchez-Vila, and A. Guadagnini. A procedure for the solution of multicomponent reactive transport problems. *Water Resour. Res.*, 41(11):W11410, 2005.
- De Simoni, M., X. Sánchez-Vila, J. Carrera, and M. W. Saaltink. A mixing ratios-based formulation for multicomponent reactive transport. *Water Resour. Res.*, 43(7):W07419, 2007.
- De Wit, A. Fingering of chemical fronts in porous media. *Phys. Rev. Lett.*, 87(5): 054502, 2001.
- Detwiler, R. L. and H. Rajaram. Predicting dissolution patterns in variable aperture fractures: Evaluation of an enhanced depth-averaged computational model. *Water Resour. Res.*, 43(4):W04403, 2007.
- Dias, E. O., E. Alvarez-Lacalle, M. S. Carvalho, and J. A. Miranda. Minimization of viscous fluid fingering: A variational scheme for optimal flow rates. *Phys. Rev. Lett.*, 109(14):144502, 2012.
- Dranchuk, P.M. and H. Abou-Kassem. Calculation of Z factors for natural gases using equations of state. *J. Can. Pet. Technol.*, 14(34), 1975.
- Elkhoury, J. E., P. Ameli, and R. L. Detwiler. Dissolution and deformation in fractured carbonates caused by flow of CO₂-rich brine under reservoir conditions. *Int. J. Greenh. Gas Control*, 16:S203–S215, 2013.
- Ennis-King, J. and L. Paterson. Role of convective mixing in the long-term storage of carbon dioxide in deep saline formations. *Soc. Pet. Eng. J.*, 10(3):349–356, September 2005.

- Fan, D., S. P. Chen, L. Q. Chen, and P. W. Voorhees. Phase-field simulation of 2-D Ostwald ripening in the high volume fraction regime. *Acta Mater.*, 50(8):1895–1907, 2002.
- Fast, P., L. Kondic, M. J. Shelley, and P. Palffy-Muhoray. Pattern formation in non-Newtonian Hele-Shaw flow. *Phys. Fluids*, 13(5):1191–1212, 2001.
- Ferré, B., J. Mienert, and T. Feseker. Ocean temperature variability for the past 60 years on the Norwegian-Svalbard margin influences gas hydrate stability on human time scales. *J. Geophys. Res.*, 117(C10):C10017, October 2012.
- Folch, R. and M. Plapp. Quantitative phase-field modeling of two-phase growth. *Phys. Rev. E*, 72(1):011602, 2005.
- Folch, R., J. Casademunt, A. Hernández-Machado, and L. Ramirez-Piscina. Phase-field models for Hele-Shaw flows with arbitrary viscosity contrast. I. theoretical approach. *Phys. Rev. E*, 60:1724–1733, 1999a.
- Folch, R., J. Casademunt, A. Hernández-Machado, and L. Ramirez-Piscina. Phase-field models for Hele-Shaw flows with arbitrary viscosity contrast. II. numerical study. *Phys. Rev. E*, 60:1734–1740, 1999b.
- Fu, X., L. Cueto-Felgueroso, and R. Juanes. Pattern formation and coarsening dynamics in three-dimensional convective mixing in porous media. *Phil. Trans. R. Soc. A*, 371:20120355, 2013.
- Fu, X., L. Cueto-Felgueroso, D. Bolster, and R. Juanes. Rock dissolution patterns and geochemical shutdown of CO₂-brine-carbonate reactions during convective mixing in porous media. *J. Fluid Mech.*, 764:296–315, 2015.
- Fu, X., L. Cueto-Felgueroso, and R. Juanes. Thermodynamic coarsening arrested by viscous fingering in partial-miscible binary mixtures. *Phys. Rev. E*, 94(3):033111, 2016.
- Fu, X., L. Cueto-Felgueroso, and R. Juanes. *in review*, 2017.
- Furukawa, H. A dynamic scaling assumption for phase separation. *Adv. Phys.*, 34:703–750, 1985.
- Gomez, H., T. J.R. Hughes, X. Nogueira, and V. M. Calo. Isogeometric analysis of the isothermal Navier-Stokes-Korteweg equations. *Comput. Meth. Appl. Mech. Eng.*, 199(25-28):1828–1840, May 2010.
- Graves, C. A., L. Steinle, G. Rehder, H. Niemann, D. P. Connelly, D. Lowry, R. E. Fisher, A. W. Stott, H. Sahling, and R. H. James. Fluxes and fate of dissolved methane released at the seafloor at the landward limit of the gas hydrate stability zone offshore western Svalbard. *J. Geophys. Res. Oceans*, 120(9):6185–6201, 2015.

- Greinert, J. and D. F. McGinnis. Single bubble dissolution model —The graphical user interface SiBu-GUI. *Environ. Modell. Softw.*, 24(8):1012–1013, August 2009.
- Greinert, J., D. F. McGinnis, L. Naudts, P. Linke, and M. De Batist. Atmospheric methane flux from bubbling seeps: Spatially extrapolated quantification from a Black Sea shelf area. *J. Geophys. Res.*, 115(C1):C01002, January 2010.
- Guadagnini, A., X. Sanchez-Vila, M. W. Saaltink, M. Bussini, and B. Berkowitz. Application of a mixing-ratios based formulation to model mixing-driven dissolution experiments. *Adv. Water Resour.*, 32(5):756–766, 2009.
- Hammond, G. E., P. C. Lichtner, C. Lu, and R.T. Mills. PFLOTRAN: Reactive flow and transport code for use on laptops to leadership-class supercomputers. In F. Zhang, G.T. Yeh, and J. C. Parker, editors, *Groundwater Reactive Transport Models*, pages 141–159. Bentham Science Publishers, Sharjah, UAE, 2012.
- Hashimoto, T., K. Matsuzaka, E. Moses, and A. Onuki. String phase in phase-separating fluids under shear flow. *Phys. Rev. Lett.*, 74(1):126–129, 1995.
- Hassanzadeh, H., M. Pooladi-Darvish, and D. W. Keith. Scaling behavior of convective mixing, with application to geological storage of CO₂. *AIChE J.*, 53(5):1121–1131, 2007.
- Haudin, F., J. H. E. Cartwright, F. Brau, and A. De Wit. Spiral precipitation patterns in confined chemical gardens. *Proc. Natl. Acad. Sci. U.S.A.*, 111(49):17363–17367, 2014.
- Helgeson, H. C. and D. H. Kirkham. Theoretical prediction of the thermodynamic behaviour of aqueous electrolytes at high pressure and temperature: II Debye-Hückel parameters for activity coefficients and relative partial molal properties. *Am. J. Sci.*, 274:1199–1261, 1974.
- Henry, W. Experiments on the quantity of gases absorbed by water, at different temperatures, and under different pressures. *Phil. Trans. R. Soc. A*, 93:29–42+274–276, 1803.
- Hernández-Machado, A. and M. Lacasta, E. Mayoral, and E. Corvera-Poiré. Phase-field model of Hele-Shaw flows in the high-viscosity contrast regime. *Phys. Rev. E*, 68:046310, 2003.
- Hewitt, D. R. , J. A. Neufeld, and J. R. Lister. Convective shutdown in a porous medium at high Rayleigh number. *J. Fluid Mech.*, 719:551–586, 2013.
- Hidalgo, J. J. and J. Carrera. Effect of dispersion on the onset of convection during CO₂ sequestration. *J. Fluid Mech.*, 640:441–452, 2009.
- Hidalgo, J. J., J. Fe, L. Cueto-Felgueroso, and R. Juanes. Scaling of convective mixing in porous media. *Phys. Rev. Lett.*, 109:264503, 2012.

- Hohenberg, P. and B. Halperin. Theory of dynamic critical phenomena. *Rev. Mod. Phys.*, 49(3):435–479, 1977.
- Homsy, G. M. Viscous fingering in porous media. *Annu. Rev. Fluid Mech.*, 19(1): 271–311, 1987.
- Huo, Z., K. Hester, E. D. Sloan, and K. T. Miller. Methane hydrate nonstoichiometry and phase diagram. *AIChE J.*, 49(5):1300–1306, 2003.
- IPCC. *Special report on carbon dioxide capture and storage*, B. Metz et al. (eds.). Cambridge University Press, 2005.
- Jager, M. D., A. L. Ballard, and E. D. Sloan. The next generation of hydrate prediction: II. Dedicated aqueous phase fugacity model for hydrate prediction. *Fluid Phase Equilib.*, 211(1):85–107, 2003.
- Jha, B., L. Cueto-Felgueroso, and R. Juanes. Fluid mixing from viscous fingering. *Phys. Rev. Lett.*, 106(19):194502, 2011.
- Jha, B., L. Cueto-Felgueroso, and R. Juanes. Synergetic Fluid Mixing from Viscous Fingering and Alternating Injection. *Phys. Rev. Lett.*, 111(14):144501, oct 2013.
- Kamath, V.A. *Study of heat transfer characteristics during dissociation of gas hydrates in porous media*. PhD thesis, University of Pittsburgh, 1984.
- Karma, A. Phase-field formulation for quantitative modeling of alloy solidification. *Phys. Rev. Lett.*, 87(11):115701, 2001.
- Kirschke, S., Philippe Bousquet, Philippe Ciais, Marielle Saunois, Josep G. Canadell, Edward J. Dlugokencky, Peter Bergamaschi, Daniel Bergmann, Donald R. Blake, Lori Bruhwiler, Philip Cameron-Smith, Simona Castaldi, Frédéric Chevallier, Liang Feng, Annemarie Fraser, Martin Heimann, Elke L. Hodson, Sander Houweling, Béatrice Josse, Paul J. Fraser, Paul B. Krummel, Jean-François Lamarque, Ray L. Langenfelds, Corinne Le Quéré, Vaishali Naik, Simon O’Doherty, Paul I. Palmer, Isabelle Pison, David Plummer, Benjamin Poulter, Ronald G. Prinn, Matt Rigby, Bruno Ringeval, Monia Santini, Martina Schmidt, Drew T. Shindell, Isobel J. Simpson, Renato Spahni, L. Paul Steele, Sarah A. Strode, Kengo Sudo, Sophie Szopa, Guido R. van der Werf, Apostolos Voulgarakis, Michiel van Weele, Ray F. Weiss, Jason E. Williams, and Guang Zeng. Three decades of global methane sources and sinks. *Nat. Geosci.*, 6(10):813–823, September 2013.
- Kneafsey, T. J. and K. Pruess. Laboratory flow experiments for visualizing carbon dioxide-induced, density-driven brine convection. *Transp. Porous Media*, 82:123–139, 2010.
- Kvenvolden, K. A. and T.D. Lorenson. *The Global Occurrence of Natural Gas Hydrate*, pages 3–18. American Geophysical Union, 2001.
- Lackner, K. S. A guide to CO₂ sequestration. *Science*, 300(5626):1677–1678, 2003.

- Lajeunesse, E. and Y. Couder. On the tip-splitting instability of viscous fingers. *J. Fluid Mech.*, 419:125–149, 2000.
- Lajeunesse, E., J. Martin, N. Rakotomalala, and D. Salin. 3D Instability of miscible displacements in a Hele-Shaw cell. *Phys. Rev. Lett.*, 79(26):5254–5257, 1997.
- Lee, H.-G., J. S. Lowengrub, and J. Goodman. Modeling pinchoff and reconnection in a Hele-Shaw cell. I. the models and their calibration. *Phys. Fluids*, 14:492–513, 2002a.
- Lee, H.-G., J. S. Lowengrub, and J. Goodman. Modeling pinchoff and reconnection in a Hele-Shaw cell. II. analysis and simulation in the nonlinear regime. *Phys. Fluids*, 14:514–545, 2002b.
- Leifer, I., B. P. Luyendyk, J. Boles, and J. F. Clark. Natural marine seepage blowout: Contribution to atmospheric methane. *Global Biogeochem. Cy.*, 20(3), September 2006.
- Lele. S.K. Compact finite difference schemes with spectral-like resolution. *J. Comput. Phys.*, 103:16–42, 1992.
- Levaché, B. and D. Bartolo. Revisiting the Saffman-Taylor experiment: imbibition patterns and liquid-entrainment transitions. *Phys. Rev. Lett.*, 113(4):044501, jul 2014.
- Li, S., J. S. Lowengrub, J. Fontana, and P. Palffy-Muhoray. Control of viscous fingering patterns in a radial Hele-Shaw cell. *Phys. Rev. Lett.*, 102(17):174501, 2009.
- Li, S.-L., C.-Y. Sun, B. Liu, Z.-Y. Li, G.-J. Chen, and A. K Sum. New observations and insights into the morphology and growth kinetics of hydrate films. *Sci. Rep.*, 4:4129, 2014.
- Lichtner, P. C. Continuum formulation of multicomponent-multiphase reactive transport. In P. C. Lichtner, C. I. Steefel, and E. H. Oelkers, editors, *Reactive Transport in Porous Media*, volume 34 of *Reviews in Mineralogy*, chapter 1, pages 1–81. Mineralogical Society of America, Washington, DC, 1996.
- Lifshitz, I. M. and V. V. Slyozov. The kinetics of precipitation from supersaturated solid solutions. *J. Phys. Chem. Solids*, 19:35–50, 1961.
- Lindeberg, E. and D. Wessel-Berg. Vertical convection in an aquifer column under a gas cap of CO₂. *Energy Conv. Manag.*, 38:S229–S234, 1997.
- Linder, A., D. Bonn, E. Poiré Corvera, M. Ben Amar, and J. Meunier. Viscous fingering in non-Newtonian fluids. *J. Fluid Mech.*, 469:237–256, 2002.
- Lowengrub, J. and L. Truskinovsky. Quasi-incompressible Cahn-Hilliard fluids and topological transitions. *Proc. R. Soc. Lond. A*, 454:2617–2654, 1998.

- MacMinn, C. W. and R. Juanes. Buoyant currents arrested by convective dissolution. *Geophys. Res. Lett.*, 40:2017–2022, 2013.
- MacMinn, C. W., M. L. Szulczewski, and R. Juanes. CO₂ migration in saline aquifers. Part 2: Capillary and solubility trapping. *J. Fluid Mech.*, 688:321–351, 2011.
- MacMinn, C. W., J. A. Neufeld, M. A. Hesse, and H. E. Huppert. Spreading and convective dissolution of carbon dioxide in vertically confined, horizontal aquifers. *Water Resour. Res.*, 48:W11516, 2012.
- Maher, J. V. Development of viscous fingering patterns. *Phys. Rev. Lett.*, 54(14): 1498–1501, 1985.
- Maini, B. B. and P. R. Bishnoi. Experimental investigation of hydrate formation behaviour of a natural gas bubble in a simulated deep sea environment. *Chem. Eng. Sci.*, 36:183–189, 1981.
- Martinez, M. J. and M. A. Hesse. Two-phase convective CO₂ dissolution in saline aquifers. *Water Resour. Res.*, 52:585–599, 2016.
- Mau, S., D. L. Valentine, J. F. Clark, J. Reed, R. Camilli, and L. Washburn. Dissolved methane distributions and air-sea flux in the plume of a massive seep field, coal oil point, california. *Geophys. Res. Lett.*, 34(22):L22603, 2007.
- Maxworthy, T. Bubble formation, motion and interaction in a Hele-Shaw cell. *J. Fluid Mech.*, 173:95–114, 1986.
- McGinnis, D. F., J. Greinert, Y. Artemov, S. E. Beaubien, and a. Wüest. Fate of rising methane bubbles in stratified waters: How much methane reaches the atmosphere? *J. Geophys. Res.*, 111(C9):C09007, 2006.
- Meiburg, E. and G. M. Homsy. Nonlinear unstable viscous fingers in HeleShaw flows. II. Numerical simulation. *Phys. Fluids*, 31(3):429, 1988.
- Meindinyo, R.-E. and T. Svartaas. Gas hydrate growth Kinetics: a parametric study. *Energies*, 9(12):1021, 2016.
- Mienert, J., M. Vanneste, S. Bünz, Andreassen K., H. Hafidason, and H. P. Sejrup. Ocean warming and gas hydrate stability on the mid-norwegian margin at the storegga slide. *Mar. Petrol. Geol.*, 22:233 – 244, 2005.
- Min, K. Y. and W. I. Goldburg. Nucleation of a binary liquid mixture under steady-state shear. *Phys. Rev. Lett.*, 70(4):469–472, 1993.
- Mochizuki, T. and Y. H. Mori. Numerical simulation of transient heat and mass transfer controlling the growth of a hydrate film. *Ann. N. Y. Acad. Sci.*, 912: 642–650, 2000.
- Moelans, N. A quantitative and thermodynamically consistent phase-field interpolation function for multi-phase systems. *Acta Mater.*, 59(3):1077–1086, 2011.

- Mori, Y. H. and T. Mochizuki. Mass transport across clathrate hydrate films— a capillary permeation model. *Chem. Eng. Sci.*, 52:3613–3616, 1998.
- Mori, Y. H. and T. Mochizuki. Modeling of simultaneous heat and mass transfer to/from and across a hydrate film. *Ann. N. Y. Acad. Sci.*, 912:633–641, 2000.
- Nagatsu, Y., Y. Ishii, Y. Tada, and A. De Wit. Hydrodynamic fingering instability induced by a precipitation reaction. *Phys. Rev. Lett.*, 113(2):024502, 2014.
- Nestler, B., A. A. Wheeler, L. Ratke, and C. Stöcker. Phase-field model for solidification of a monotectic alloy with convection. *Physica D*, 141:133–154, 2000.
- Neufeld, J. A., M. A. Hesse, A. Riaz, M. A. Hallworth, H. A. Tchelepi, and H. E. Huppert. Convective dissolution of carbon dioxide in saline aquifers. *Geophys. Res. Lett.*, 37:L22404, 2010.
- Nguyen, S., R. Folch, V. K. Verma, H. Henry, and M. Plapp. Phase-field simulations of viscous fingering in shear-thinning fluids. *Phys. Fluids*, 22(10), 2010.
- Nield, D. A. and A. Bejan. *Convection in Porous Media*. Springer, New York, 3 edition, 2006.
- Ober, T. J., D. Foresti, and J. A. Lewis. Active mixing of complex fluids at the microscale. *Proc. Natl. Acad. Sci. U.S.A.*, 112(40):12293–12298, 2015.
- Ohgaki, K., T. Sugahara, M. Suzuki, and H. Jindai. Phase behavior of xenon hydrate system. *Fluid Phase Equilib.*, 175(1-2):1–6, 2000.
- Oliveira, R. M. and E. Meiburg. Miscible displacements in Hele-Shaw cells: three-dimensional Navier–Stokes simulations. *J. Fluid Mech.*, 687:431–460, 2011.
- Oliveira, R. M. and E. Meiburg. Saffman–Taylor instability and the inner splitting mechanism. *Phys. Rev. Lett.*, 118:124502, 2017.
- Olivella, S., A. Gens, J. Carrera, and E. E. Alonso. Numerical formulation for a simulator (code.bright) for the coupled analysis of saline media. *Eng. Comput.*, 13(7):87, 1996.
- Orr, F. M. *Theory of gas injection processes*. Tie-Line Publications, 2007.
- Orr, F. M. Onshore geologic storage of CO₂. *Science*, 325:1656–1658, 2009.
- Ostwald, W. “Über die vermeintliche Isomerie des roten und gelben Quecksilbersoxyds und die Oberflächenspannung fester Körper”. *Zeit. für Physik Chemie*, 34: 495–503, 1900.
- Park, C. W. and G. M. Homsy. The instability of long fingers in HeleShaw flows. *Phys. Fluids*, 28(6):1583, 1985.

- Parkhurst, D. L. *User's guide to PHREEQC: A computer program for speciation, reaction-path, advective-transport, and inverse geochemical calculations, water resources investigations report*. Lakewood, Colo., 1995.
- Paterson, L. Radial fingering in a Hele-Shaw cell. *J. Fluid Mech.*, 113:513–529, 1981.
- Pau, G. S. H. , J. B. Bell, K. Pruess, A. S. Almgren, M. J. Lijewski, and K. Zhang. High-resolution simulation and characterization of density-driven flow in CO₂ storage in saline aquifers. *Adv. Water Resour.*, 33(4):443–455, 2010.
- Peng, B. Z., A. Dandekar, C.Y. Sun, H. Luo, Q.L. Ma, W.X. Pang, and G.J. Chen. Hydrate film growth on the surface of a gas bubble suspended in water. *J. Phys. Chem. B*, 111:12485–12493, 2007.
- Perlekar, P., R. Benzi, H. J. H. Clercx, D. R. Nelson, and F. Toschi. Spinodal decomposition in homogeneous and isotropic turbulence. *Phys. Rev. Lett.*, 112(1):014502, 2014.
- Peters, B., N. E. R. Zimmermann, G. T. Beckham, J. W. Tester, and B. L. Trout. Path sampling calculation of methane diffusivity in natural gas hydrates from a water-vacancy assisted mechanism. *J. Am. Chem. Soc.*, 130(51):17342–17350, 2008.
- Petitjeans, P. and T. Maxworthy. Miscible displacements in capillary tubes. Part 1. Experiments. *J. Fluid Mech.*, 326:37–56, 1996.
- Phrampus, B. J. and M. J. Hornbach. Recent changes to the Gulf Stream causing widespread gas hydrate destabilization. *Nature*, 490(7421):527–30, October 2012.
- Pihler-Puzović, D., P. Illien, M. Heil, and A. Juel. Suppression of complex fingerlike patterns at the interface between air and a viscous fluid by elastic membranes. *Phys. Rev. Lett.*, 108(7):074502, 2012.
- Pine, D. J., N. Easwar, J.V. Maher, and W.I. Goldberg. Turbulent suppression of spinodal decomposition. *Phys. Rev. A*, 29(1):308–313, 1984.
- Plapp, M. Unified derivation of phase-field models for alloy solidification from a grand-potential functional. *Phys. Rev. E*, 84(3):031601, 2011.
- Plummer, L. N., T. M. L. Wigley, and D. L. Parkhurst. The kinetics of calcite dissolution in CO₂-water systems at 5° to 60°C and 0.0 to 1.0 atm CO₂. *Am. J. Sci.*, 278:179–216, 1978.
- Reagan, M. T. and G. J. Mordis. Dynamic response of oceanic hydrate deposits to ocean temperature change. *J. Geophys. Res.*, 113(C12):C12023, December 2008.
- Rehder, G., P. W. Brewer, E. T. Peltzer, and G. Friederich. Enhanced lifetime of methane bubble streams within the deep ocean. *Geophys. Res. Lett.*, 29(15):21–1–21–4, August 2002.

- Rehder, G., I. Leifer, P. G. Brewer, G. Friederich, and E. T. Peltzer. Controls on methane bubble dissolution inside and outside the hydrate stability field from open ocean field experiments and numerical modeling. *Mar. Chem.*, 114(1-2):19–30, 2009.
- Rezaei, M., E. Sanz, E. Raeisi, C. Ayora, E. Vázquez-Suñé, and J. Carrera. Reactive transport modeling of calcite dissolution in the fresh-salt water mixing zone. *J. Hydrol.*, 311:282–298, 2005.
- Riaz, A. and E. Meiburg. Three-dimensional miscible displacement simulations in homogeneous porous media with gravity override. *J. Fluid Mech.*, 494:95–117, 2003a.
- Riaz, A. and E. Meiburg. Three-dimensional miscible displacement simulations in homogeneous porous media with gravity override. *J. Fluid Mech.*, 494:95–117, 2003b.
- Riaz, A., M. Hesse, H. A. Tchelepi, and F. M. Orr. Onset of convection in a gravitationally unstable, diffusive boundary layer in porous media. *J. Fluid Mech.*, 548: 87–111, 2006.
- Romanov, D. and W. Dreybrodt. Evolution of porosity in the saltwater–freshwater mixing zone of coastal carbonate aquifers: An alternative modelling approach. *J. Hydrol.*, 329:661–673, 2006.
- Römer, M., H. Sahling, T. Pape, G. Bohrmann, and V. Spieß. Quantification of gas bubble emissions from submarine hydrocarbon seeps at the makran continental margin (offshore pakistan). *J. Geophys. Res. Oceans*, 117(C10), 2012.
- Rowlinson, J. S. Translation of J. D. van der Waals’ “The thermodynamik theory of capillarity under the hypothesis of a continuous variation of density”. *J. Stat. Phys.*, 20(2):197–200, 1979.
- Ruith, M. and E. Meiburg. Miscible rectilinear displacements with gravity override. Part 1. Homogeneous porous medium. *J. Fluid Mech.*, 420:225–257, 2000.
- Ruiz, R. and D. Nelson. Turbulence in binary fluid mixtures. *Phys. Rev. A*, 23:6, 1981.
- Ruppel, C. Tapping methane hydrates for unconventional natural gas. *Elements*, 3: 193–199, 2007.
- Ruppel, C. and J. D. Kessler. The interaction of climate change and methane hydrates. *Rev. Geophys.*, 55, 2017.
- Saaltink, M. W., C. Ayora, and J. Carrera. A mathematical formulation for reactive transport that eliminates mineral concentrations. *Water Resour. Res.*, 34(7):1649–1656, 1998.

- Saaltink, M. W., F. Batlle, C. Ayora, J. Carrera, and S. Olivella. RETRASO, a code for modeling reactive transport in saturated and unsaturated porous media. *Geol. Acta*, 2(3):235–251, 2004.
- Saaltink, M. W., V. Vilarrasa, F. De Gaspari, O. Silva, J. Carrera, and T. S. Rötting. A method for incorporating equilibrium chemical reactions into multiphase flow models for CO₂ storage. *Adv. Water Resour.*, 62:431–441, 2013.
- Saffman, P. G. and G. I. Taylor. The penetration of a fluid into a porous medium or Hele-Shaw cell containing a more viscous liquid. *Proc. R. Soc. Lond. A*, 245:312–329, 1958.
- Saffman, P.G. and Geoffrey Taylor. The penetration of a fluid into a porous medium or Hele-Shaw cell containing a more viscous liquid. *Proc. R. Soc. A*, 245:1242, 1958.
- Saito, K., A. K. Sum, and R. Ohmura. Correlation of hydrate-film growth rate at the guest/liquid-water interface to mass transfer resistance. *Ind. Eng. Chem. Res.*, 49(15):7102–7103, 2010.
- Sanchez-Vila, X., M. Dentz, and L. D. Donado. Transport-controlled reaction rates under local non-equilibrium conditions. *Geophys. Res. Lett.*, 34(10):L10404, 2007.
- Sanford, W. E. and L. F. Konikow. Simulation of calcite dissolution and porosity changes in saltwater mixing zones in coastal aquifers. *Water Resour. Res.*, 25(4):655–667, 1989.
- Sauter, E. J., S. I. Muyakshin, J.-L. Charlou, M. Schlüter, A. Boetius, K. Jerosch, E. Damm, J.-P. Foucher, and M. Klages. Methane discharge from a deep-sea submarine mud volcano into the upper water column by gas hydrate-coated methane bubbles. *Earth Planet. Sci. Lett.*, 243(3-4):354–365, March 2006.
- Shou, Z. and A. Chakrabarti. Ordering of viscous liquid mixtures under a steady shear flow. *Phys. Rev. E*, 61(3):2200–2203, 2000.
- Siggia, E. D. Late stages of spinodal decomposition in binary mixtures. *Phys. Rev. A*, 20:595–605, 1979.
- Skarke, A., C. Ruppel, M. Kodis, D. Brothers, and E. Lobecker. Widespread methane leakage from the sea floor on the northern US Atlantic margin. *Nat. Geosci.*, pages 1–5, 2014.
- Slim, A. Solutal-convection regimes in a two-dimensional porous medium. *J. Fluid Mech.*, 741:461–491, 2014.
- Slim, A., M. M. Bandi, J. C. Miller, and L. Mahadevan. Dissolution-driven convection in a Hele-Shaw cell. *Phys. Fluids*, 25:024101, 2013.
- Sloan, E. D. Fundamental principles and applications of natural gas hydrates. *Nature*, 426(6964):353–63, 2003.

- Sloan, E. D. and C. A. Koh. *Clathrate hydrates of natural gases*. CRC Press, Boca Raton, FL, USA, 3rd edition, 2008.
- Sloan, E. D., C. A. Koh, and A. K. Sum. Gas hydrate stability and sampling: the future as related to the phase diagram. *Energies*, 3(12):1991–2000, 2010.
- Steefel, C. I. and K. T. B. MacQuarrie. Approaches to modeling of reactive transport in porous media. In P. C. Lichtner, C. I. Steefel, and E. H. Oelkers, editors, *Reactive Transport in Porous Media*, volume 34 of *Reviews in Mineralogy*, chapter 2, pages 83–129. Mineralogical Society of America, Washington, DC, 1996.
- Steefel, C. I. and A. C. Lasaga. A coupled model for transport of multiple chemical species and kinetic precipitation/dissolution reactions with application to reactive flow in single phase hydrothermal systems. *Am. J. Sci.*, 294(5):529–592, 1994.
- Suess, E., M. E. Torres, G. Bohrmann, R. W. Collier, J. Greinert, P. Linke, G. Rehder, A. Trehu, K. Wallmann, G. Winckler, and E. Zuleger. Gas hydrate destabilization: enhanced dewatering, benthic material turnover and large methane plumes at the Cascadia convergent margin. *Earth Planet. Sci. Lett.*, 170(1-2):1–15, 1999.
- Sum, A. K., C. A. Koh, and E. D. Sloan. Developing a comprehensive understanding and model of hydrate in multiphase flow: From laboratory measurements to field applications. *Energy Fuels*, 26(7):4046–4052, 2012.
- Sun, C.-Y., G.-J. Chen, C.-F. Ma, Q. Huang, H. Luo, and Q.-P. Li. The growth kinetics of hydrate film on the surface of gas bubble suspended in water or aqueous surfactant solution. *J. Cryst. Growth*, 306(2):491–499, 2007.
- Sun, Y. and C. Beckermann. A two-phase diffuse-interface model for Hele-Shaw flows with large property contrasts. *Physica D*, 237:3089–3098, 2008.
- Sun, Y. and C. Beckermann. Phase-field modeling of bubble growth and flow in a Hele-Shaw cell. *Int. J. Heat Mass Transfer*, 53(15-16):2969–2978, July 2010.
- Suzuki, R., Y. Nagatsu, M. Mishra, and T. Ban. Experimental study on viscous fingering with partial miscible fluids. 69th Annual Meeting of the APS Division of Fluid Dynamics, 2016. URL <http://meetings.aps.org/link/BAPS.2016.DFD.D38.7>.
- Svandal, A., T. Kuznetsova, and B. Kvamme. Thermodynamic properties and phase transitions in the $\text{H}_2\text{O}/\text{CO}_2/\text{CH}_4$ system. *Phys. Chem. Chem. Phys.*, 8(14):1707–13, 2006.
- Swarztrauber, P. N. The methods of cyclic reduction, Fourier analysis, and the FACR algorithm for the discrete solution of Poisson’s equation on a rectangle. *SIAM Review*, 19:490–501, 1977.
- Swernath, S., B. Malengier, and S. Pushpavanam. Effect of Korteweg stress on viscous fingering of solute plugs in a porous medium. *Chem. Eng. Sci.*, 65(7):2284–2291, 2010.

- Szulczewski, M. L. , C. W. MacMinn, H. J. Herzog, and R. Juanes. Lifetime of carbon capture and storage as a climate-change mitigation technology. *Proc. Natl. Acad. Sci. U.S.A.*, 109(14):5185–5189, 2012.
- Szulczewski, M. L. , M. A. Hesse, and R. Juanes. The evolution of miscible gravity currents in horizontal porous layers. *J. Fluid Mech.*, 736:287–315, 2013.
- Szymczak, P. and A. J.C. Ladd. The initial stages of cave formation: Beyond the one-dimensional paradigm. *Earth Planet. Sci. Lett.*, 301(3-4):424–432, 2011a.
- Szymczak, P. and A.J.C. Ladd. The initial stages of cave formation: Beyond the one-dimensional paradigm. *Earth Planet. Sci. Lett.*, 301(3-4):424–432, 2011b.
- Tackley, P. J. Mantle convection and plate tectonics: Toward an integrated physical and chemical theory. *Science*, 288(5473):2002–2007, 2000a.
- Tackley, P. J. Self-consistent generation of tectonic plates in time- dependent, three-dimensional mantle convection simulations, 1. Pseudoplastic yielding. *Geochem., Geophys., Geosyst.*, 01(23), 2000b.
- Tan, C. T. and G. M. Homsy. Simulation of nonlinear viscous fingering in miscible displacement. *Phys. Fluids*, 6:1330–1338, 1988a.
- Tan, C. T. and G. M. Homsy. Simulation of nonlinear viscous fingering in miscible displacement. *Phys. Fluids*, 6:1330–1338, June 1988b.
- Taylor, C. J., K. T. Miller, C. A. Koh, and E. D. Sloan. Macroscopic investigation of hydrate film growth at the hydrocarbon/water interface. *Chem. Eng. Sci.*, 62(23): 6524–6533, December 2007.
- Tegze, G., T. Pusztai, and L. Gránásy. Phase field simulation of liquid phase separation with fluid flow. *Mater. Sci. Eng., A*, 413-414:418–422, 2005.
- Tong, P., W.I. Goldberg, J. Stavans, and A. Onuki. Temporal fluctuation in a turbulently stirred binary liquid mixture. *Phys. Rev. Lett.*, 62(23):2668–2671, 1989.
- Topham, D. R. The formation of gas hydrates on bubbles of hydrocarbon gases rising in seawater. *Chem. Eng. Sci.*, 39(5):821–828, 1984.
- Tréhu, A. M., P. B. Flemings, N. L. Bangs, J. Chevallier, E. Gràcia, J. E. Johnson, C.-S. Liu, X. Liu, M. Riedel, and M. E. Torres. Feeding methane vents and gas hydrate deposits at south hydrate ridge. *Geophys. Res. Lett.*, 31(23), 2004.
- Tréhu, A. M., C. Ruppel, Holland M., G. R. Dickens, M. E. Torres, T.S. Collett, D. Goldberg, M. Riedel, and P. Schultheiss. Gas hydrates in marine sediments: lessons from scientific ocean drilling. *Oceanography*, 19, December 2006.
- Trompert, R. and U. Hansen. Mantle convection simulations with rheologies that generate plate-like behaviour. *Nature*, 395:686–689, 1998.

- Truzzolillo, D., S. Mora, C. Dupas, and L. Cipelletti. Off-equilibrium surface tension in colloidal suspensions. *Phys. Rev. Lett.*, 112(128303), 2013.
- Tryggvason, G. and H. Aref. Numerical experiments on Hele Shaw flow with a sharp interface. *J. Fluid Mech.*, 136:1–30, 1983.
- van der Waals, J. D. *Z. Phys. Chem.*, 13(657), 1894.
- van Heck, H. J. and P. J. Tackley. Planforms of self-consistently generated plates in 3D spherical geometry. *Geophys. Res. Lett.*, 35(19):1–6, 2008.
- Voorhees, P. W. Ostwald ripening of two-phase mixtures. *Annu. Rev. Mater. Res.*, 22:197–215, 1992.
- Wagner, A. J. and J. M. Yeomans. Breakdown of scale-invariance in the coarsening of phase-separating binary fluids. *Phys. Rev. Lett.*, 80:1429–1432, 1998.
- Wagner, C. Theory of the aging of precipitates by dissolution-precipitation (Ostwald ripening). *Z. Electrochem.*, 65:581–591, 1961.
- Walsh, M. R., G. T. Beckham, C. A. Koh, E. D. Sloan, D. T. Wu, and A. K. Sum. Methane hydrate nucleation rates from molecular dynamics simulations : effects of aqueous methane concentration , interfacial curvature , and system Size. *J. Phys. Chem. C*, 115:21241–21248, 2011.
- Wang, B., S. Socolofsky, J. Breier, and J. Seewald. Observations of bubbles in natural seep flares at MC 118 and GC 600 using in situ quantitative imaging. *J. Geophys. Res. Oceans*, 121, 2016.
- Warzinski, R. P., R. Lynn, I. Haljasmaa, I. Leifer, F. Shaffer, B. J. Anderson, and J. S. Levine. Dynamic morphology of gas hydrate on a methane bubble in water: Observations and new insights for hydrate film models. *Geophys. Res. Lett.*, 41, sep 2014.
- Weinstein, A., L. Navarrete, C. Ruppel, T. C. Weber, M. Leonte, M. Y. Kellermann, E. C. Arrington, D. L. Valentine, M. I. Scranton, and J. D. Kessler. Determining the flux of methane into hudson canyon at the edge of methane clathrate hydrate stability. *Geochem., Geophys., Geosyst.*, 17(10), 2016.
- Weir, G. J. , S. P. White, and W. M. Kissling. Reservoir storage and containment of greenhouse gases. *Transp. Porous Media*, 23(1):37–60, 1996.
- Westbrook, G. K., K. E. Thatcher, E. J. Rohling, A. M. Piotrowski, H. Pälike, A. H. Osborne, E. G. Nisbet, T. A. Minshull, M. Lanoisellé, R. H. James, V. Hühnerbach, D. Green, R. E. Fisher, A. J. Crocker, A. Chabert, C. Bolton, A. Beszczynska-Möller, C. Berndt, and A. Aquilina. Escape of methane gas from the seabed along the West Spitsbergen continental margin. *Geophys. Res. Lett.*, 36(15):L15608, August 2009.

- Wheeler, A. A., W. J. Boettinger, and G. B. McFadden. Phase-field model of solute trapping during solidification. *Phys. Rev. E*, 47(3):1893–1909, 1993.
- Wilson, G. A new expression for the excess free energy of mixing. *J. Am. Chem. Soc.*, 86(2):127–130, 1964.
- Witelski, T. P. The structure of internal layers for unstable nonlinear diffusion equations. *Stud. Appl. Math.*, 97(3):277–300, 1996.
- Witherspoon, P. A. and D. N. Saraf. Diffusion of Methane, Ethane, Propane, and n-Butane. *J. Phys. Chem.*, 69(11):3752–3755, 1965.
- Xu, T. F., J. A. Apps, and K. Pruess. Reactive geochemical transport simulation to study mineral trapping for CO₂ disposal in deep arenaceous formations. *J. Geophys. Res.*, 108(B2):2071, 2003.
- Xu, T. F., E. Sonnenthal, N. Spycher, and K. Pruess. TOUGHREACT—A simulation program for non-isothermal multiphase reactive geochemical transport in variably saturated geologic media: Applications to geothermal injectivity and CO₂ geological sequestration. *Comput. & Geosci.*, 32(2):145–165, 2006.
- Xu, T. F., Y. K. Kharaka, C. Doughty, B. M. Freifeld, and T. M. Daley. Reactive transport modeling to study changes in water chemistry induced by CO₂ injection at the Frio-I Brine Pilot. *Chem. Geol.*, 271(3-4):153–164, 2010.
- Xu, W. and C. Ruppel. Predicting the occurrence, distribution, and evolution of methane gas hydrate in porous marine sediments. *J. Geophys. Res.*, 104:5081–5095, 1999.
- Yang, Z. and Y. C. Yortsos. Asymptotic solutions of miscible displacements in geometries of large aspect ratio. *Phys. Fluids*, 9(2):286–298, 1997.
- Yao, J. H., K. R. Elder, H. Guo, and M. Grant. Theory and simulation of Ostwald ripening. *Phys. Rev. B*, 47(21):14110–14125, 1993.
- Yeh, G. T. and V. S. Tripathi. A model for simulating transport of reactive multi-species components: Model development and demonstration. *Water Resour. Res.*, 27(12):3075–3094, 1991.
- Zatsepina, O. Y. and B. A. Buffett. Thermodynamic conditions for the stability of gas hydrate in the seafloor. *J. Geophys. Res.*, 103:2412724139, 1998.
- Zhang, Y. Methane escape from gas hydrate systems in marine environment, and methane-driven oceanic eruptions. *Geophys. Res. Lett.*, 30(7):1–4, 2003.
- Zhao, B., C. W. MacMinn, and R. Juanes. Wettability control on multiphase flow in patterned microfluidics. *Proc. Natl. Acad. Sci. U.S.A.*, 113(37):10251–6, 2016.
- Zhao, H., J. Casademunt, C. Yeung, and J. V. Maher. Perturbing Hele-Shaw flow with a small gap gradient. *Phys. Rev. A*, 45(4):2455–2462, 1992.